DEVICE FOR MEASUREMENT OF OPTICAL PROPERTIES OF TISSUES: 900-1400 nm

DESIGN AND TESTING OF A NONINVASIVE STEADY-STATE DEVICE FOR THE MEASUREMENT OF OPTICAL PROPERTIES OF TISSUES IN THE 900-1400 nm WAVELENGTH REGION

By

JODY T. BRUULSEMA, B.SC.

A Thesis
Submitted to the School of Graduate Studies
in Partial Fulfillment of the Requirements
for the Degree
Master of Science

McMaster University

MASTER OF SCIENCE (1997)
(Physics)

McMaster University
Hamilton, Ontario

TITLE: Design and Testing of a Noninvasive Steady-State Device for the Measurement of Optical Properties of Tissues in the 900-1400 nm Wavelength Region.

AUTHOR: Jody Bruulsema, B.Sc. (University of Waterloo)

SUPERVISOR: Dr. Michael S. Patterson

NUMBER OF PAGES: xi, 127

ABSTRACT

The measurement of the absorption coefficient, μ_a, and the transport scattering coefficient, μ_s', in tissue *in vivo* has applications for blood analyte monitoring, dosimetry for laser therapeutics, and optical imaging techniques. The optical properties of human tissue *in vivo* in the 900-1400 nm wavelength range are currently poorly characterized, even though this may be a useful wavelength range for biomedical optics applications. A system has been developed which is capable of performing steady-state spatially resolved diffuse reflectance measurements in the 900-1400 nm wavelength range, from which optical properties can be estimated. In this technique, light enters the sample in a pencil beam geometry, and reflected light is collected at several distances from the input location. The principal components of the system are a fibre optic probe, a broadband light source, an imaging monochromator, and an InGaAs photodiode array. A Monte Carlo model and a diffusion theory model have been applied to the reflectance data to estimate optical properties. Both nonlinear regression and neural network techniques have been explored to fit the models to the reflectance data. Aqueous suspensions of monodisperse polystyrene spheres of known μ_a and μ_s' were measured to determine the accuracy of the technique in estimating optical properties. The features in the measured spectra compared well with the theoretical spectra for these phantoms, although large discrepancies between predicted and measured optical properties were observed. This disagreement may be a result of not accounting for a small mismatch in refractive index at the phantom-probe boundary, and not accounting for the limited collection angle of the detection fibres in the model. Several measurements were performed on human volunteers to demonstrate the capabilities of the instrument and the advantages of working in the 900-1400 nm wavelength range.

ACKNOWLEDGEMENTS

I would like to thank Dr. Mike Patterson for his patient guidance in this work. I would also like to acknowledge Dr. Joe Hayward and Dr. Robert Weersink for their assistance in the setup and characterization of the equipment. I am indebted to Dr. Tom Farrell for the use of several modeling and analysis programs, and for many helpful conversations regarding theory and data analysis. I wish to thank Ed Hull for the use of his Mie theory programs. I am grateful to Dr. Matthias Essenpreis, Dr. Michael Hein, Dr. Günther Shmelzeisen-Redeker, Dr. Marilyn Gatin, Jörn Becker and other staff in the Diabetes Care, New Technologies department of Boehringer Mannheim GmbH for their useful suggestions and interpretations regarding the *in vivo* studies, their assistance with some of the acquisition and analysis software, and the use of optical standards. I would also like to acknowledge the financial support of Boehringer Mannheim GmbH in this work. I am thankful to Julie Northcott, Ed Castillo, and Lee Chin for their assistance in many elements of this project. I am thankful to the many individuals who volunteered their time for the *in vivo* studies. Lastly, I would like to express my gratitude to my husband, Dave, and my family and friends without whose unfailing encouragement I would not have been able to complete this effort.

TABLE OF CONTENTS

LIST OF TABLES

LIST OF FIGURES

Chapter 1 Introduction

The use of visible and near infrared (NIR) light in therapeutic and diagnostic medicine has recently been receiving increased attention. With the continued development of biomedical optics applications such as photodynamic therapy (PDT), blood oxygenation monitoring, blood constituent monitoring, tissue imaging, optical coherence tomography (OCT) and other surgical procedures involving lasers, there has been considerable interest in the modelling of near infrared (NIR) photon transport in human tissue, and in the optical characterization of these tissues.

At present, however, there are very few published data on the optical properties of *in vivo* human tissue in the 0.9-1.3 μm wavelength range. This is due to several factors: In the past, measurements of optical properties of tissue have focused on the shorter wavelengths within this region for applications including PDT and optical blood oxygenation monitoring. In PDT, light-activated drugs react with oxygen resulting in local cell destruction. Most photosensitizing drugs absorb most strongly at wavelengths below 700 nm, and treatment wavelengths are tuned to maximize this absorption. Blood oxygenation monitoring takes advantage of the fact that oxygenated and reduced haemoglobin absorb light differently in the wavelength region up to about 1.2 μm, but measurements are normally performed in the lower wavelength region where the difference is most pronounced. Another factor which has prevented measurement in the 0.9-1.3 μm wavelength range is that many optical measurement techniques rely on technology such as photomultiplier tubes and silicon detectors, which have drastically reduced sensitivity beyond about 950 nm.

The wavelength range of about 0.6 - 1.3 μm is of interest for therapy and diagnostics using light because of relatively weak light absorption. The longer wavelength region may be preferable for applications such as tissue imaging and OCT, where a lower scattering coefficient permits greater penetration of light [Chan *et al* 1995, Huang *et al* 1991]. NIR optical properties of tissue are also of interest for medical applications employing the Nd:YAG laser operating at a wavelength of 1.064 μm, such as interstitial laser hyperthermia in the treatment of tumours [Panjehpour *et al* 1991]. The limited contribution of haemoglobin to the absorption coefficient of tissue at wavelengths beyond 1.2 μm [Barlow and Polanyi 1962] also suggests that the longer wavelength region could be a better candidate for biological monitoring of tissue constituents such as glucose, since blood oxygenation changes would not contribute to a change in the absorption coefficient.

In order to gain better understanding, control, and predictability in the application of light in the wavelength range of 0.9-1.3 μm in therapeutic and diagnostic medicine, it is necessary to characterize the optical properties of human tissues at these wavelengths. This thesis will describe a system which is capable of obtaining *in vivo* measurements of diffuse reflectance from human skin (or other organs, invasively) in this wavelength region, from which the optical properties of skin can be estimated by applying established models. The models and data reduction methods which have been used to estimate tissue optical properties from diffuse reflectance data will also be discussed. Finally, we will examine the results of several experiments which were performed to establish the accuracy of the method in determining absolute optical properties and to demonstrate the ability of this technique to detect externally induced changes in tissue optical properties *in vivo*.

1.1 Skin Optical Properties in the Near Infrared

Skin is a multi-layered structure comprised of two main layers: epidermis and dermis. The epidermis is the thin outer layer of skin which varies in thickness from 75 to 150 μm over most of the body, and can be as thick as 0.6 mm on the palms and soles of the feet [Odland 1991]. The epidermis contains melanin which contributes to the natural colour of skin. Below the epidermis is the dermis, ranging in thickness from 1 to 4 mm [Odland 1991]. The dermis is composed of fibroelastic connective tissue including collagen and elastin which give the skin its strength and elasticity. The dermis also contains the vasculature which sustains the skin. Human skin is composed of about 65% water [Duck 1990]. Subdermal tissues include fat and muscle.

The fundamental parameters which are used to characterize photon transport in turbid media such as skin are the absorption coefficient, μ_a, the scattering coefficient, μ_s, the scattering phase function, $p(\hat{\Omega},\hat{\Omega}')$, and the index of refraction, n. Light can be absorbed by different chromophores which are present in the skin. Figure 1.1 shows the absorption spectra for the primary chromophores of the skin in the visible and NIR. Absorption is dominated by melanin and oxy/deoxy haemoglobin at the shorter wavelengths, and by water at the longer wavelengths. Much of the scattering of light in skin occurs because of a mismatch between the refractive indices of cellular structures and the intra and extra cellular fluids. In the dermis, scattering of light is mainly due to collagen fibres [Anderson 1993]. Dermal scattering is strongly forward directed, and has been found to depend on wavelength by a power of approximately -3/2 [Anderson 1993]. The refractive index of the skin determines the amount of specular reflection at the surface from either externally or internally incident light. The average refractive index of dermis and epidermis is about 1.4.

1.2 *In vivo* Measurement of Skin Optical Properties in the NIR

It is of particular interest to be able to characterize the optical properties of tissue *in vivo*. A review of measured tissue optical properties was published by Cheong *et al* [1990] which included data at wavelengths at 1.064 μm and below. More recently Chan *et al* [1997] presented optical properties of human skin for wavelengths up to 1.8 μm. Most of these data are based on *in vitro* samples, which may not be representative of live, intact tissue for several reasons: the optical properties may be changed by various steps involved in tissue preparation such as freezing, drying, heating, or soaking in saline, and the perfusion state of tissue is not retained post mortem. Graaff *et al* found that optical properties of dermis *in vivo* were much lower than those obtained from *in vitro* measurements [1993]. Thus, for accurate dosimetry of *in vivo* response during therapeutic procedures, the *in vivo* optical properties are required to accurately predict the fluence

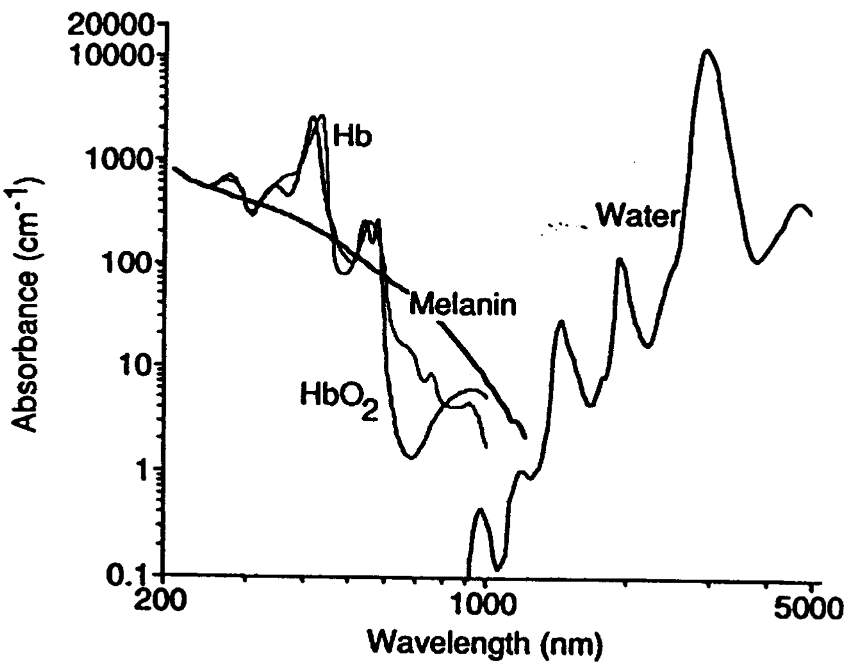

Figure 1.1 Absorption spectra of chromophores in skin in the NIR. Absorption coefficients for pure water, human blood at 11g/100mL Hb concentration and melanin at 15 mg/100mL are shown. Beyond about 900 nm the absorption is dominated by water (from Anderson [1993]).

distribution. In most diagnostic and therapeutic applications it is preferable or necessary to have a non-invasive or minimally invasive technique for measuring the *in vivo* optical properties of a sample of tissue. Monitoring applications are limited to techniques which sample noninvasively. Such a technique must rely on either reflection or transmission of light through a region of tissue. A disadvantage of *in vivo* techniques is that it is difficult to isolate only one type of tissue in a measurement. For example, in measurements of the skin, the layers which comprise the skin and subdermal tissue are all sampled to some extent in either transmission or reflectance measurements.

1.3 Steady-State Spatially Resolved Diffuse Reflectance

There are several techniques which have been used for the measurement of optical properties of tissue *in vivo*. Patterson [1995] and Wilson [1995] have both described the principles of three common techniques: steady-state, frequency domain, and time domain. The method of spatially resolved diffuse reflectance applied in this study falls into the category of steady-state, and is the only method which will be discussed herein.

Steady state spatially resolved diffuse reflectance is a technique which has been successfully used by several researchers for the measurement of optical properties of human tissue in various specific applications. The technique, schematically shown in

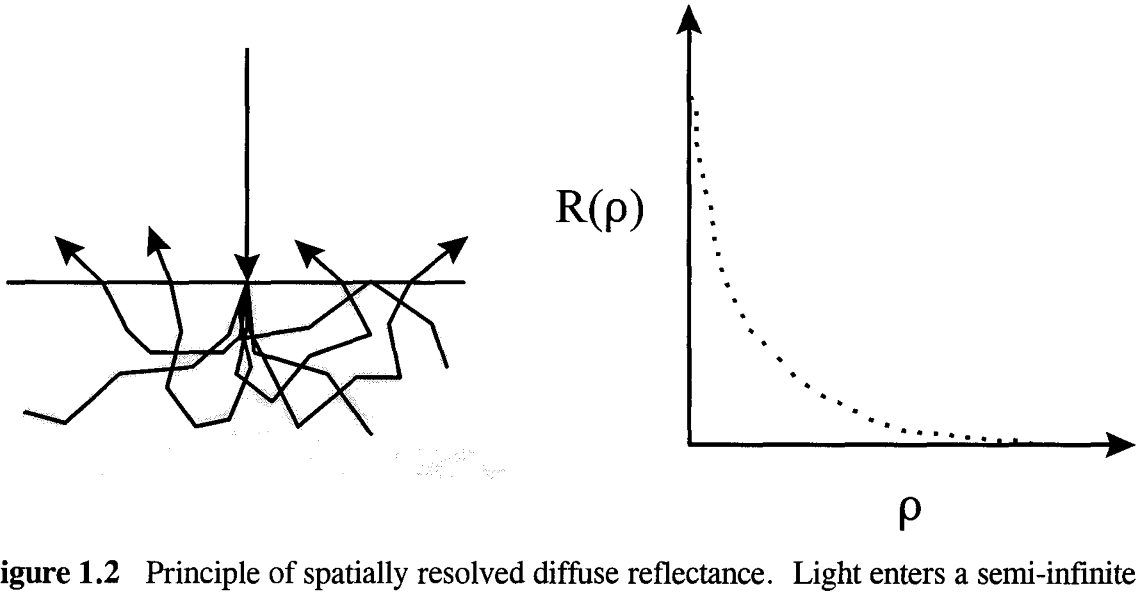

Figure 1.2 Principle of spatially resolved diffuse reflectance. Light enters a semi-infinite medium in a pencil beam geometry. The reflected light is detected on the surface at several radial distances, ρ, from the source. A light propagation model can be applied to the measured R(ρ) to estimate the optical properties.

Figure 1.2, was initially presented by Groenhuis *et al* [1983]. In this method, light is incident upon the surface of the medium under study in a narrow beam geometry. Upon entering the tissue, photons can be either scattered or absorbed, and a small amount of light is diffusely reflected back out of the incident surface as a radially dependent function, R(ρ). Since R(ρ) depends on the optical properties of the medium sampled, it is possible to estimate the optical properties based on a measured R(ρ) distribution using an appropriate model.

Several variations on this basic technique have since been suggested for optical property measurement, as well as other biomedical applications. A common approach is to use fibre optics for delivery and detection of light at discrete distances. In combination with a broadband light source and imaging detector, it is possible to obtain reflectance at several distances and wavelengths simultaneously. Farrell *et al* used this configuration to measure concentrations of exogenous photosensitizers in rat muscle *in vivo* [1994]. Nichols *et al* were able to measure absorption and scattering spectra of various phantoms with an accuracy of about 10% using a similar technique [1997]. Mourant *et al* have also investigated absorption and scattering spectra of tissue-simulating phantoms using this method [1997]. The same approach was used by Bruulsema *et al* to detect blood glucose induced changes in the scattering coefficient of skin in diabetic volunteers [1997]. A related technique known as video reflectometry has been demonstrated by Jacques *et al* [1993] and Kienle *et al* [1996]. In this technique, a narrow beam of light is incident on the surface of the tissue, and a 2-dimensional image of the reflected light is captured using a camera focused on the surface. Other variations of steady-state spatially resolved reflectance measurements include configurations with fewer source-detector distances [Liu *et al* 1995] from which μ_a and μ_s can be estimated with the use of a calibration sample, and oblique incidence reflectometry [Lin *et al* 1997]. The principle can also be applied endoscopically, as has been demonstrated by Bays *et al* [1996].

Chapter 2 Theory

In the study of light propagation in turbid media the wave nature of light is generally ignored and a theory of radiative transport of neutral particles is invoked. The Boltzmann equation of radiative transport for photons travelling through a scattering and absorbing medium with no internal sources is

$$\hat{\Omega}\cdot\nabla_r L(\hat{r},\hat{\Omega}) = -(\mu_a+\mu_s)L(\hat{r},\hat{\Omega}) + \mu_s\int_{4\pi} p(\hat{\Omega},\hat{\Omega}')L(\hat{r},\hat{\Omega}')d\hat{\Omega}' \qquad (1)$$

[Duderstadt and Hamilton 1976] where $L(\hat{r},\hat{\Omega})$ is the radiance (W m^{-2} sr^{-1}) at position r in the direction of unit vector $\hat{\Omega}$. It can be seen that $L(\hat{r},\hat{\Omega})$ is decreased by absorption and scattering losses, and increased by in-scattering from other directions according to the single scattering phase function $p(\hat{\Omega},\hat{\Omega}')$. The scattering phase function is the probability density for scattering from direction $\hat{\Omega}'$ to direction $\hat{\Omega}$, and is generally considered to depend only on the angle between $\hat{\Omega}'$ and $\hat{\Omega}$. While the form of the phase function for tissue is not well known, some models have been used to describe the anisotropic scattering of turbid media such as tissue, including the Henyey-Greenstein phase function [Flock *et al* 1989a]. The phase function is characterized by the average cosine of the scattering angle denoted by g, the anisotropy factor.

The total attenuation coefficient is defined as

$$\mu_t=\mu_a+\mu_s \tag{2}$$

in which each coefficient represents the probability of an interaction per mm path length travelled. The mean free path between events of a certain type is the inverse of the interaction coefficient. The similarity principle can be used to describe photon transport in terms of isotropic scattering using the parameters μ_a and μ_s', where μ_s' is the transport scattering coefficient and is defined as [Wyman *et al* 1989]

$$\mu_s'=\mu_s(1-g) \tag{3}$$

Determination of optical properties of turbid media such as skin amounts to making measurements of transmission and/or reflection of light through a sample, and applying a model of radiative transport to the measured intensities which accounts for the geometry of the sample and measurement. While the Boltzmann equation provides the most accurate representation of the transport process, in practice it is difficult to apply directly to *in vivo* measurements for the extraction of optical properties. Instead, either Monte Carlo simulations of experiments or approximations of radiation transport must be used in the analysis of experimental data.

Photon transport can be modelled using Monte Carlo simulations in which photons are injected into a medium and are followed along their trajectories through the medium [Flock *et al* 1989a, Jacques and Wang 1995]. Scattering and absorption events occur according to input transport properties of μ_s, μ_a and $p(\hat{\Omega},\hat{\Omega}')$. This method is easily tailored to different measurement geometries, but requires a large amount of computing time to achieve acceptable precision. By applying a generalized Monte Carlo simulation it is possible to use conventional fitting techniques to estimate optical properties from experimental data for simple geometries [Kienle and Patterson 1996] .

The most common approach used in the determination of optical properties from experimental data is to approximate photon transport in turbid media as a diffusion process. If isotropic scattering can be assumed by using the transport scattering coefficient, μ_s', and the probability of scatter is much greater than the probability of absorption ($\mu_s' >> \mu_a$) then the diffusion approximation to the Boltzmann equation can be used. Both Monte Carlo and diffusion theory techniques have been applied in the method of spatially resolved diffuse reflectance measurements for the determination of optical properties in this study, and are described in the following sections.

2.1 Monte Carlo Modelling

Monte Carlo techniques are useful when accurate, practical analytical models are difficult to derive. These methods have been applied to steady-state spatially resolved diffuse reflectance experiments for comparison with models [Flock *et al* 1989a] and with experimental data [Flock *et al* 1989b]. Typically, the source is modelled as an infinitely narrow 'pencil' beam of light incident normally on the surface of a semi-infinite medium.

The optical properties μ_s, μ_a, n_{rel} and g are used to determine the paths of photons through the medium. A random number generator is used to sample discrete events from the probability distributions that describe them. Anisotropic scattering can be modelled by the Henyey-Greenstein phase function which is determined only by g as [Henyey and Greenstein 1941]

$$p(\hat{\Omega},\hat{\Omega}')=\frac{1}{4\pi}\frac{1-g^2}{(1+g^2-2g\hat{\Omega}\cdot\hat{\Omega}')} \quad \textbf{(4)}$$

While it is possible to record all information about the trajectory of photons in the medium, it is of most interest to score the photons where they leave the medium for direct comparison with diffuse reflectance experiments. The surface of the medium is divided into annular bins of discrete width, and the number of photons exiting through each annulus, normalized by the annular area, is a measure of the diffuse reflectance. In order to obtain an acceptable signal to noise ratio in these Monte Carlo simulations it is necessary to trace the histories of millions of photons, which can be computationally expensive. Each simulation provides reflectance information for only one set of optical properties, and direct application of this Monte Carlo technique is not practical for solving inversely for the optical properties of a medium based on experimentally measured spatially resolved diffuse reflectance.

A modified approach to the Monte Carlo technique was described by Kienle and Patterson [1996] in which optical properties of turbid media could be determined from a single Monte Carlo simulation if the relative refractive index, n_{rel}, and anisotropy parameter, g, are both known. If only the reduced scattering coefficient, μ_s', is required, g need only be known approximately. Photon absorption obeys Beer's law whereby the probability of absorption depends on the path length travelled and the absorption coefficient. If the mean free path between scatter events and the total number of scatter events are known, then the probability of absorption at some exit distance ρ on the surface can be determined for any absorption coefficient. Also, the scattering events can also be scaled because different scatter coefficients change only the mean free path (mfp) between scatter events (1 mfp = $1/\mu_s$). Kienle and Patterson applied this 'Mono Monte Carlo' technique to model time-resolved reflectance from a point, impulse source incident on a semi-infinite medium. However, it is directly applicable to the problem of steady-state spatially resolved diffuse reflectance measurements.

The physics of the simulation is the same, but in contrast to the traditional technique in which μ_s, μ_a, n_{rel} and g are defined at the outset, in the 'Mono Monte Carlo' technique only n_{rel} and g are fixed, and the scoring is done somewhat differently. The exit surface is divided into annular bins of discrete width and distance from the input source, where the dimensions are in units of mean free paths rather than physical distance. The exiting photons are then scored according to the mean free path

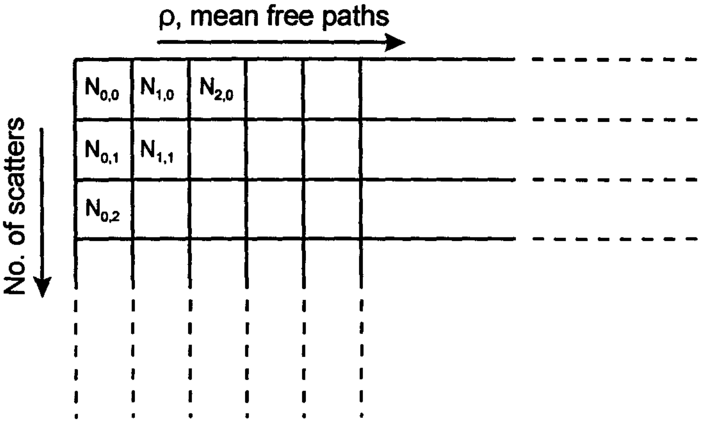

Figure 2.1 Scoring grid design for 'Mono Monte Carlo' simulation.

bin in which they exit, as well as the number of scatter events experienced in their trajectory. This scoring grid is pictured in Figure 2.1. It is still necessary to simulate millions of photons to obtain acceptable statistics in scored quantities. However, one simulation contains information from which reflectance can be extracted for any combination of μ_s and μ_a. This provides a sort of look-up table with which the transport model can be fit to experimental data by adjustment of μ_s and μ_a, as long as n_{rel} and g match the experiment accurately.

A scaling procedure is used to produce reflectance at any distance for a desired μ_s and μ_a. The following steps are followed in the reflectance extraction:

1. Convert distance to number of mean free paths: $\rho_{mfp}=\rho(\mu_a+\mu_s)=\rho\mu_t$
2. Calculate reflectance for integer mfp columns (see Figure 2.1)to the left and right of ρ_{mfp}(photons are scored for only integer mfp).
3. The scatter bins in the left and right mfp columns are scaled using the ratio of the scattering coefficient to the total attenuation coefficient:

$$R(\rho_{left,i}) = N_{left,i}\left(\frac{\mu_s}{\mu_t}\right)^i \tag{5}$$

   where i is the number of scatters. The ratio, $\frac{\mu_s}{\mu_t}$, is called the albedo. Multiplying by this factor for each scatter event removes the fraction of photons lost through absorption.

4. The total reflectance for the left and right mfp is the sum over all scatter bins:

$$R_{left} = \sum_{i=0}^{max.\ scatters} R_{left,i} \tag{6}$$

5. Interpolate between $R(\rho_{left})$ and $R(\rho_{right})$ to find $R(\rho_{mfp})$. Divide by the annular area of the mfp bin, and normalize to the total number of photons simulated.

2.2 Diffusion Theory Model

Diffusion theory can be used as a model for light propagation provided that scattering dominates absorption. The diffusion equation has been derived from the Boltzmann equation [Keijzer *et al* 1988] and can be tailored to describe a particular type of experiment by correctly modelling the source term and applying the appropriate boundary conditions. In these spatially resolved diffuse reflectance measurements, a narrow collimated beam of light impinges normally onto the surface of a semi-infinite medium. It is convenient to model this source as an isotropic point source located in the medium at a depth z_o equal to one transport mean free path. The method of images has been used to satisfy the boundary conditions at the surface of the semi-infinite medium. For a mismatched boundary, such as an air-tissue interface, the photon current into the medium at the surface ($z = 0$) is due only to the internally reflected component. Otherwise, as in a matched boundary in which the surface is bounded by a non-scattering medium with $n = n_{medium}$, the photon current into the medium at the surface must be 0. Either boundary condition can be satisfied by setting the fluence equal to 0 at an extrapolated boundary at a distance z_b = 2AD above the surface [Farrell *et al* 1992b], where D is the diffusion coefficient given by

$$D=\frac{1}{3(\mu_a+\mu_s')} \tag{7}$$

and A is a term to account for refractive index mismatch at the boundary. The zero fluence plane is achieved by placing a negative image source in the plane at a distance z_o+z_b above the extrapolated boundary, which corresponds to a distance $z=z_o+2z_b$ above the surface of the semi-infinite medium. A diagram of the boundary condition treatment is given in Figure 2.2. The fluence rate at some location within the medium is taken as the Green's function for the fluence from both the real source and the image source which yields

$$\Phi(\rho,z)=\frac{1}{4\pi D}\left(\frac{e^{-\mu_{eff}r_1}}{r_1}-\frac{e^{-\mu_{eff}r_2}}{r_2}\right) \tag{8}$$

The parameter A is related to the diffuse internal reflectance and is given by

$$A=\frac{2/(1-R_o)-1+|\cos\theta_c|^3}{1-|\cos\theta_c|^2} \tag{9}$$

where θ_c is the critical angle and R_o is related to the relative refractive index, n_{rel}, according to [Keijzer *et al* 1988]

$$R_o = \frac{(n_{rel}-1)^2}{(n_{rel}+1)^2} \tag{10}$$

An empirical estimation of the parameter A was given by Groenhuis *et al* [1983] where

$$A = \frac{1+r_d}{1-r_d} \tag{11}$$

where

$$r_d = -1.440 n_{rel}^{-2} + 0.710 n_{rel}^{1} + 0.668 + 0.0636 n_{rel} \tag{12}$$

In the case of a matched boundary, either calculation returns a value of 1 for A.

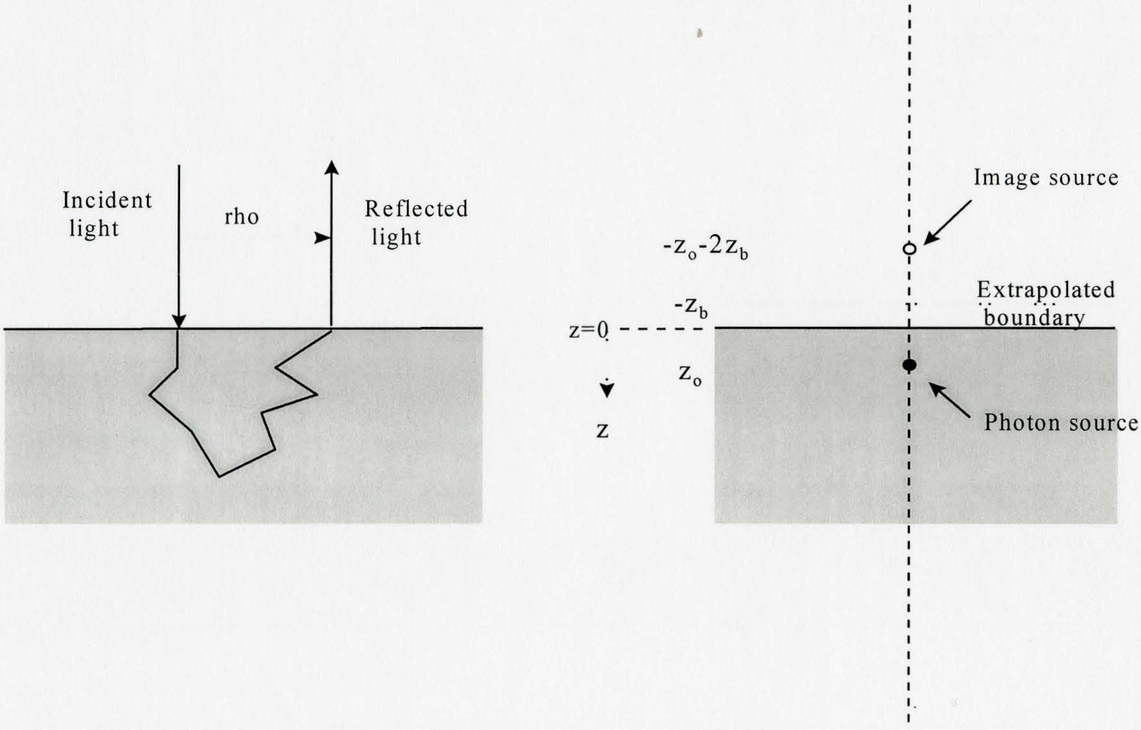

Figure 2.2 Treatment of boundary conditions in the diffusion model for a semi-infinite medium.

The quantity measured in an experiment is proportional to the diffuse reflectance -- the photon flux per unit area exiting the surface of the medium at a distance ρ from the source. The reflectance can be expressed as the current across the boundary as

$$R(\rho) = -D\nabla\Phi(r)\big|_{z=0} \tag{13}$$

A solution for the steady-state diffuse reflectance was derived by Farrell *et al* [1992b] and is given by

$$R(\rho) = \frac{1}{4\pi}\left\{ z_o\left(\mu_{eff} + \frac{1}{r_1}\right)\frac{\exp^{-\mu_{eff} r_1}}{r_1^2} + \left(z_o + 2z_b\right)\left(\mu_{eff} + \frac{1}{r_2}\right)\frac{\exp^{-\mu_{eff} r_2}}{r_2^2} \right\} \tag{14}$$

where r_1 and r_2 are the respective distances to the real and image sources at some radial distance ρ along the surface, such that

$$r_1 = \sqrt{\left(\frac{1}{\mu_t^{\prime}}\right)^2 + \rho^2} \qquad r_2 = \sqrt{\left(\frac{\frac{4}{3}A + 1}{\mu_t^{\prime}}\right)^2 + \rho^2} \tag{15}$$

and $\mu_{eff} = \sqrt{3\mu_a(\mu_a + \mu_s^{\prime})}$ is the effective attenuation coefficient in the diffusion approximation.

The diffusion model breaks down at distances close to the source where photons have not experienced a sufficient number of scatter events to be considered diffuse. Comparison studies with Monte Carlo simulations indicate that the diffusion approximation should only be applied at radial distances greater than one transport mean free path ($1/\mu_s'$) [Nichols *et al* 1997].

This solution was found to be inadequate for the description of diffuse reflectance from a semi-infinite medium with a mismatched boundary [Kienle *et al* 1996]. In a comparison of different treatments of boundary conditions in the diffusion approximation to the transport equation for frequency domain techniques, Haskell *et al* [1994] suggested a more correct expression for the diffuse reflectance as the integral of the radiance over the backward hemisphere. Kienle and Patterson [1997] applied this analysis to obtain modified solutions for steady state diffuse reflectance which are more accurate for mismatched boundary conditions. The modified solution is

$$R(\rho)=\int_{2\pi} d\Omega[1-R_{fres}(\theta)]\frac{1}{4\pi}[\Phi(\rho)+3D\frac{\partial\Phi(\rho)}{\partial z}\cos\theta]\cos\theta \qquad \textbf{(16)}$$

For a matched boundary, the two expressions yield very similar results. However, for a mismatched boundary the diffuse reflectance differs significantly. Figure 2.3 shows the theoretical diffuse reflectance as a function of distance for the two solutions given in Equations 14 and 16 for two different sets of optical properties. Figure 2.3(a) compares the two solutions for a matched boundary situation, while Figure 2.3(b) compares them for a boundary mismatch of 1.4, similar to what might be found at the surface of skin. The reflectance in each set has been normalized to the reflectance at a distance of 1 mm.

In published descriptions of spatially resolved diffuse reflectance measurements an absorbing surface probe is often used so that a matched boundary is assumed. However, this assumption may not always be accurate, and it may be necessary to assume a slight effective mismatch, for which Equation 16 must be used.

2.3 Comparison of Monte Carlo and Diffusion Models

A comparison of the diffuse reflectance generated from the Monte Carlo simulation and diffusion theory is presented in Figure 2.4 for the case of matched and mismatched boundaries. The Monte Carlo data were obtained using the 'Mono Monte Carlo' method with $g=0.9$, and diffusion theory data were generated using Equation 16. The reflectance has been normalized to the reflectance at 1 mm. Results for two different sets of optical properties are shown. From these graphs there appears to be fairly good agreement between the Monte Carlo and diffusion theory reflectance beyond a distance of about 1 mm. As discussed in 2.3, diffusion theory is not expected to perform very well at close distances.

Inspection of Equation 14 shows that for large ρ, a plot of $\ln(\rho^2 R(\rho))$ versus ρ yields a line with slope of μ_{eff}. Farrell *et al* [1992a] also demonstrated that such a plot contains a peak near the origin which has a shape and position which is related to μ_t'. For this reason, it is revealing to display reflectance data in the form of $\ln(\rho^2 R(\rho))$ versus ρ. The same data displayed in Figure 2.4 are shown in Figure 2.5 in this modified format, with the reflectance normalized to the reflectance at 1 mm. Results for an additional set

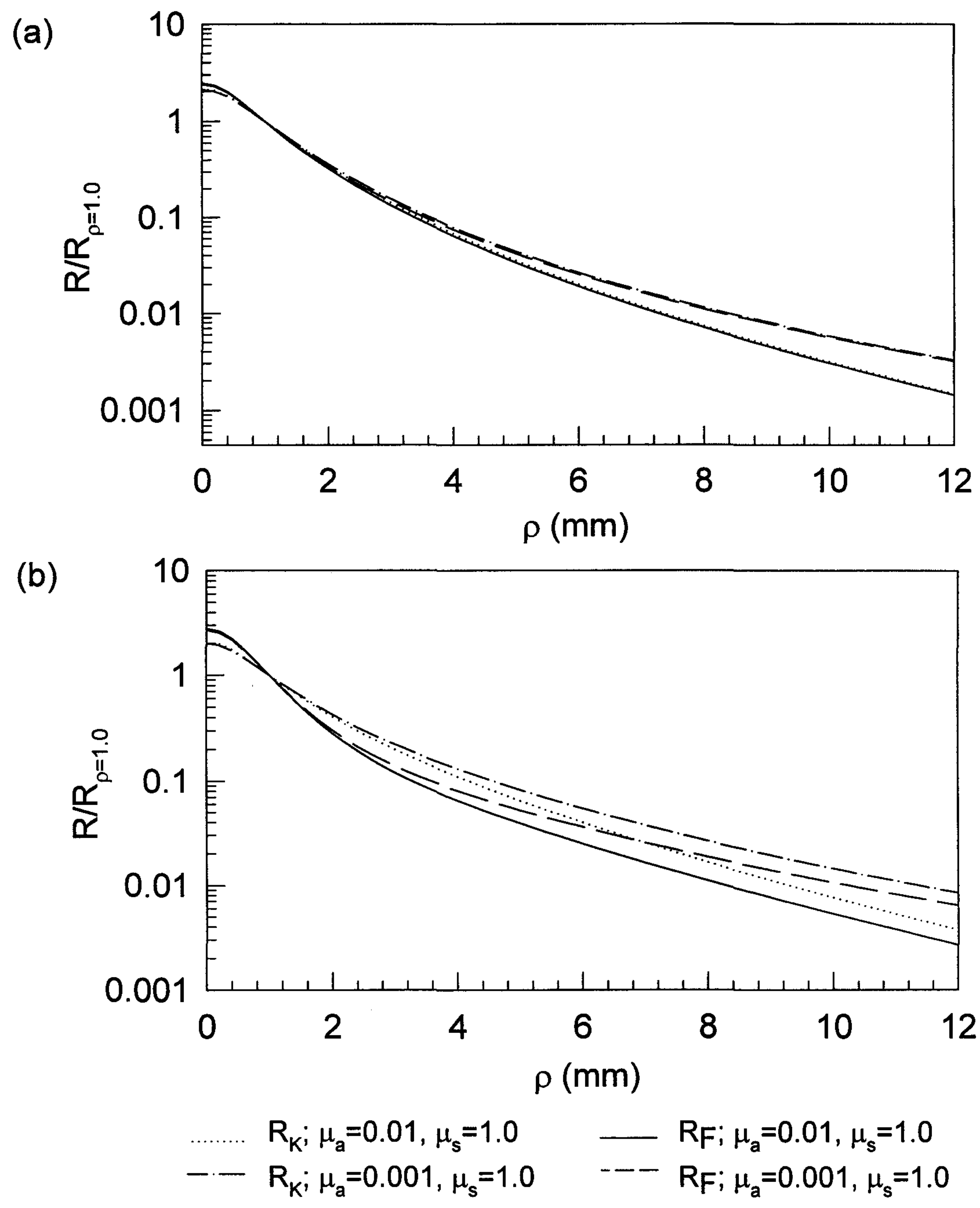

Figure 2.3 Comparison of two diffusion theory solutions for diffuse reflectance from a semi-infinite medium. (a) n_{rel} = 1.0 (matched boundary). (b) n_{rel} = 1.4 (mismatched boundary). R_K: Solution from Kienle and Patterson (Equation 16). R_F: Solution from Farrell *et al* (Equation 14). Theoretical reflectance is shown for μ_s' = 1.0 mm^{-1} and μ_a = 0.001 and 0.01 mm^{-1}. Reflectance has been normalized to ρ = 1.0 mm

of optical properties are included in these graphs so that the effect of changing both μ_s' and μ_a on the shape of the curve can be seen. This method of presentation highlights differences in the reflectance models which are not clearly seen by simply looking at the log of the reflectance.

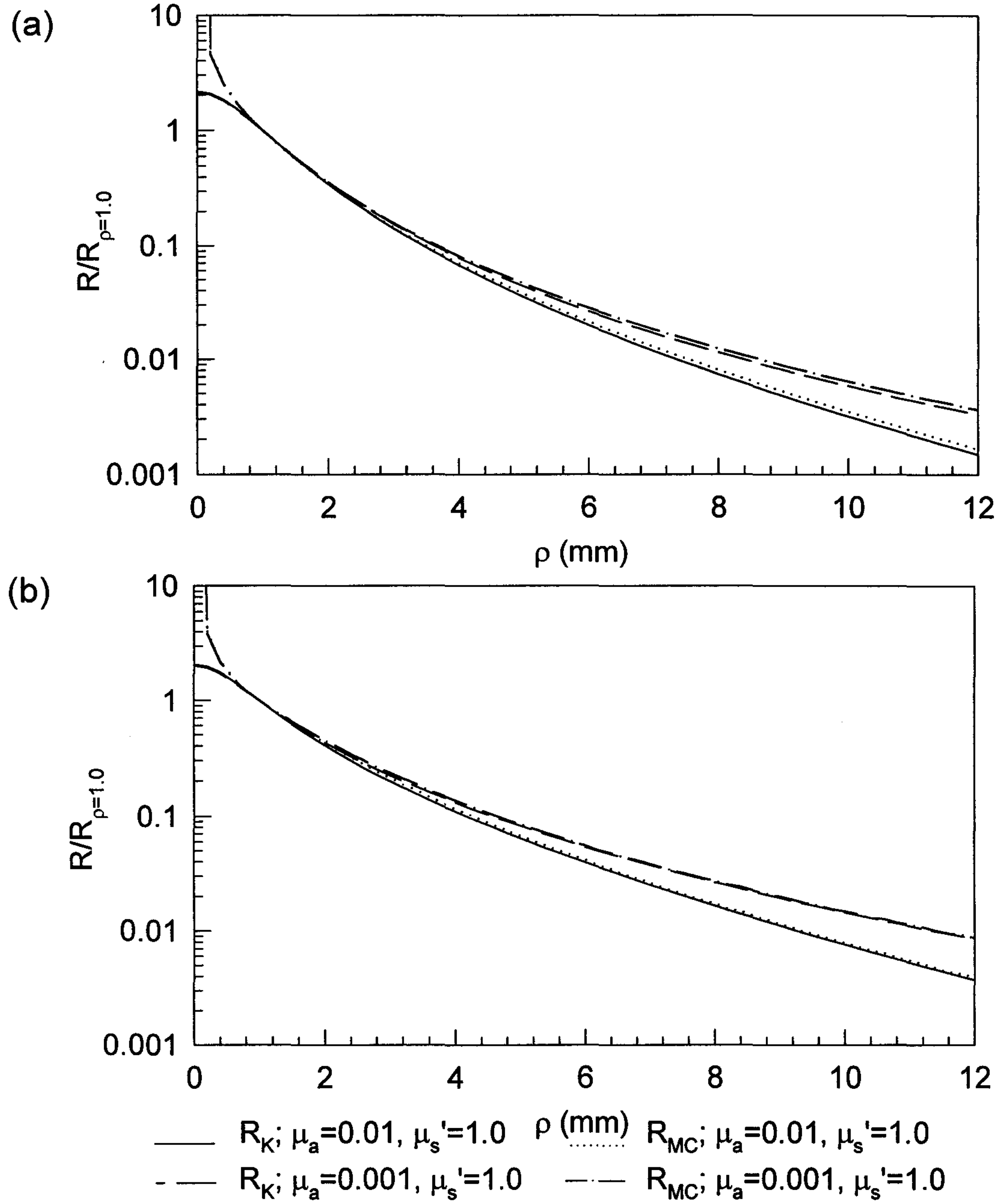

Figure 2.4 Comparison of Monte Carlo and diffusion theory diffuse reflectance. (a) n_{rel} = 1.0 (matched boundary). (b) n_{rel} = 1.4 (mismatched boundary). R_{MC}: Monte Carlo reflectance, g=0.9. R_K: Diffusion model diffuse reflectance from Kienle and Patterson (Equation 16). Theoretical reflectance is shown for $\mu_s' = 1.0$ mm^{-1} and $\mu_a = 0.001$ and 0.01 mm^{-1}. Reflectance has been normalized to $\rho = 1.0$ mm.

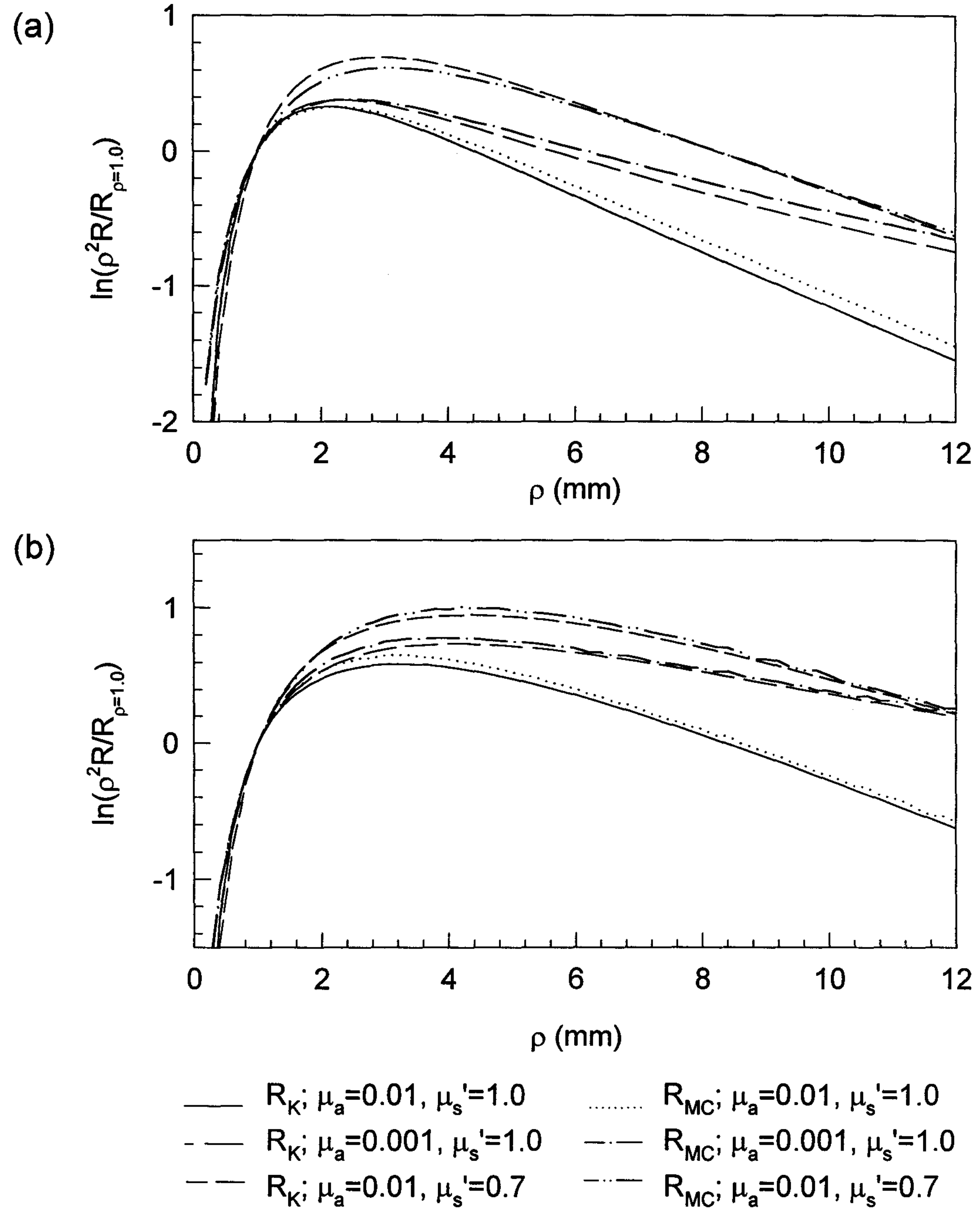

Figure 2.5 Monte Carlo and diffusion model diffuse reflectance plotted as $\ln(\rho^2R(\rho))$, normalized to 1 mm. (a) n_{rel} = 1.0 (matched boundary). (b) n_{rel} = 1.4 (mismatched boundary). R_{MC}: Monte Carlo reflectance, g=0.9. R_K: Diffusion model diffuse reflectance from Kienle and Patterson (Equation 16). Theoretical reflectance is shown for μ_s' = 1.0 mm^{-1} and μ_a = 0.001 and 0.01 mm^{-1}. Reflectance has been normalized to ρ = 1.0 mm.

Chapter 3 Estimation of Optical Properties

The models described in Chapter 2 can be used to estimate the optical properties of a sample from the measured diffuse reflectance. Optical properties in the model are adjusted to obtain the best match between theoretical intensities and the measured intensities. The simplest approach is to apply a nonlinear least squares fit to an analytical model for reflectance based on the diffusion approximation. In some situations this method may not be suitable due to model constraints or speed of evaluation. Two types of fitting algorithms have been applied to both the Monte Carlo modelling and the diffusion theory analytical model. The first fitting algorithm is a nonlinear least squares fit, and the second is a neural network. These methods are described in the following sections with their specific applications to the models.

3.1 Nonlinear Least Squares Fitting

The nonlinear least squares fitting algorithm used is a conventional Levenberg-Marquardt technique [Bevington 1969]. This method is straightforward when applied to the analytical diffusion solutions for the radial reflectance, $R(\rho)$, as given by Equations 14 or 16. The fitting can be performed using either the natural log of the reflectance, or $\ln(\rho^2R(\rho))$. The measurements provide only relative diffuse reflectance, so it is necessary to either fit a normalization constant in addition to μ_a and μ_s', or to fit normalized data. A QBASIC program created by Tom Farrell (Hamilton Regional Cancer Centre) was used to perform the fits. The fitting function used in the program was the diffuse reflectance given by Equation 14, assuming a matched boundary. When a matched boundary is assumed, Equations 14 and 16 are equivalent. For this reason, the simpler expression (Equation 14) was used for the analysis.

As a measure of the performance of the diffusion model and fitting algorithm, several sets of reflectance data were generated from the 'Mono Monte Carlo' simulation for a range of combinations of μ_a and μ_s'. 1% noise randomly sampled from a normal distribution [Abramowitz and Stegun 1972] was added to the reflectance data to simulate typical experimental noise. The nonlinear least-squares fitting program was then used to estimate the optical properties. The estimated optical properties were compared to the input properties to characterize the performance. The results of this comparison are shown in Figure 3.1. Limit lines corresponding to 20% error in estimated μ_a (Figure 3.1a) and 10% in estimated μ_s' (Figure 3.1b) are shown on either side of the line of identity for reference. For most μ_s' greater than 0.5 mm^{-1}, this method obtains μ_s' to within 10% of the input value, and most μ_a to within 20%. μ_s' is systematically underestimated for μ_s' greater than 0.5 mm^{-1}, and overestimated for μ_s' less than 0.5 mm^{-1}, with some gross errors occurring. Some large errors in the estimated μ_a occurred for larger values of the input $\mu_{a,}$ corresponding to reflectance sets with μ_s' less than 0.5 mm^{-1}.

The nonlinear least-squares fitting technique can also be applied to the 'Mono Monte Carlo' method described in Chapter 2. However, rather than fitting to an analytical model, the model reflectance is obtained by scaling the Monte Carlo grid for different combinations of μ_a and μ_s'as described in Chapter 2. Because there is noise in both the Monte Carlo reflectance and the measured reflectance, the χ^2 surface is more likely to contain local minima which can prevent the fit from converging to the correct solution. For this reason, it is sometimes necessary to try multiple starting points in order to improve the likelihood of convergence. This method is also slower due to the increased number of calculations involved in scaling the Monte Carlo grid. Fitting to Monte Carlo data can be particularly useful when estimating optical properties of materials for which diffusion theory no longer applies, such as those with low μ_s' or high μ_a . A Pascal computer program was written to perform these fits.

The performance of the fitting algorithm was evaluated using a method similar to the diffusion theory nonlinear least-squares fit. Again, 1% noise randomly sampled from a normal distribution was added to Monte Carlo data covering a range of combinations of μ_a and μ_s' [Abramowitz and Stegun 1972]. Although the Monte Carlo is implicitly noisy, this additional noise ensured that the fits could not converge to discrete points in the Monte Carlo grid which would yield a χ^2 of 0 (This could occur since the reflectance data was generated from the same Monte Carlo grid as was used in the fitting). Furthermore, it allows for a more direct comparison to the performance of the nonlinear least-squares fit to the analytical model. These data were fit with the Monte Carlo nonlinear least-squares fitting program, after which the input and output optical properties were compared. The input versus output optical properties are given in Figure 3.2 . This comparison was

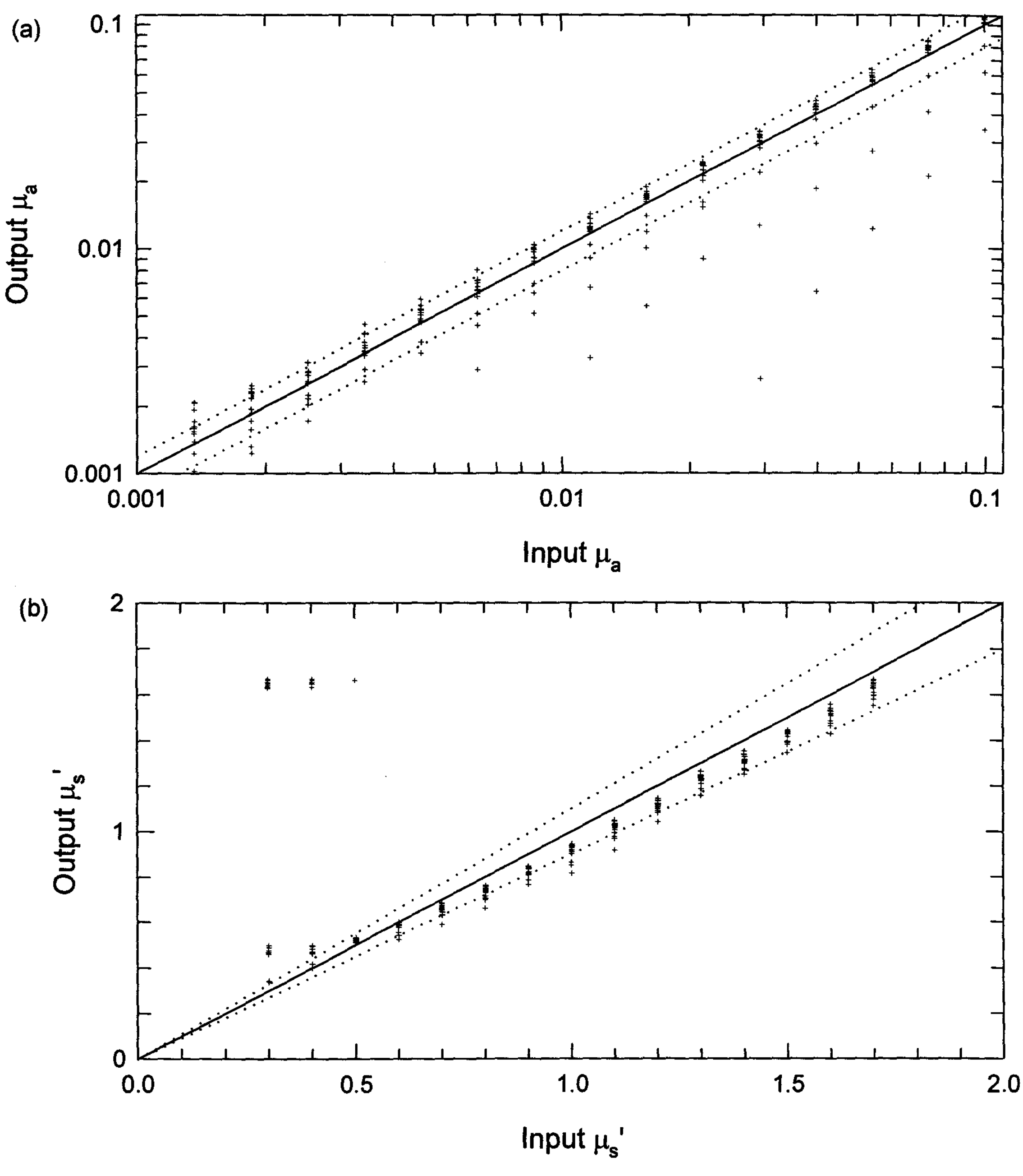

Figure 3.1 Comparison of input versus output optical properties using the nonlinear least-squares fit of diffusion theory (Equation 14) to data generated from a Mono Monte Carlo simulation with g=0.9, n_{rel} = 1.0. 1% random Gaussian noise was added to the reflectance prior to fitting. (a) μ_a. (b) μ_s'. Dotted lines demark relative errors of 10% and 20% for μ_s' and μ_a respectively.

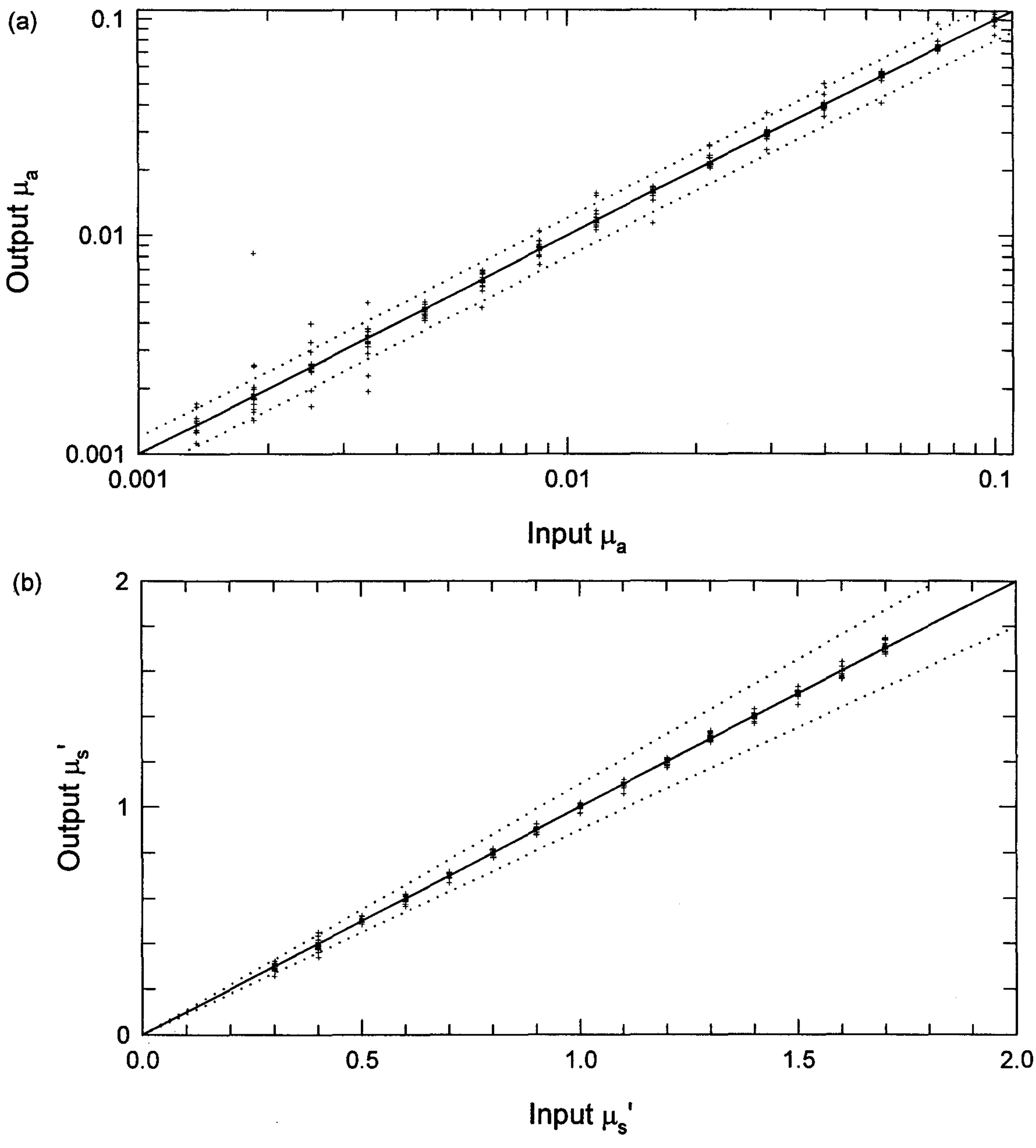

Figure 3.2 Comparison of input versus output optical properties using a nonlinear least-squares fit using a 'Mono Monte Carlo' simulation with $g=0.9$, $n_{rel} = 1.0$. 1% random Gaussian noise was added to the reflectance data prior to fitting. (a) μ_a. (b) μ_s'. Dotted lines demark relative errors of 10% and 20% for μ_s' and μ_a respectively.

performed for the case of a matched boundary only. Limit lines corresponding to 20% error in estimated μ_a (Figure 3.2a) and 10% in estimated μ_s' (Figure 3.2b) are shown on either side of the line of identity for reference. The Monte Carlo fitting results did not suffer from the same systematic discrepancies of the diffusion model fits. μ_s' was estimated to well within 10% of the input value except for some low μ_s'. μ_a was almost always estimated to within 20% of the input value.

3.2 Neural Network Fitting

An alternative data reduction technique was suggested by Farrell *et al* [1992a] which takes advantage of the characteristic shape of diffuse reflectance curves when plotted in the form of $\ln(\rho^2 R(\rho))$ versus ρ. As discussed in Section 2.3, the slope of this curve at large ρ reduces to μ_{eff}, while the shape and position of the peak depend on μ_t'. Hence it may be possible to deduce the optical properties of a sample based on simply the shape of the curve. Neural networks have been used as mathematical tools capable of performing tasks such as pattern recognition. The general neural network technique applied in this study involves training a neural network using a large number of sets of theoretical reflectance data for different combinations of optical properties selected from a relevant range. Experimentally obtained reflectance can then be fed through the trained network in order to obtain an estimate of the optical properties. Neural networks can be trained with theoretical data based on either Monte Carlo simulations or diffusion theory approximations.

A neural network was created using a method described by Farrell *et al* [1992a]. Theoretical reflectance data were generated for 15 source-detector distances ranging from 1 to 10 mm spaced according to the physical probe distances described in Chapter 4. The data obtained from diffusion theory for a matched boundary (Equation 14), were converted to $\ln(\rho^2 R(\rho))$, and then normalized to the first distance. Noise characteristic of experimental data was also added to the reflectance values. 200 such sets of 15 points were generated by randomly selecting combinations of μ_a and μ_s' respectively from the ranges 0.001-0.1 mm^{-1} and 0.3-2.5 mm^{-1}. The neural network consisted of 15 input nodes for the 15 input $\ln(\rho^2 R(\rho))$ points, 32 hidden layer nodes, and 2 output layer nodes for μ_{eff} and μ_t'. The neural network was trained using a QBASIC program created by Tom Farrell (Hamilton Regional Cancer Centre) which applies the generalized delta rule described elsewhere [Rumelhart and McClellend 1986]. Training amounts to adjusting hidden layer node weights until the matrix acting upon all input sets provides the smallest error between the output layer and the optical properties corresponding to the input layer. The training takes several hours on a 90 MHz Pentium computer.

The performance of the neural network can be evaluated by its ability to estimate optical properties from another set of theoretical data for randomly selected combinations of μ_a and μ_s', different from the data used to train the network, but generated using the same theoretical model. The output optical properties can be compared to the input properties as a measure of performance. Figure 3.3 shows the input versus output optical properties for the neural network used. These plots clearly delineate those regions in which performance is best, and those in which performance is somewhat poor. As indicated by the lines of 10% error, the output μ_s' is found to within 10% of the input for the entire range. The ability of the network to determine μ_a is considerably poorer, particularly for μ_a less than 0.001 mm^{-1}. Such low values for absorption are unlikely in water-rich materials in the NIR.

Performance was also assessed by applying the neural network to reflectance data generated from a Monte Carlo simulation, using the same method as for the nonlinear least-squares fitting technique. Since Monte Carlo data more closely represent data which would be obtained experimentally, this analysis provides a measure of the accuracy of the neural network. The estimated optical properties were then compared to the input properties as a measure of performance. The results of this comparison are shown in Figure 3.4. Limit lines corresponding to 20% error in estimated μ_a (Figure 3.4a) and 10% in estimated μ_s' (Figure 3.4b) are shown on either side of the line of identity for reference. The neural network performance is systematically similar to the nonlinear least-squares fitting method which applied the same model (Figure 3.1), although the errors are somewhat greater.

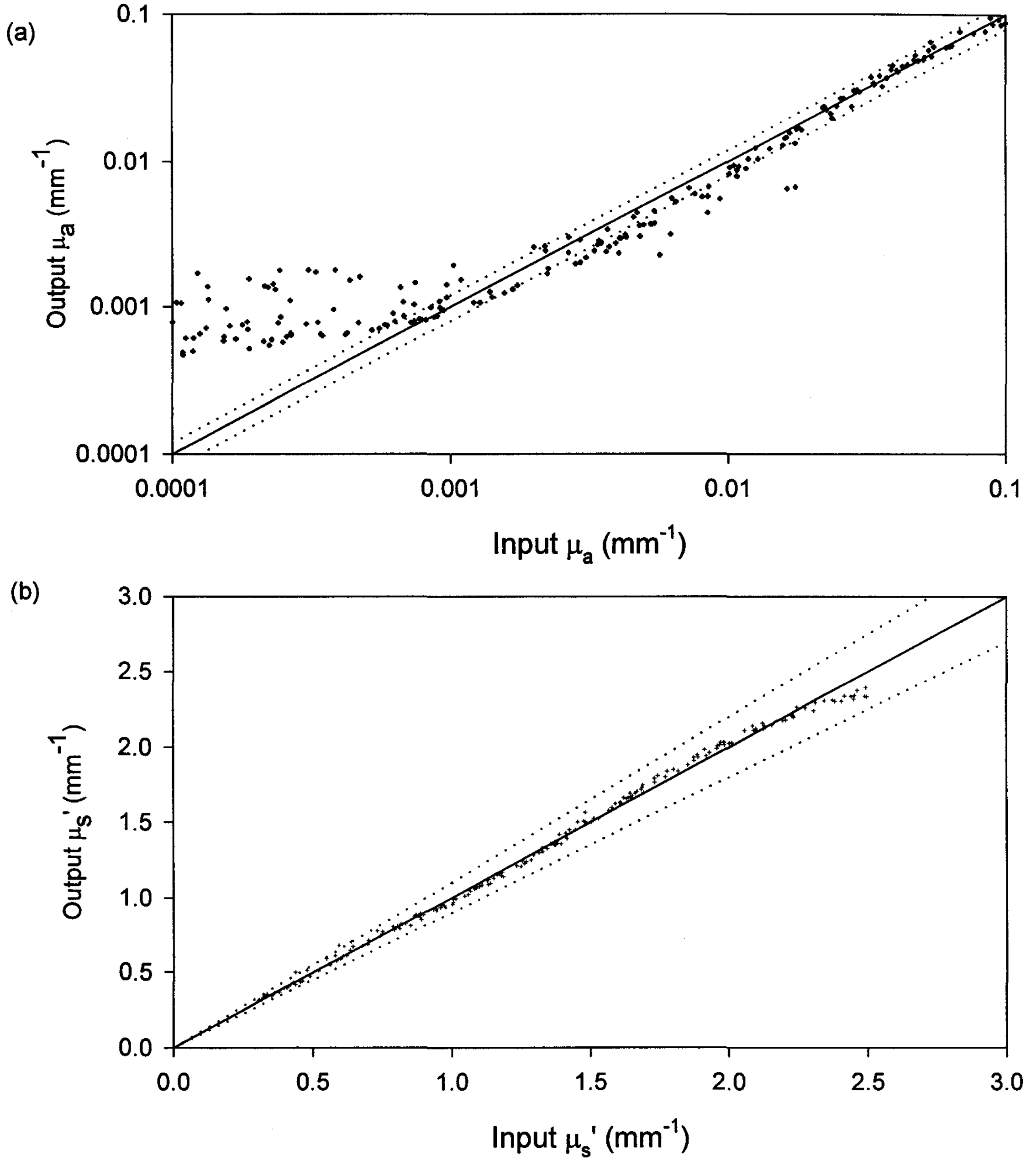

Figure 3.3 Comparison of input versus output optical properties using a neural network trained with reflectance generated from diffusion theory (Equation 14), where input reflectance was also obtained from diffusion theory. This demonstrates the performance of the neural network itself. (a) μ_a. (b) μ_s'. Dotted lines demark relative errors of 10% and 20% for μ_s' and μ_a respectively.

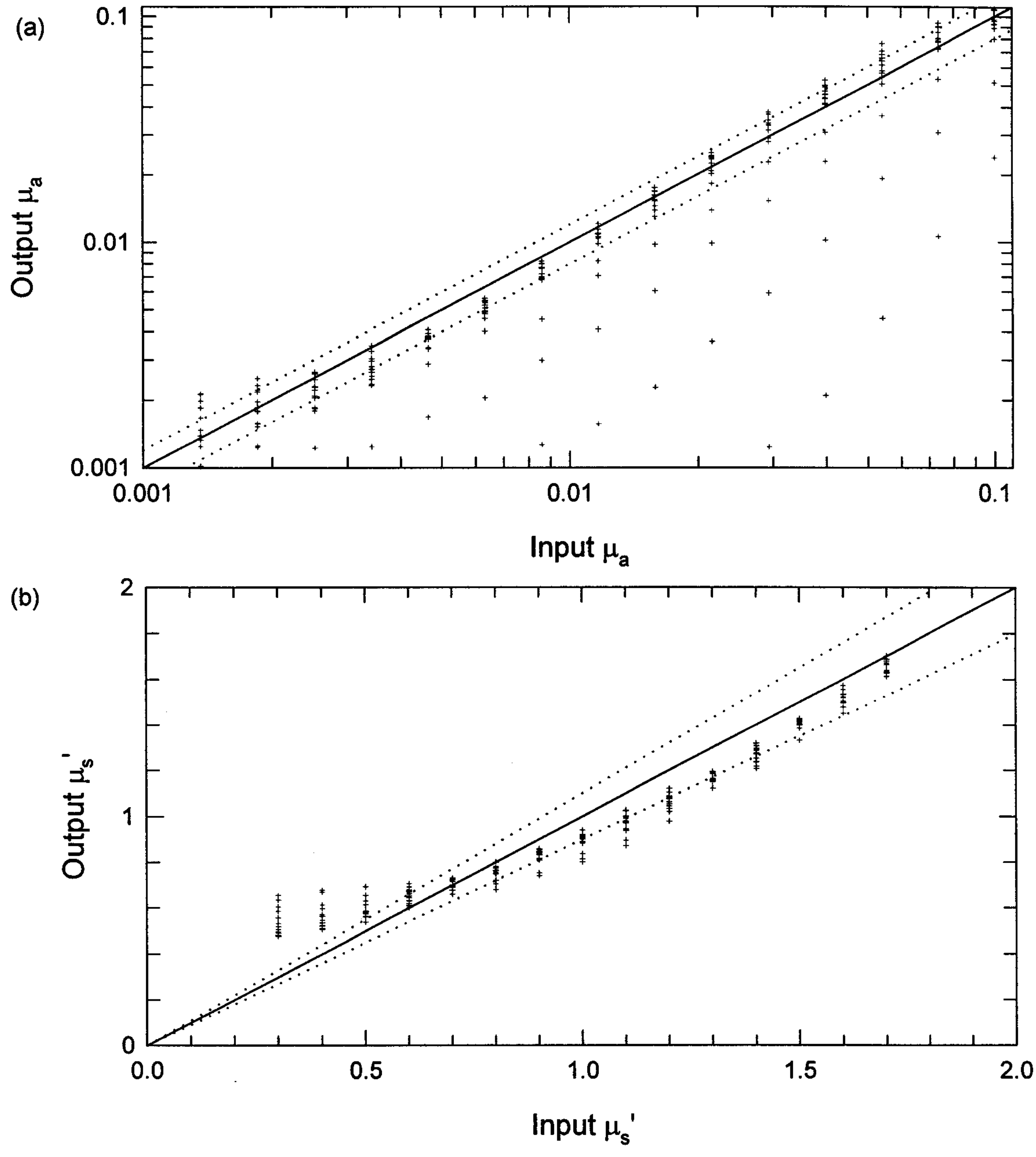

Figure 3.4 Comparison of input versus output optical properties using neural network trained on diffusion theory, where the input reflectance is obtained from Monte Carlo simulation with $g=0.9$, $n_{rel} = 1.0$. 1% random Gaussian noise was added to the reflectance prior to fitting. (a) μ_a. (b) μ_s'. Dotted lines demark relative errors of 10% and 20% for μ_s' and μ_a respectively.

Chapter 4 Instrumentation

The concept of the light detection system is depicted in Figure 4.1. Basically, light from a broadband source enters the medium from an optical fiber and is collected at several distances along the surface with other optical fibers. A more detailed schematic of the actual system and its components is given in Figure 4.2. The collected light is imaged through a monochromator onto a photodiode array as shown in Figure 4.1, such that the reflectance from all detectors is obtained simultaneously. The grating in the monochromator can be scanned to obtain reflectance at different wavelengths. The individual elements of the system are described in detail in the following sections.

4.1 Probe

A fibre optic probe was constructed (Fiberguide Industries, Stirling, New Jersey) which includes fibers for both delivery and detection of light. The face of the probe which is in contact with the sample is made of black Delrin. Holes for source and detector fibers were drilled out precisely in the pattern depicted in Figure 4.1. The nominal centre-to-centre source-detector distances are 1.0, 1.5, 2.0, 2.5, 3.0, 3.5, 4.0, 4.5, 5.0, 5.5, 6.0, 7.0, 8.0, 9.0, and 10.0 mm for a total of 15 distances. Multiple detectors were used at the largest three separations along a short arc of constant radius from the source fibre, as

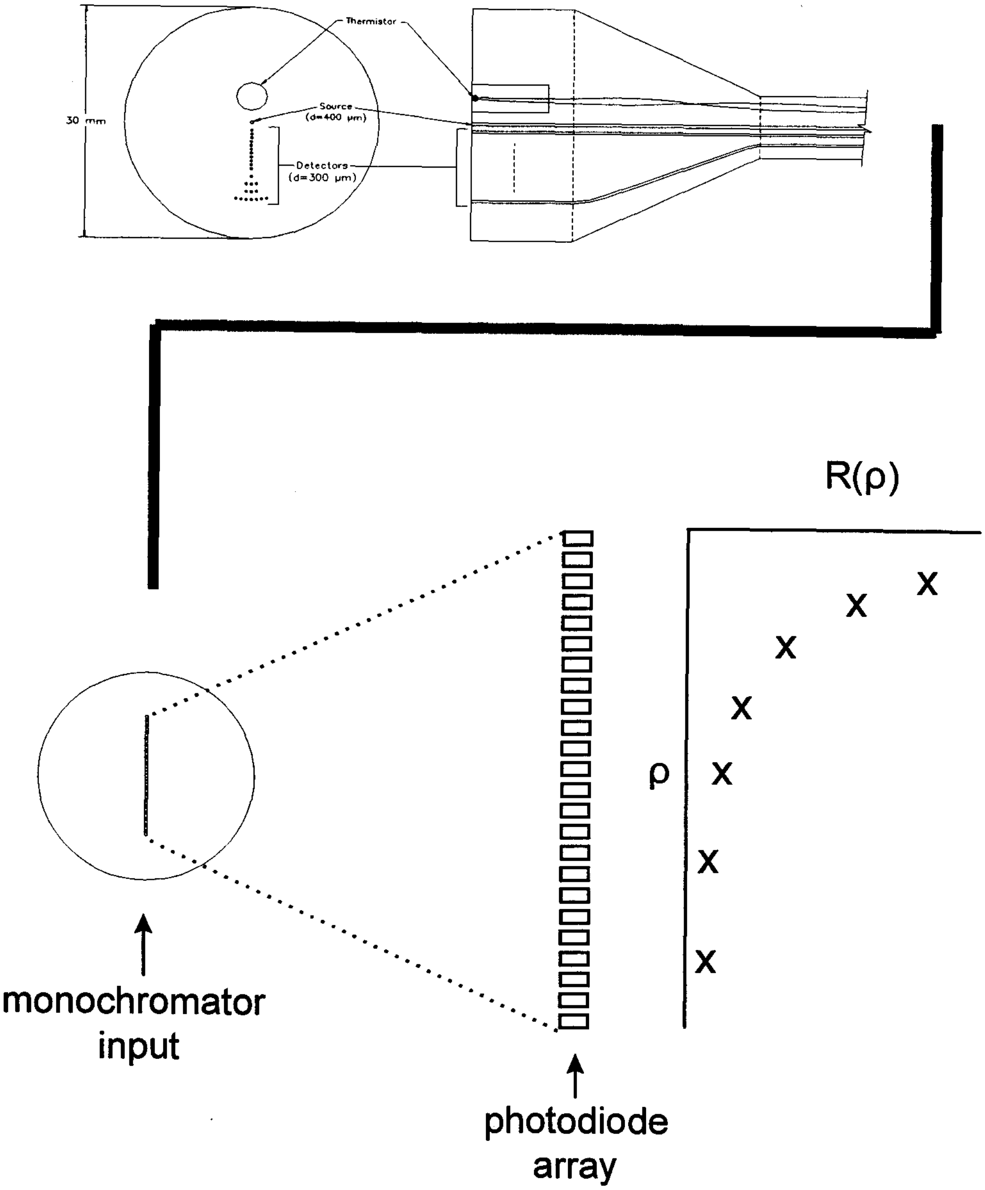

Figure 4.1 Spatially resolved diffuse reflectance measurement technique. A surface probe (top) is used for delivery (source) and detection of light. Detection fibres are coupled to elements of a second, linear fibre array (bottom) which is imaged through a monochromator onto a InGaAs photodiode array. This configuration yields R(ρ) for a single wavelength, but spectral information can be obtained by rotating the monochromator grating.

shown in Figure 4.1. At these distances, this increases the signal which can be very low for some of the materials and wavelengths under investigation. Including the multiple

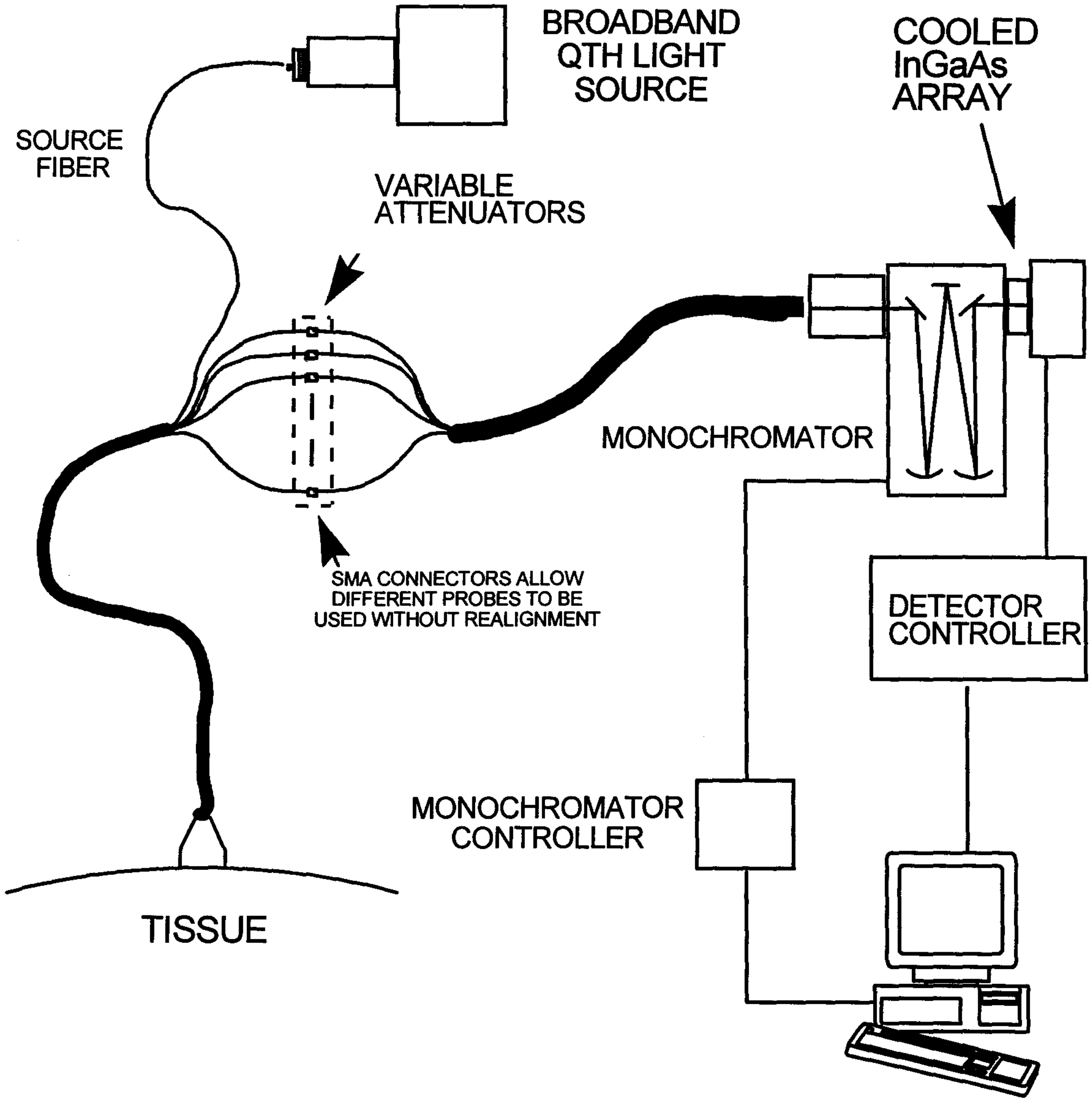

Figure 4.2 Schematic of system for measurement of spatially resolved diffuse reflectance.

detector distances, there are 25 detector fibres in total. The source and detection fibres are silica core, silica cladding with numerical aperture of 0.22. The fibres used for detection have 300 μm core diameter, while the source fibre has 400 μm core diameter. A larger source fibre was required to increase the amount of light detected. A thermistor (Omega Engineering, Quebec) was incorporated into the probe head for measurements of local skin temperature, and is also depicted in Figure 4.1. The thermistor was epoxied into an aluminum cup which was anodized and then inserted into the probe face. The fibres were inserted through the holes and fixed in place with optical epoxy. The face of the probe and fibres were then polished to a smooth finish. The fibres and thermistor leads were housed inside polyvinyl chloride monocoil for about 2.5 m, after which they were split into individual leads and terminated with SMA connectors (fibres) or BNC connector (thermistor) for convenient attachment and reattachment to the monochromator input assembly and temperature data acquisition system.

4.2 Light Detection and Imaging

Detected light from the probe is coupled to another fibre optic monochromator input assembly through fibre optic variable attenuators (OZ Optics, Nepean, Canada). The monochromator input (Fiberguide Industries, Stirling, New Jersey) consists of a linear array of fibres housed in an aluminum cylinder about 5 cm long and 2 cm in diameter. The end face has a matte black finish. The fibre is of the same size and type as the detector fibres of the probe. Individual fibres are separated by inactive spacing fibres to ensure that the individual tracks can be resolved on the detector array There are 25 active fibres to match the 25 detector fibres on the probe. It is advantageous to attenuate the light from the nearest distances so that the signal from the more distant detectors can be integrated over longer times without saturating the near detectors.

An imaging monochromator (Acton Research Corporation, Acton, Massachusetts) with a 200 g/mm grating centred at 1 μm is used to form the image of the linear input array onto the photodiode array The optics result in a magnification of approximately 1 The grating can be scanned to obtain a full range of wavelengths within the sensitive region of the detector, although the grating efficiency is significantly reduced for wavelengths less than 0.9 μm and greater than 1 3 μm.

A 512 element InGaAs photodiode array (Princeton Instruments, Princeton, New

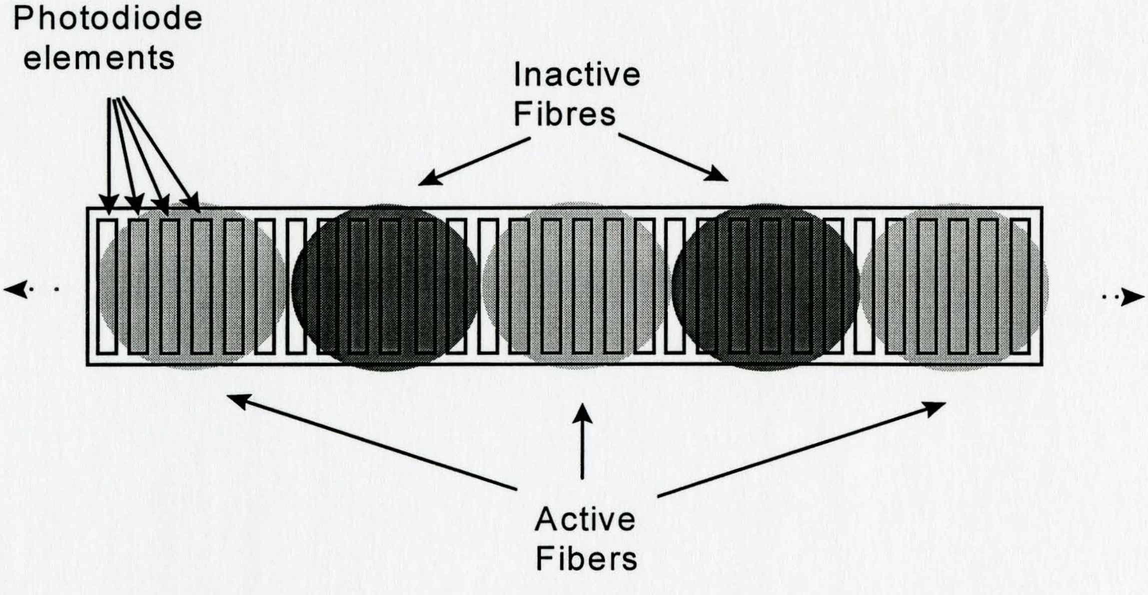

Figure 4.3 Imaging of fibre array onto photodiode array For clarity, the imaging scheme is shown without wavelength dispersion. Dark circles represent inactive, spacing fibres. Light circles represent active fibres coupled to detection fibres in the probe.

Jersey) is used to measure the light intensity. The long side of the array is oriented to match the monochromator input fibre array so that a single acquisition measures all detector intensities at a single wavelength. Figure 4.3 depicts how the fibre optic array is imaged onto the photodiode array. The pixels dimensions are 250 x 38 μm with 50 μm centre-to-centre spacing. The longer dimension is perpendicular to the array of imaged fibres. The detector is cooled to about -40° C using a coolant circulating unit and temperature controller. The readout is performed with a 15 bit A/D converter using spectroscopy software (Winspec, Princeton Instruments) supplied by the manufacturer.

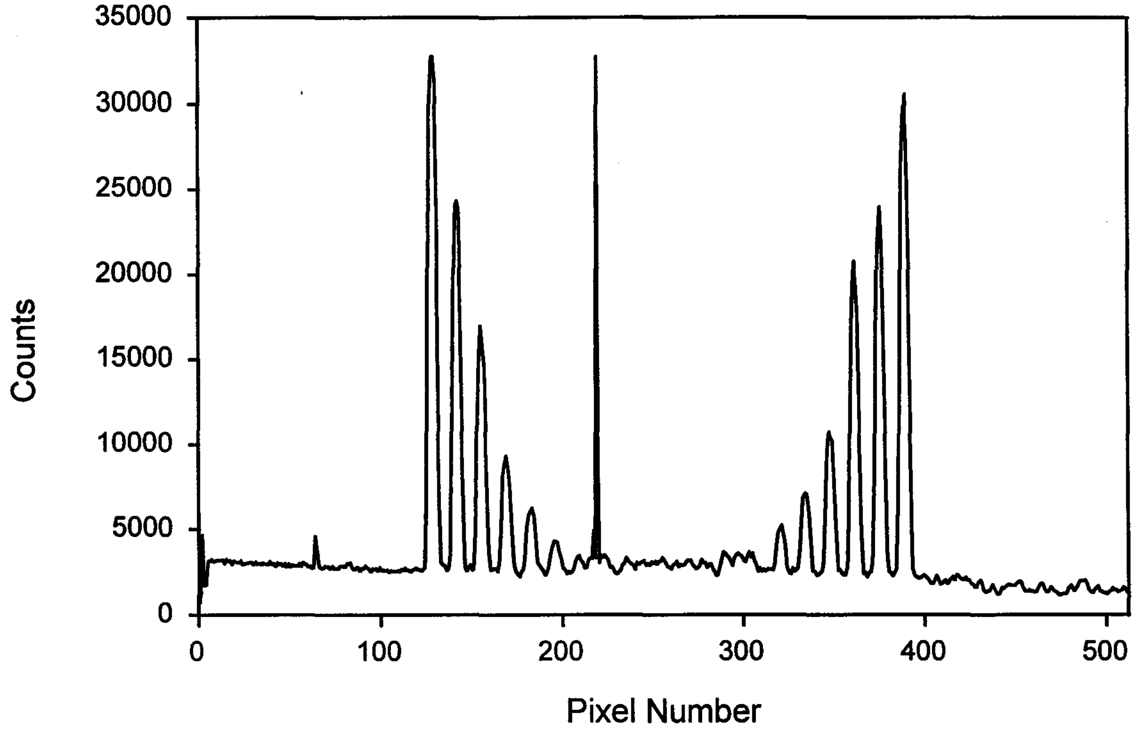

Figure 4.4 Typical photodiode array intensity profile. Each narrow peak corresponds to a detection fibre. The detectors are arranged so that the detectors closest to the light source are imaged onto the edges of the array, while the furthest detectors which sample the lowest intensity are imaged onto the centre of the array. The baseline counts are due to detector dark current and ambient light. The narrow spikes occurring at about pixel number 70 and 210 are due to bad photodiodes, and are bypassed in the binning procedures.

The data obtained are in the form of counts versus pixel number and appear as a series of peaks, each approximately 9 pixels wide, corresponding to the imaged fibres. A sample intensity profile for a typical acquisition is shown in Figure 4.4.

One of the limitations of the detection system is the high level of detector dark current. Dark current is a temperature dependent background arising from the thermally generated carriers in the semiconductor. Cooling the detector significantly reduces this dark current, but even when operating at -40° C, the background is significant. Each array element has a slightly different dark current, but on average the dark rate is about 1400 counts per element per second out of a possible 2^{15} (32,768) counts. This corresponds to 4% of the counts read out after a 1 second exposure to maximum unsaturated accumulation. If longer exposure times are required in a measurement, the relative contribution of dark current increases. The detector will be completely saturated by dark counts after about a 25 second exposure. The required exposure time is determined by the intensity of the source, throughput of the spectrometer (including fibre optics, imaging efficiency, and detector sensitivity) and the attenuation of the medium, which are all dependent on wavelength. With the light source output maximized, typical exposure times are 0.5 to 5 seconds.

The detector dark current and other contributions to background light such as ambient light leakage are subtracted from each exposure using a reference measurement in which the light source shutter is closed. In many measurement situations it is not practical to measure the dark current prior to each acquisition. Generally, a reference background measurement is acquired at the beginning of a sampling period, and applied

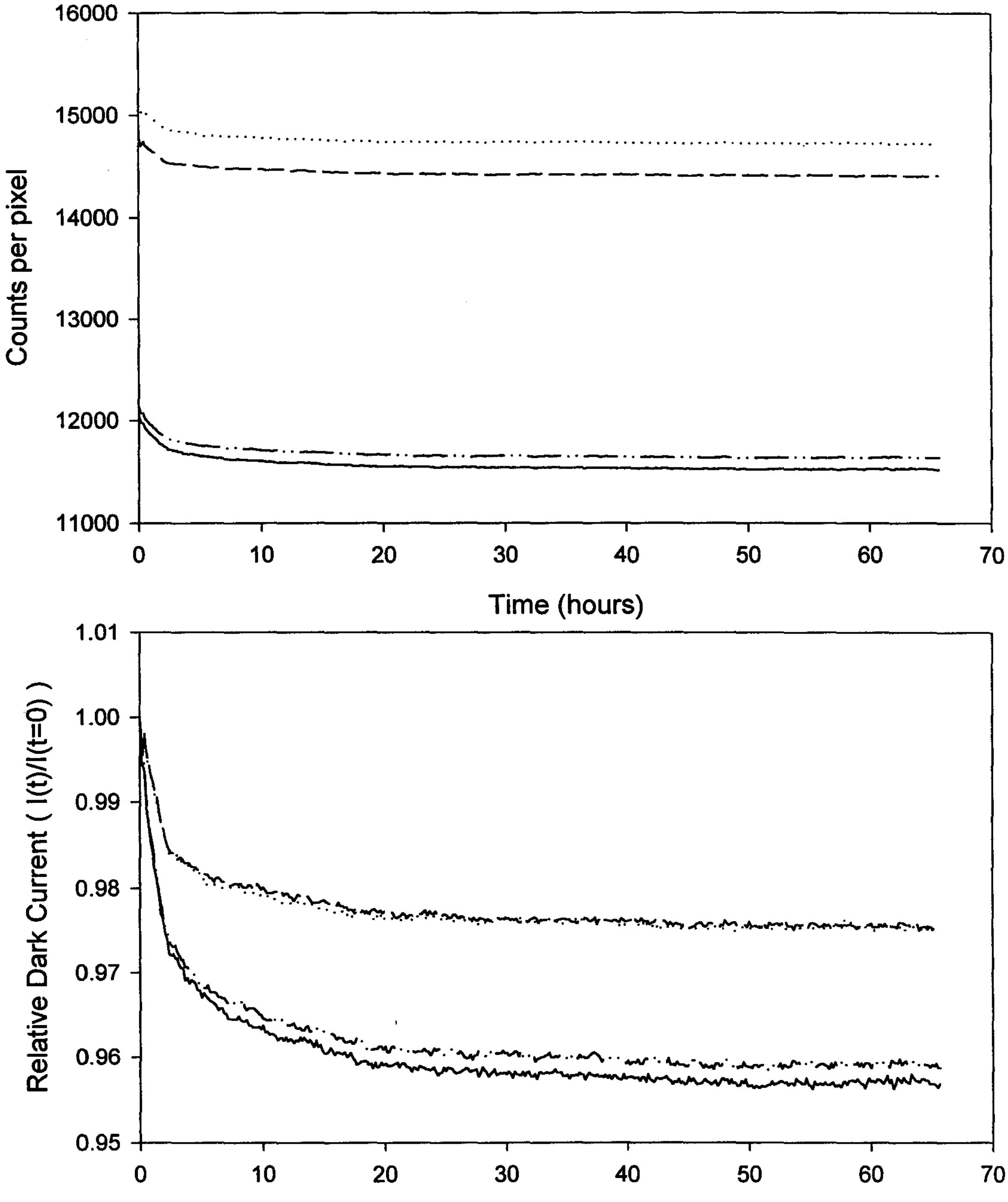

Figure 4.5 Detector dark current drift over time. Time in hours is with respect to the time when the coolant controller indicated a temperature lock status. Each of four curves represents (a), the average intensity or (b), the relative intensity of a group of several photodiodes from four different regions of the detector. The exposure time was 10 seconds.

to all measurements following, with the assumption that the background will remain constant over time. The manufacturer suggested a 1 hour stabilization period for the photodiode array to reach temperature equilibrium. However, long-term sampling of dark current indicated that the actual stabilization period may be several days, depending on the criteria applied. Figure 4.5 demonstrates the behaviour of intensities sampled over a long period, showing the initial drift downward in the measured counts.

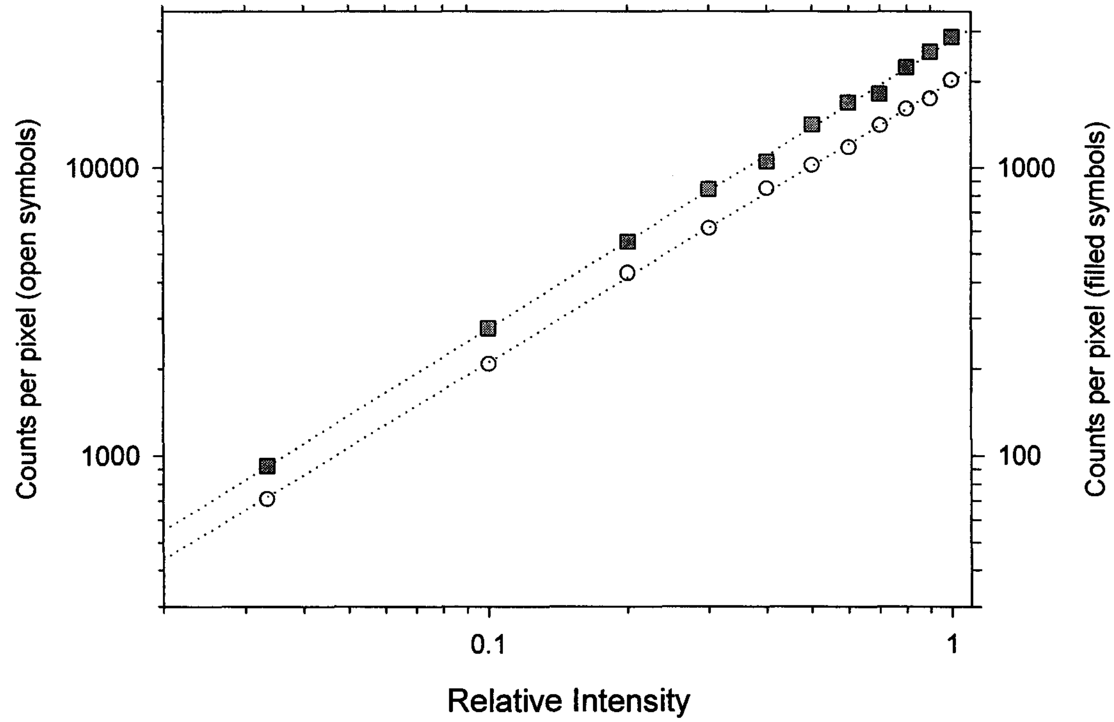

Figure 4.6 Linearity of detector response. A constant intensity light source was incident on the detector. Relative incident intensity was changed by changing the exposure time. All data has been background subtracted. Each curve shows the mean detected counts from a 3-pixel region as the relative intensity was varied over a range of high intensities (open symbols, left scale) or low intensities (filled symbols, right scale). Dotted lines are linear regressions performed on each curve.

It is important that the detector has a linear response to the amount of light it sees. A nonlinear response would make the system more difficult to calibrate. A measurement was performed in which the detector was exposed to a wide range of intensities, spanning the dynamic range of the readout. This was done by using a constant light source and changing the exposure time. Figure 4.6 shows the result of this measurement. The intensities were read from a few different pixels to verify that a linear response occurred across the detector. The intensities are shown on a log-log scale to show the full dynamic range.

4.3 Light Source

A 100 W broadband quartz tungsten halogen light source (Oriel Corporation, Stratford, Connecticut) was used in the experiments. The spectral irradiance curve for the lamp (published by the manufacturer) is shown in Figure 4.7. The light is focused into the source fibre of the probe and thus onto the skin for measurement. A 780 nm cut-on long-pass filter was placed in the path of the output collimated beam to prevent second order images of lower wavelength light overlapping the wavelength of interest. Since the detector sensitivity at lower wavelengths is extremely low, these contributions would be minor even without the filter.

The light source is equipped with a photo feedback intensity controller to prevent fluctuations in the output which occur due to changes in ambient temperature, as well as aging of the lamp. The photo feedback unit adjusts the lamp current to maintain a constant

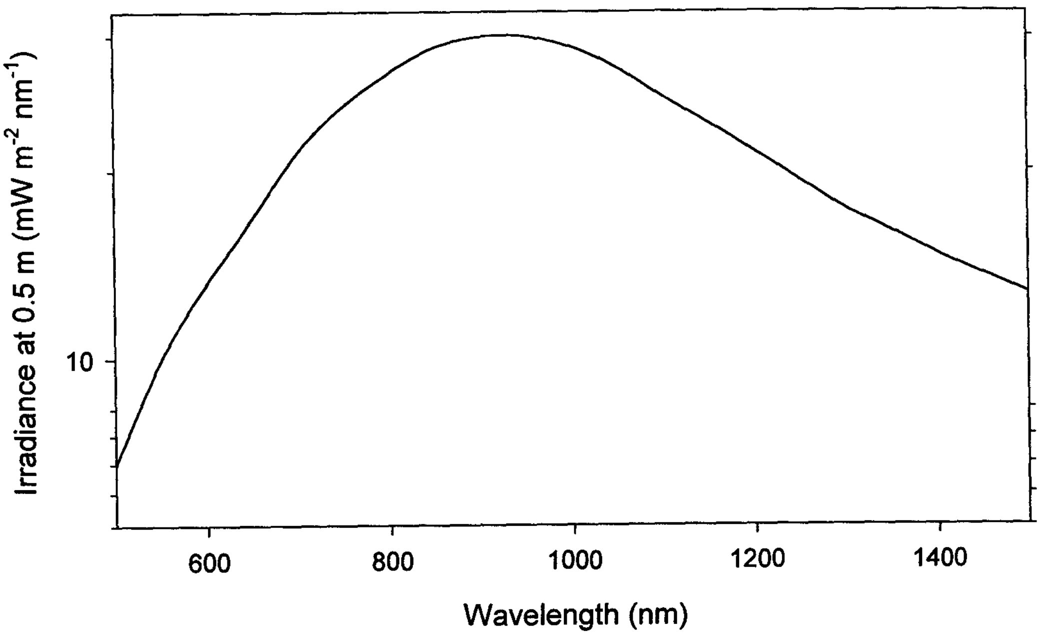

Figure 4.7 Spectral irradiance of 100 W quartz-tungsten-halogen lamp. Irradiance is given at a distance of 0.5 m (from Oriel Corporation product catalogue).

intensity reading on a temperature controlled photo detector located on the lamp housing. Even with the intensity controller, the lamp requires a burn-in period of about 1 hour before its output becomes temporally stable. Measurements are not taken until after this burn-in period as an added precaution. However, since the analysis of reflectance measurements is based on the relative reflectance, small changes in lamp intensity will be corrected by the normalization procedure.

The total power entering the sample was estimated by measuring the intensity of the source through a 400 μm fibre with the same properties as the source fibre of the surface probe. A 15 nm bandpass filter centred at 1064 nm was placed in front of the lamp for the intensity measurement, which was made using an IR-sensitive optical power meter (Newport Systems). The spectral irradiance curve shown in Figure 4.7 was scaled by this measured power, and then integrated using a lower limit of 780 nm. This yielded a total estimated power of 4.5 mW.

4.4 Track Attenuation

As described previously, fibre optic variable attenuators are used to couple the detector fibres from the probe to the fibres of the monochromator input assembly. It is possible to vary the attenuation of each track by a different amount. By doing this, it is possible to significantly increase the signal to noise ratio for data acquired from the furthest distances. The amount of light reaching the detector at 10 mm may be several orders of magnitude lower than that reaching the detector at 1 mm separation. Since the dynamic range of the instrument is only about four orders of magnitude, this situation would prevent acquisition of meaningful data at the further distances. By attenuating the light in the closer tracks, the exposure time can be increased without saturating the detector and more counts can be measured at the further detector distances.

The application of attenuation to selected tracks has the negative effect of increasing the dynamic range of the inter-detector calibration measurement, which is discussed in the next section. Therefore, the attenuation settings are adjusted to provide a reasonable dynamic range of intensities in both the calibration and sample measurements. The attenuation scheme can be optimized for a particular set of optical properties. However, in most measurements, data are obtained at several wavelengths with different optical properties and the attenuation scheme is based on a median set of optical properties for application at all wavelengths and samples.

4.5 Calibration

There are several factors which contribute to the final intensity which is read from the detector. Spectral efficiency curves for some of these factors are given in Figure 4.8. The optical fibres used in detection transmit some wavelengths of light more efficiently than others. The fibre optic attenuators reduce the amount of light transmitted in each detection track by a different amount. The spectrometer throughput has spatial and

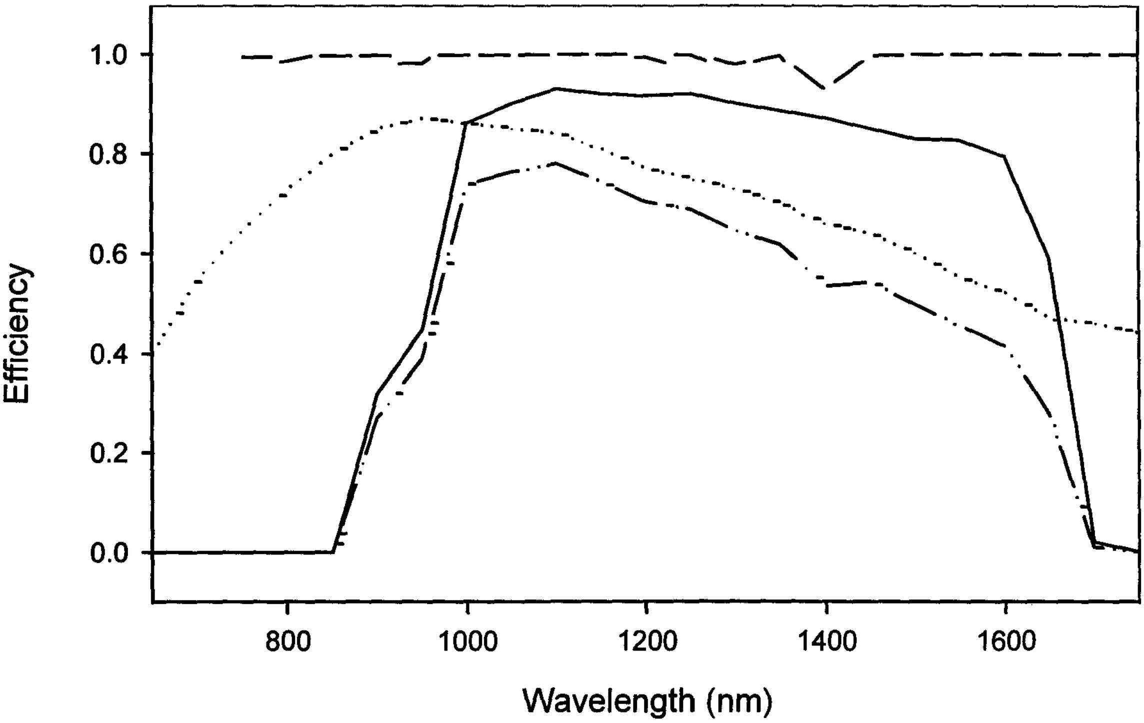

Figure 4.8 Factors contributing to total system response. Spectral response for the InGaAs detector (solid line), grating (dotted line), and detection fibre (dashed line) are shown. The combined response is also plotted (dash-dot line). Sources: Princeton Instruments (InGaAs detector response), Acton Research Corporation (grating response) and Fibreguide Industries (fibre response).

wavelength dependence. The photodiode array sensitivity also depends on wavelength and each photodiode array element may have a slightly different intensity response. Each detector track is imaged across several array elements, and the number of elements binned together for each track determines the final intensity reading for a measurement. In addition to these detection related factors, the exposure time, light source intensity, and sample optical properties also contribute to the intensity readings. Although the light source output does not contain any sharp spectral features, the intensity output decreases with increasing wavelength as shown in Figure 4.7. Longer exposure times can be used to compensate for decreased input light, at the expense of increasing the dark current contribution. In practice, the biggest single factor contributing to differences in relative detector response is the track-specific attenuation.

In theory it would be possible to characterize each of these individual factors, and then apply the combined spectral response to the measured intensities. However, there is a more practical technique which does not require individual characterization. In this calibration procedure, it is assumed that for some fluence $\psi(\lambda)$ incident on all detectors, the intensity reading should be the same. Any differences in measured intensity between tracks is a result of the combined response of the detection factors listed above. Since only relative track intensities are required for a measurement, it is only necessary to know the relative track response. The relative track response is obtained by placing the measurement probe on an output port of a 6" diameter integrating sphere which is illuminated by a fibre from the side. This arrangement provides uniform illumination of all detectors. The track intensities are sampled by the same technique as for a measurement, at all wavelengths of interest. The relative calibration factors for detection distance ρ and wavelength λ are thus:

$$C_{rel}(\rho,\lambda)=\frac{I(\rho,\lambda)}{I(\rho_o,\lambda)} \quad \textbf{(17)}$$

where I is the intensity measured with the probe on the integrating sphere, and ρ_o is any track selected as a reference. When using the calibration data to correct measurement data, it is sufficient to use the calibration intensities so that the unnormalized reflectance becomes:

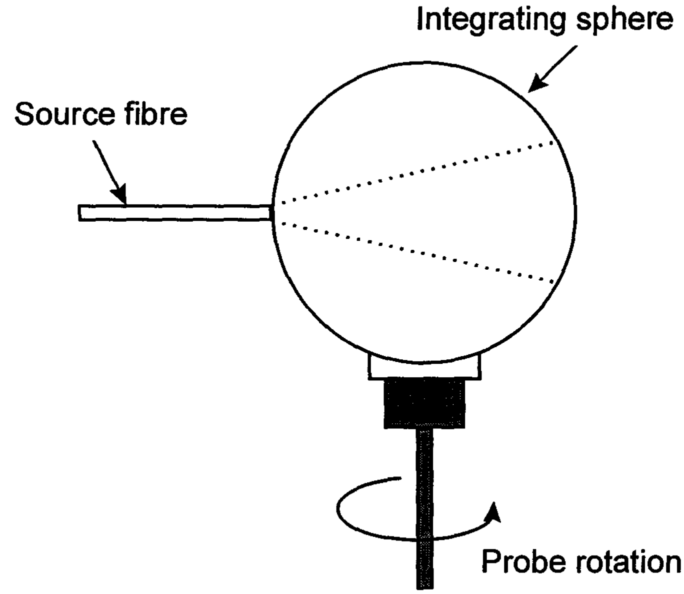

Figure 4.9 Experimental setup to evaluate uniformity of detector illumination.

$$R(\rho,\lambda)=\frac{I(\rho,\lambda)}{C(\rho,\lambda)} \quad \textbf{(18)}$$

where I(ρ,λ) is the intensity measured for distance ρ and wavelength λ on the sample.

An experiment was performed to establish that ψ(λ) was indeed sufficiently uniform across the port of the integrating sphere for calibration purposes. The probe was placed in the port of the integrating sphere with illumination from a port 90° adjacent. Measurements were obtained at different randomized rotations of the probe. The experimental setup for this measurement is depicted in Figure 4.9. The mean and relative

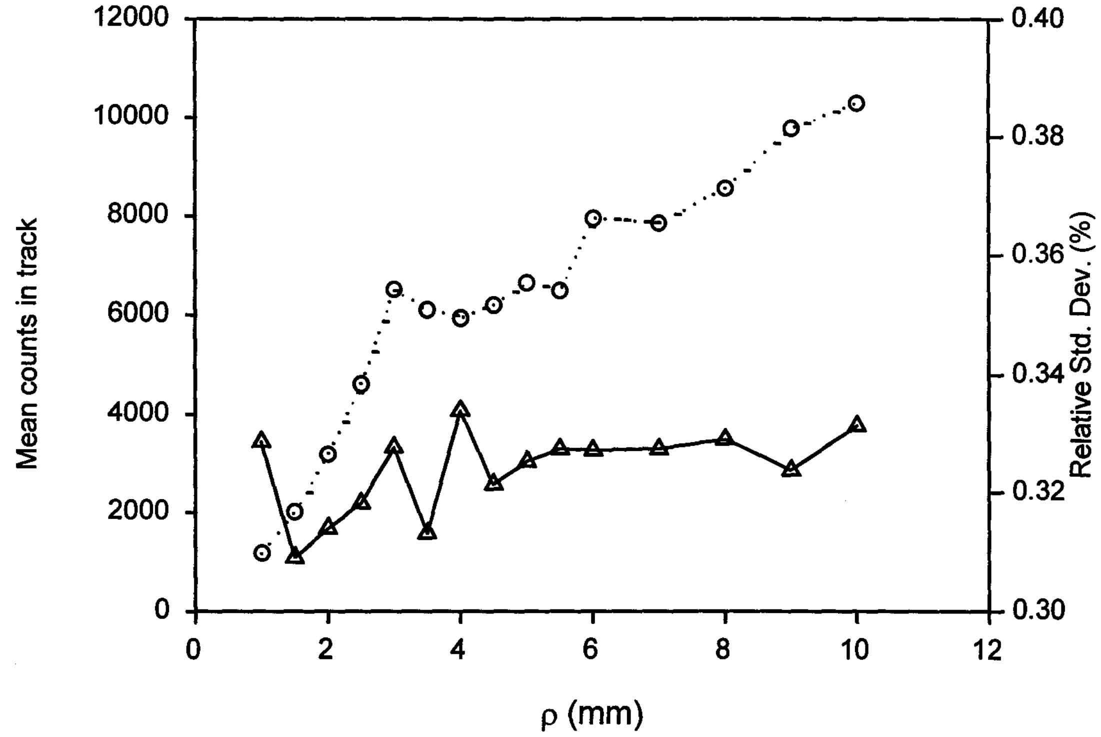

Figure 4.10 Output uniformity of integrating sphere used for inter-detector calibration. The mean (circles, left axis) and relative standard deviation (triangles, right axis) were calculated from intensities measured at 20 rotational positions. The intensity measurements were obtained with fibre attenuators in place, resulting in a large range of mean intensities. The relative standard deviation of the intensities was not strongly dependant on the track intensity, and was less than 0.34% for all tracks.

standard deviations of the measured track intensities for a series of 20 positions were calculated and are shown in Figure 4.10. The relative standard deviation was found to be less than 0.34% for all detectors. It should be noted that this experiment does not comprehensively determine the uniformity of the output, since each detector is always the same distance from the rotational axis.

4.6 Crosstalk Correction

An additional correction which must be made is the crosstalk resulting from imperfect imaging on the photodiode array. The image of a single fibre does not produce a perfectly sharp profile of the 300 μm diameter fibre core. Figure 4.11a shows the profile of a single detector, demonstrating this behaviour. Although most of the light falls within the main peak of the profile, there is sufficient light in the tails of the distribution falling onto other parts of the array to result in erroneous intensity readings in adjacent tracks. The pixels used for intensity integration are shown as shaded regions in Figure 4.11, demonstrating this effect, which is referred to as "crosstalk". This effect is enhanced when a high intensity track is adjacent to a low intensity track, leading to a large relative crosstalk into the lower intensity track. The degree of crosstalk depends on the attenuation of the sample, which determines the distribution of intensities across the photodiode array. For highly attenuating media, there is a large dynamic range of measured intensities, and crosstalk is worse. For less attenuating media, the distribution of intensities is more uniform, and the crosstalk effect is smaller.

An approximate correction for this crosstalk is obtained by subtracting the average intensity measured in the 3-4 pixel wide regions on either side of each fibre peak from the integrated intensity of the fibre peak itself. The correction can be quickly performed during data acquisition. This correction assumes that the combined crosstalk from all imaged detectors results in a slowly changing, continuous background on which the fibre profiles are superimposed. It is important to note that this correction is only approximate.

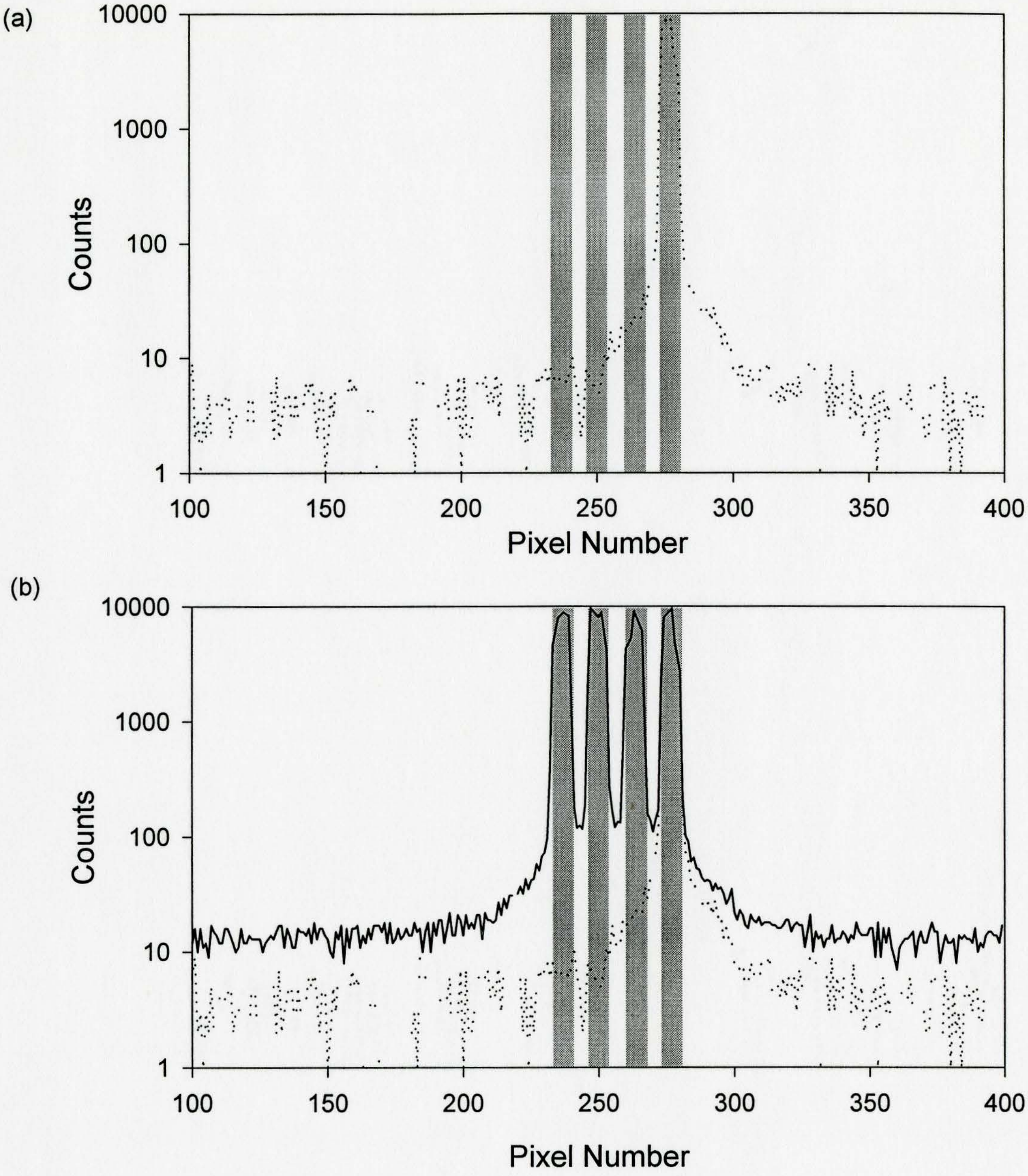

Figure 4.11 (a) Profile of a single fibre on the photodiode array, demonstrating the crosstalk effect. Shaded regions represent positions bins used for intensity integration. (b) The same profile is shown (dotted line) along with the profile of four adjacent fibres imaged on the array (solid line). The baseline shift is evident from comparison of these profiles.

A precise crosstalk correction would require fitting each peak and evaluating its crosstalk contribution to each track, based on its intensity. Such a procedure would be much more time consuming, would require storing more data, and would have to be incorporated as a post-acquisition processing step. An added advantage of the crosstalk correction is that it compensates for small changes in background that may occur during a lengthy measurement. The crosstalk correction decreases the signal to noise ratio of the reflectance data, since the low intensity crosstalk correction data is much noisier than the intensity data itself.

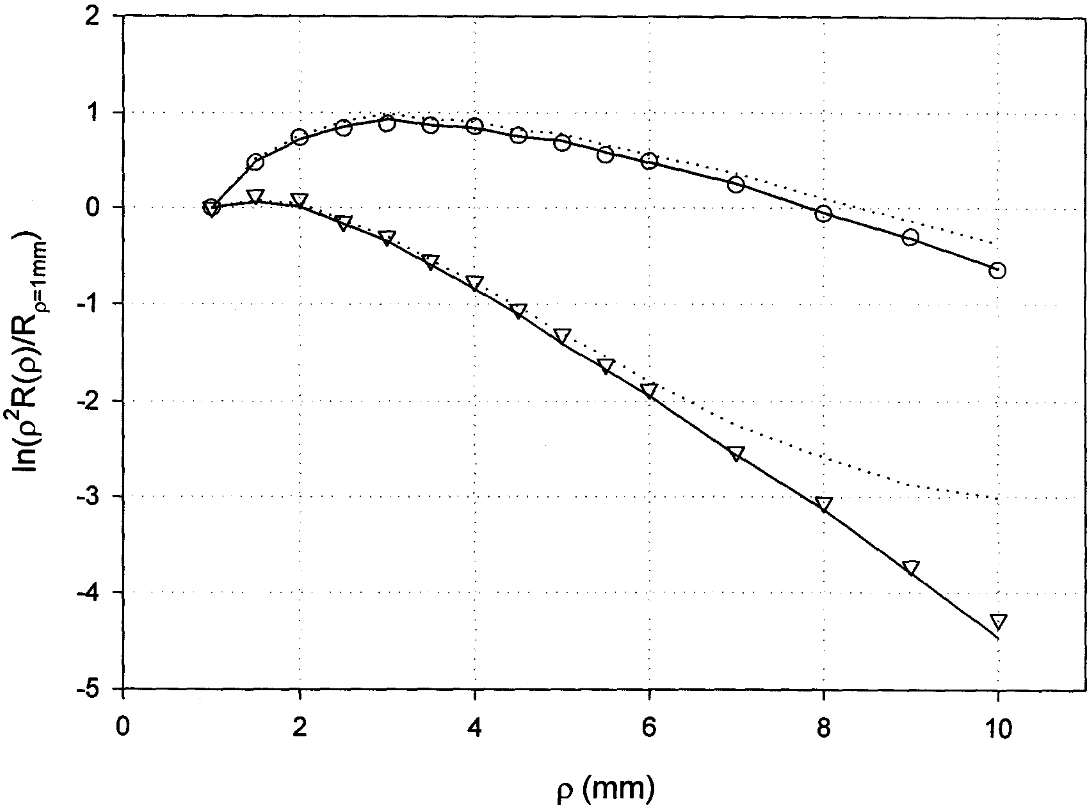

Figure 4.12 Validation of crosstalk correction. Markers represent data acquired with only one fibre imaged at a time. Lines represent reflectance acquired with all tracks imaged simultaneously before (dotted line) and after (solid line) performing the crosstalk correction. Data are shown for two samples with significantly different optical properties.

An experiment was performed to evaluate the accuracy of this crosstalk correction method. A measurement was acquired on a tissue-simulating phantom with and without the crosstalk correction. These data were compared to a measurement obtained in which there is no crosstalk. To do this, the intensity for each distance was acquired in sequence with all of the other tracks disconnected. This was performed at two wavelengths to compare different phantom attenuations. The results are plotted in Figure 4.12. It is apparent from this that the crosstalk corrected data is close to the 'ideal' data. This figure also demonstrates the greater severity of the crosstalk effect for more highly attenuating materials.

Chapter 5 Validation of Instrument and Technique

5.1 System Stability

The temporal stability of the measurement system is extremely important for applications such as monitoring. To evaluate the stability, a measurement was performed using a homogeneous tissue-simulating resin-based solid phantom. Spatially resolved reflectance data were sampled at selected wavelengths for more than 12 hours. There was no significant drift in the measured raw intensities over this period, as shown in Figure 5.1. The standard deviations of intensities ranged from less than 0.2 % for the nearer distances to about 1.0 % for the furthest distance, with no visible drift. It should be noted that these statistics, as well as those for *in vivo* measurements, depend on the wavelength and optical properties of the sample. In cases of extreme attenuation, such as the absorption peaks of water, the data at the furthest distances become quite noisy.

The optical properties for a phantom stability measurement were estimated using the nonlinear least-squares fit to diffusion theory described in Chapter 3. The results are plotted in Figure 5.2 for three selected wavelengths. No smoothing has been applied to the data so that the noise provides a visualization of the short-term variation in the estimated optical properties. The relative standard deviations of the optical properties for the three wavelengths shown are summarized in Table 5.1. In most cases the estimated optical properties are stable to within 1%. The stability of estimated μ_s' is better than that of μ_a by factors ranging from about 4 to 13. The analysis of fitting techniques presented in Chapter 3 showed that in general μ_s' can be more accurately determined than μ_a, which explains this difference in stability. Similar trends were noted by Farrell *et al* [1996] when estimating optical properties from theoretical reflectance data using a diffusion model.

Table 5.1 Phantom stability results at selected wavelengths.

	960 nm		**1060 nm**		**1250 nm**	
	μ_s'	μ_a	μ_s'	μ_a	μ_s'	μ_a
Mean	1.031	0.0420	1.013	0.0059	0.941	0.0464
Std. Dev.	0.0035	0.0006	0.0007	0.0001	0.0023	0.0005
$\frac{\textit{Std. Dev.}}{\textit{Mean}}$	0.0034	0.0149	0.0007	0.0092	0.0024	0.0113

5.2 Measurements of Aqueous Suspensions of Polystyrene Spheres

In order to demonstrate the ability of the technique to estimate optical properties of turbid media accurately it is necessary to perform measurements on samples for which the optical properties are known. Mie theory can be used to predict the scattering cross-sections and anisotropy of spherical particles of different sizes and refractive indices for different wavelengths of light [van de Hulst 1981]. A straightforward application is an

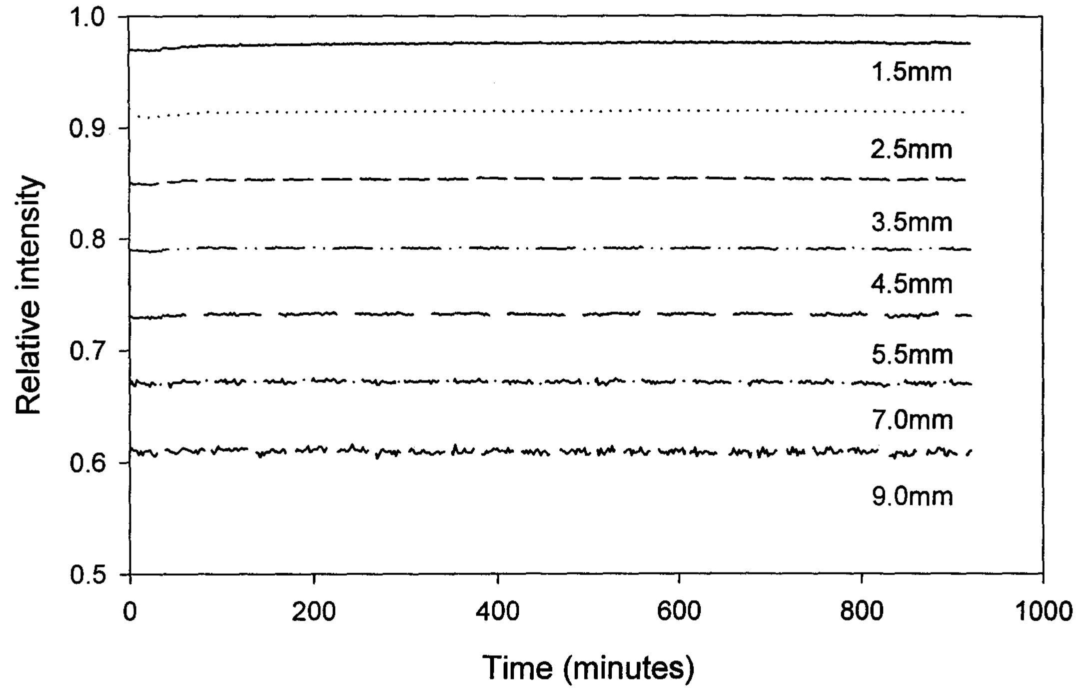

Figure 5.1 Intensities measured at selected source-detector separations on a solid phantom over a 12 hour period. Intensities are plotted relative to the initial intensity, and are offset for clarity.

aqueous suspension of mono-disperse non-absorbing polystyrene microspheres. A computer program was obtained from Ed Hull [University of Rochester] which applied Mie theory for this simple case. Input parameters to the program are particle radius, real refractive index of the particle, real refractive index of the suspending medium, and the range and increment of wavelengths required. Execution of the program produces a file containing the scattering cross-section, σ_s, the anisotropy, g, and the reduced scattering cross-section, $\sigma_s' = \sigma_s(1-g)$, for each wavelength. The reduced scattering coefficient of the suspension can be determined using the particle density, N_o:

$$\mu_s' = N_o \sigma_s' \qquad (19)$$

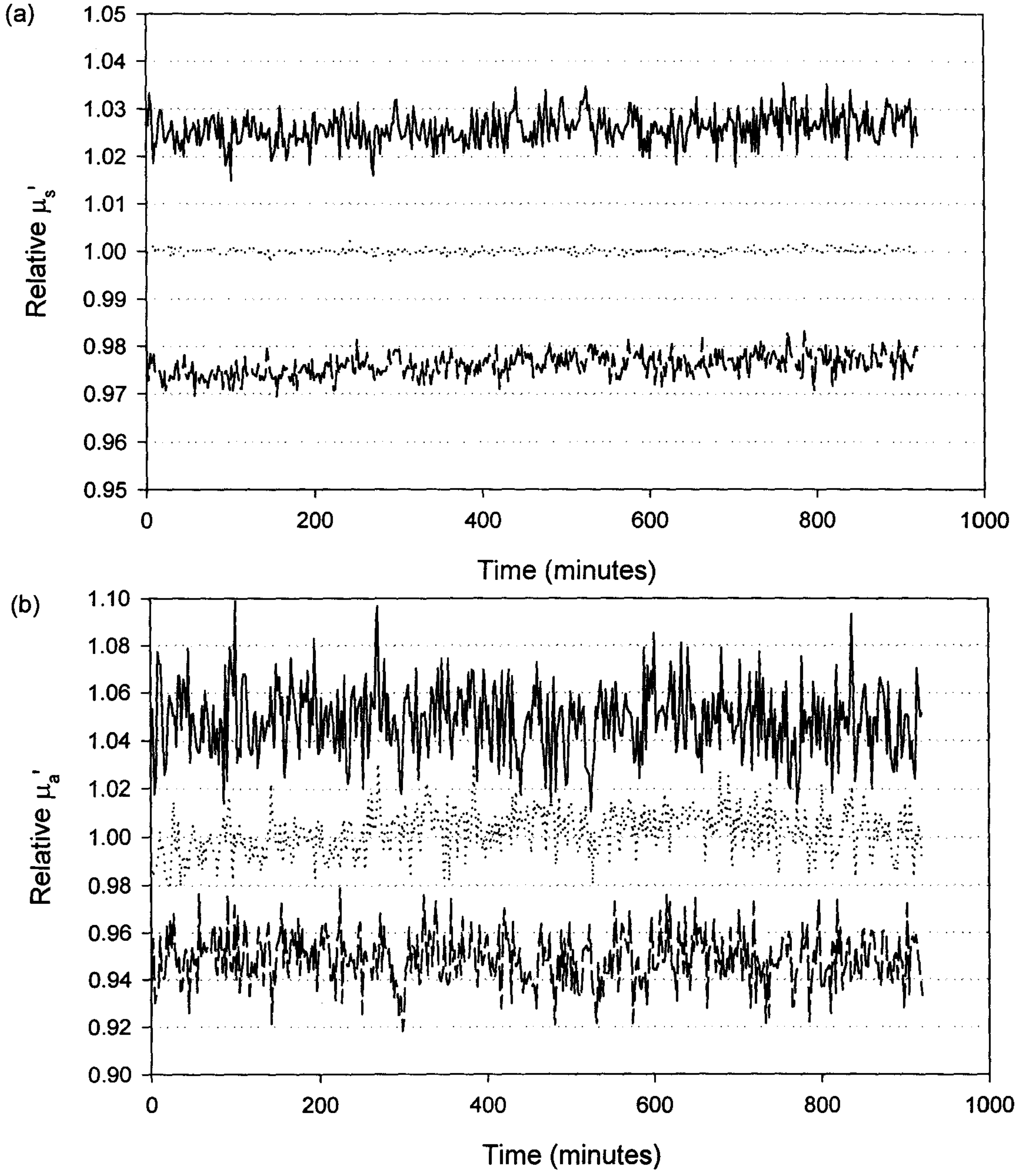

Figure 5.2 Estimated optical properties measured on a solid phantom for selected wavelengths. Optical properties were estimated using a nonlinear least-squares fit with the diffusion model (Equation 14). Three wavelengths are shown relative to the initial optical property, and offset for clarity. Top: 960 nm. Middle: 1060 nm. Bottom: 1250 nm.

The program was modified slightly to use the Cauchy dispersion formula for refractive index wavelength dependence to make the predictions more accurate over a large range of wavelengths. The general dispersion formula is [Weast 1989]:

$$n(\lambda)=A+B/\lambda^2+C/\lambda^4 \tag{20}$$

where $A_{polystyrene}$ = 1.566, $B_{polystyrene}$ = 7.85 x 10^3, $C_{polystyrene}$ = 3.34x10^9 [Duke Scientific 1996], A_{water} = 1.311, B_{water} = 1.154 x 10^4, and C_{water} = -1.132 x 10^9 [van Staveren *et al* 1991] and wavelength is in nanometres. The absorption coefficient of an aqueous suspension can be obtained from tabulated absorption spectra for pure water, such as Hale and Querry [1973].

Table 5.2 Concentrations and predicted scattering coefficients for polystyrene phantoms.

	Diameter (μm)	Particle Concentration (x 10^{10} mL^{-1})	Predicted μ_s' at 1000nm (mm^{-1})	Diameter (μm)	Particle Concentration (x 10^9 mL^{-1})	Predicted μ_s' at 1000nm (mm^{-1})
1	0.653	1.20±0.0067	0.465±0.0026	1.53	1.24±0.0051	0.432±0.0018
2	0.653	1.64±0.015	0.636±0.0059	1.53	1.72±0.014	0.599±0.0047
3	0.653	2.09±0.032	0.807±0.012	1.53	2.21±0.026	0.766±0.0092
4	0.653	2.42±0.0067	0.938±0.0026	1.53	2.70±0.0056	0.938±0.0019
5	0.653	2.84±0.025	1.10±0.0096	1.53	3.17±0.026	1.10±0.0089
6	0.653	3.27±0.054	1.27±0.021	1.53	3.63±0.048	1.26±0.016
7	0.653	3.70±0.063	1.43±0.024	1.53	4.10±0.055	1.42±0.019

Polystyrene spheres of diameter d=0.653 μm ± 0.0048 and d=1.53 μm ± 0.018 [Duke Scientific, Palo Alto, California] were used to make a series of phantom suspensions of different particle densities. Table 5.2 gives the concentrations and predicted Mie reduced scattering coefficients at a wavelength of 1000 nm. Figure 5.3 shows the predicted reduced scattering coefficients for the two particle sizes for the range of phantom concentrations measured.

The Mie program was also used to determine the wavelength dependence of the anisotropy factor for the two particle sizes used. The anisotropy factors for both particle sizes is graphed in Figure 5.4. This graph demonstrates the large difference in wavelength dependence of scattering phase functions for the two sizes. The large particles are highly forward scattering across the wavelength range of interest, while the smaller particle sizes become increasingly isotropically scattering with increasing wavelength. For data analysed with a diffusion model, the anisotropy of the particles is not considered, since only the transport scattering coefficient is considered. However, in Monte Carlo analysis methods an anisotropy factor is assumed when the simulation is performed. Errors may occur when Monte Carlo data for a fixed anisotropy are applied to analyse data over a wavelength range in which g changes significantly.

In addition to measurements performed with the spatially resolved diffuse reflectance spectrometer described in this thesis, the same phantoms were measured with another instrument which obtained similar data at a lower wavelength range of approximately 600-1000 nm. This provided an extended wavelength region for comparison of predicted optical properties versus measured, as well as a region of

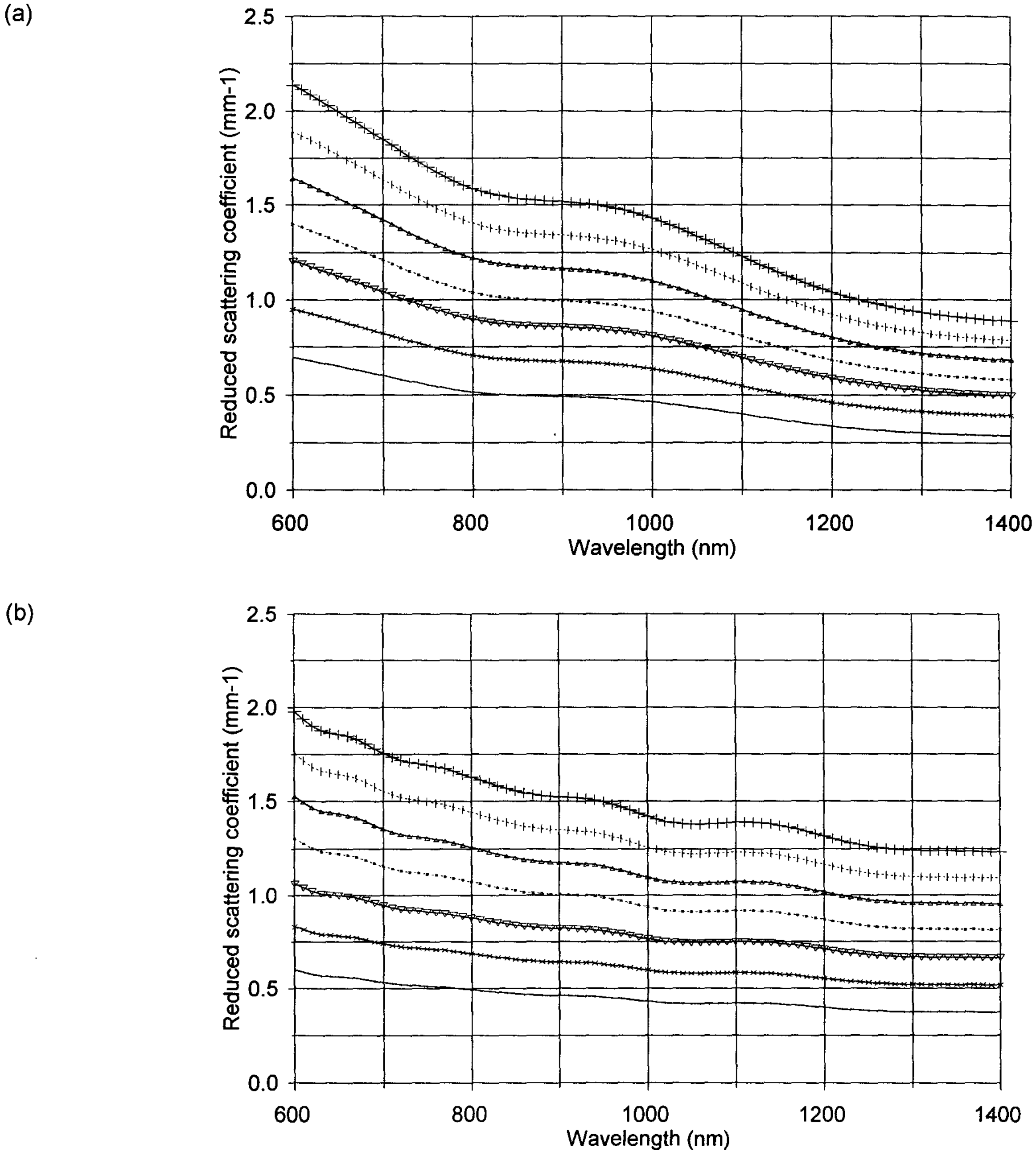

Figure 5.3 Calculated reduced scattering coefficients for suspensions of polystyrene spheres in water. Spheres were monodisperse with diameters (a) 0.653 μm and (b) 1.53 μm. Seven concentrations were prepared for each particle size as given in Table 5.2. Uncertainties in the reduced scattering coefficient (based on particle size distribution and dilution uncertainties) were smaller than the marker size for each sample.

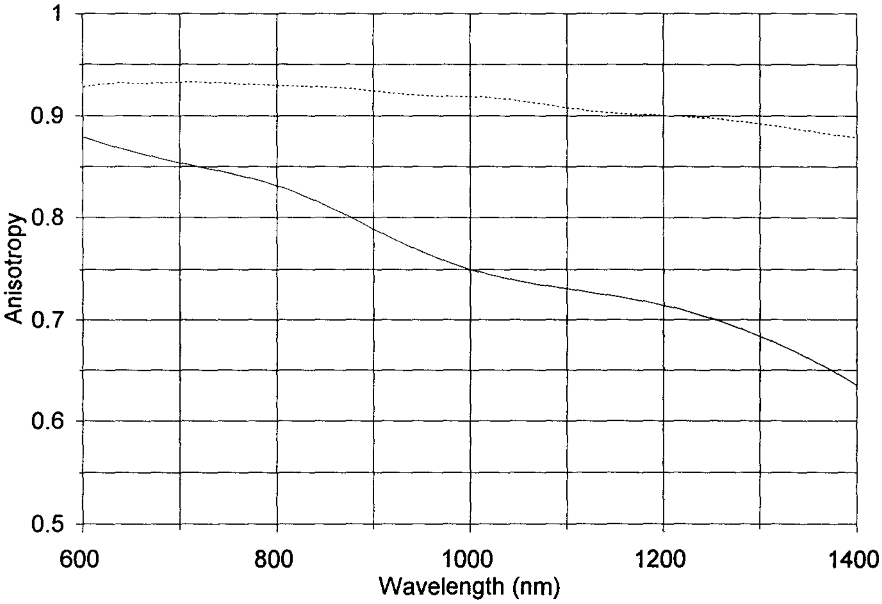

Figure 5.4 Wavelength dependence of the anisotropy factors (g) for polystyrene spheres. Solid line: 0.653 μm diameter spheres. Dotted line: 1.53 μm diameter spheres.

overlapping wavelengths where the two instruments should, in principle, measure the same reflectance. The lower wavelength system has been described in detail by Bruulsema *et al* [1997]. Basically, this system features a two-dimensional Si-CCD detector which allows for simultaneous acquisition of spatial and spectral information. A special probe was used for these measurements which was in principle the same as that described in Section 4.1. However, to allow for simultaneous measurements by both instruments, a second array of detection fibres alongside the existing array was implemented. The fibre array for this probe is depicted in Figure 5.5 The source fibre was then located along the line halfway between the two arrays. The source-detector distances for each array were kept the same as the previous probe. The second set of detection fibres was connected to the imaging input of the other instrument.

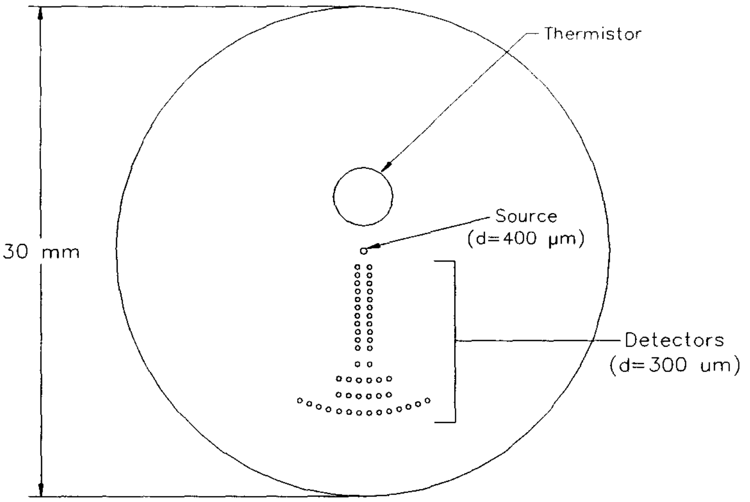

Figure 5.5 Diagram of probe used for dual system measurements. Each source-detector distance has detector(s) for the InGaAs and Si based light intensity measurement systems.

For measurements, the polystyrene sphere suspensions were poured into a square black container with dimensions 7x7x5.5 cm. Spatially resolved reflectance measurements were performed on all phantoms using a 10 nm scan resolution over the range of 900-1380 nm. The three methods described in Chapter 3 were used to estimate the optical properties from the reflectance data. In cases of strong attenuation, the furthest detectors were not used in the nonlinear fits since the signal to noise was so low. There is sufficient information in the close detector reflectance measurements to obtain a good estimate of the optical properties, while inclusion of the furthest points tends to prevent proper convergence. Data beyond about 1360 nm were extremely noisy due to strong water

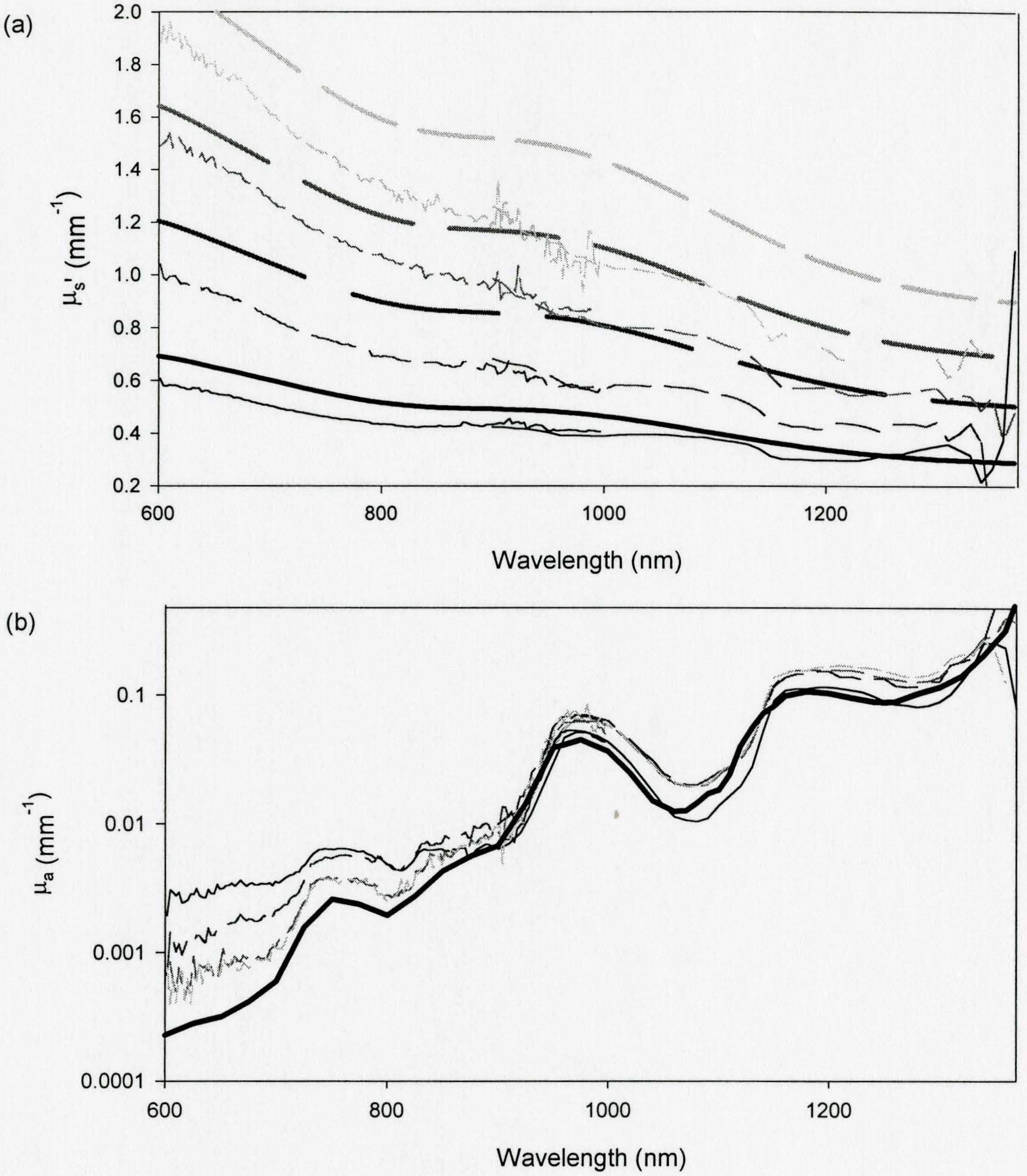

Figure 5.6 Measured μ_s' and μ_a spectra for selected aqueous suspensions of 0.653 μm polystyrene spheres. Optical properties were estimated using a nonlinear least-squares fit to a diffusion model (Equation 14). Actual μ_s' and μ_a are shown as heavy lines. Spectra are shown, in decreasing grey level, for particle concentrations of 1.20x10^{10} mL^{-1}, 2.09x10^{10} mL^{-1}, 2.84x10^{10} mL^{-1}, and 3 70x10^{10} mL^{-1} Actual and measured μ_s' for the same particle concentration are shown in matching grey levels, as are μ_s' and μ_a.

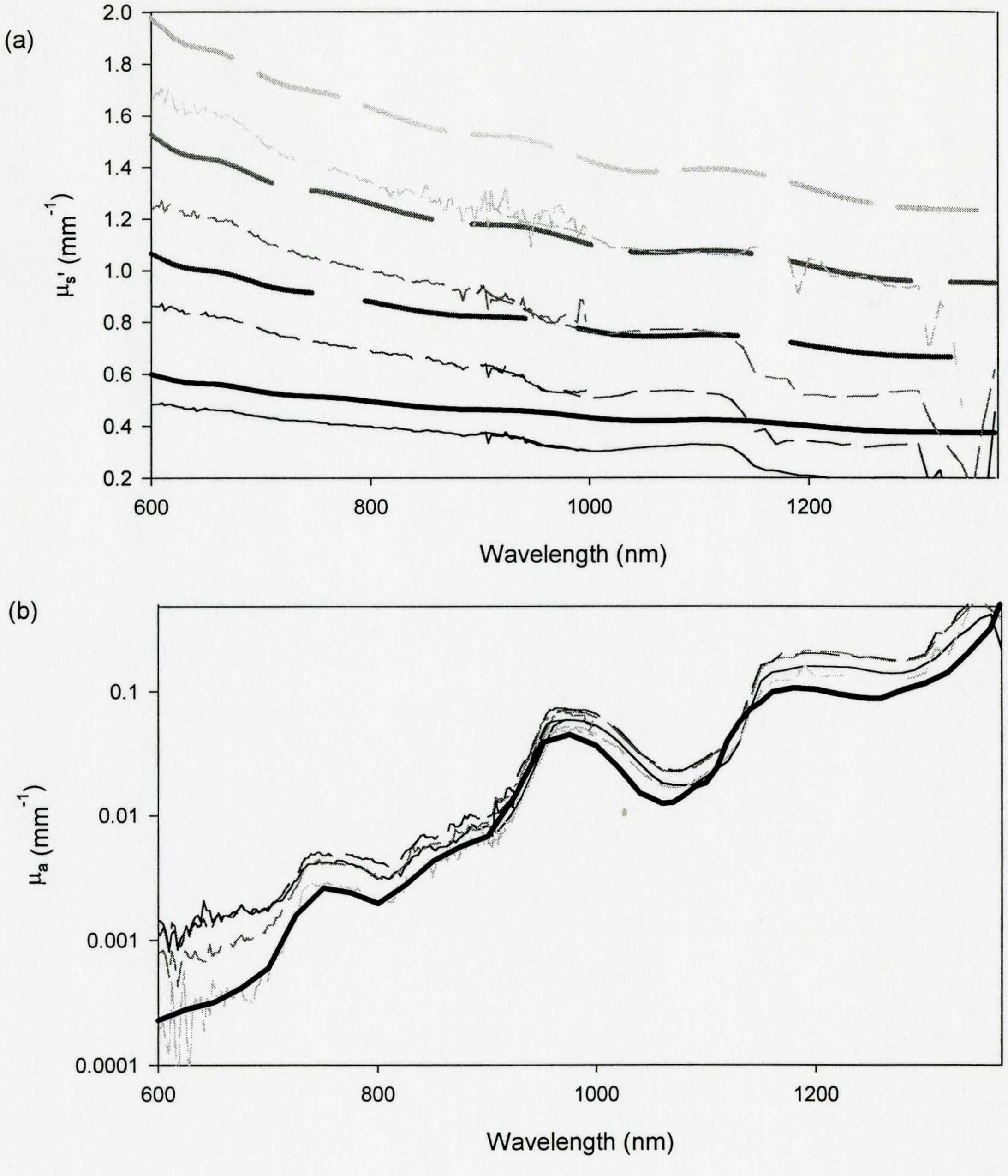

Figure 5.7 Measured μ_s' and μ_a spectra for selected aqueous suspensions of 1.53 μm polystyrene spheres. Optical properties were estimated using a nonlinear least-squares fit to a diffusion model (Equation 14) Actual μ_s' and μ_a are shown as heavy lines. Spectra are shown, in decreasing grey level, for particle concentrations of 1.24x10^9 mL^{-1}, 2.21x10^9 mL^{-1}, 3 17x10^9 mL^{-1}, and 4.10x10^9 mL^{-1} Actual and measured μ_s' for the same particle concentration are shown in matching grey levels, as are μ_s' and μ_a.

absorption, and the parameters extracted at these wavelengths are suspect.

The scattering and absorption spectra for selected phantom concentrations are shown in Figures 5.6 (0.653 μm spheres) and Figure 5.7 (1.53 μm spheres) for the optical properties estimated using a nonlinear least-squares fit to diffusion theory. The theoretical optical properties are shown for comparison. It is apparent from these curves that there is a tendency to underestimate the scattering coefficient at all wavelengths. Some of the features in the scattering coefficient appear to compare well with the theoretical curves, but at the longer wavelengths there are features which may be related to the peaks in the absorption spectrum. The water absorption features are reproduced well in the measured coefficients, but there is a tendency to overestimate μ_a. Also, as the scattering coefficient increased with increasing particle concentration, the estimated absorption increased, even though the water concentration has not increased. These trends were similar when the other methods of optical property extraction were used. Figures 5.6 and 5.7 demonstrate a reasonably good overlap in estimated coefficients between the two measurement systems in the wavelength region spanning 900-1000 nm.

The discrepancies between the estimated coefficients and the predicted coefficients were determined for each fitting method used. In Figure 5.8 and 5.9 the fractional error in estimated μ_s' is plotted versus the known value of μ_a for the small and large spheres. Selected wavelengths were chosen to provide the range of theoretical absorption coefficients. These figures demonstrate that the discrepancy in μ_s' is smaller for lower

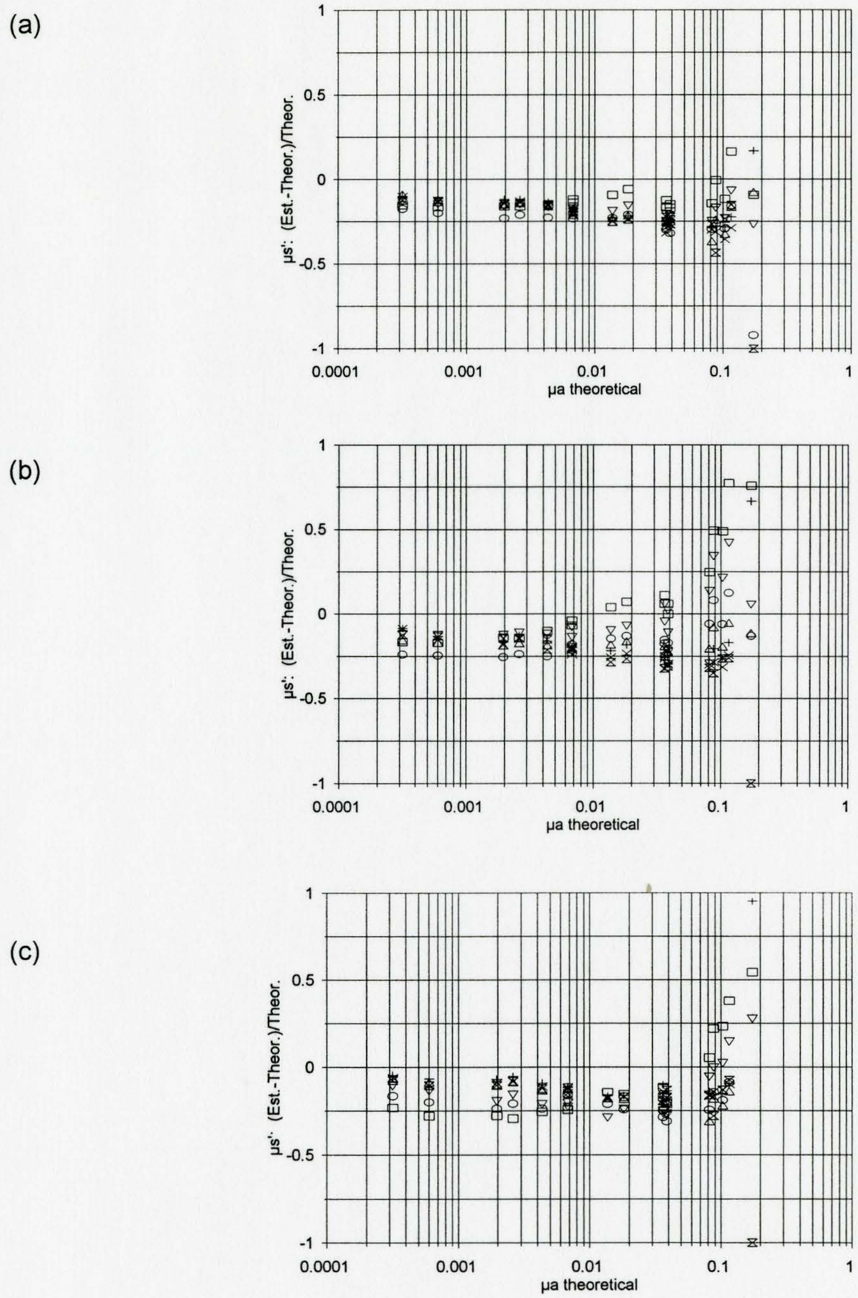

Figure 5.8 Fractional error in estimated μ_s' versus theoretical μ_a for suspensions of 0.653 μm polystyrene spheres Optical properties were estimated using (a) nonlinear least-squares fit to a diffusion model, (b) neural network fit to diffusion model and (c) nonlinear least-squares fit to 'Mono Monte Carlo' simulation. Data for seven particle concentrations (see Table 5.2) are shown in order of increasing concentration as markers: □, ▿ ,○, ▵, +, X, ⋈

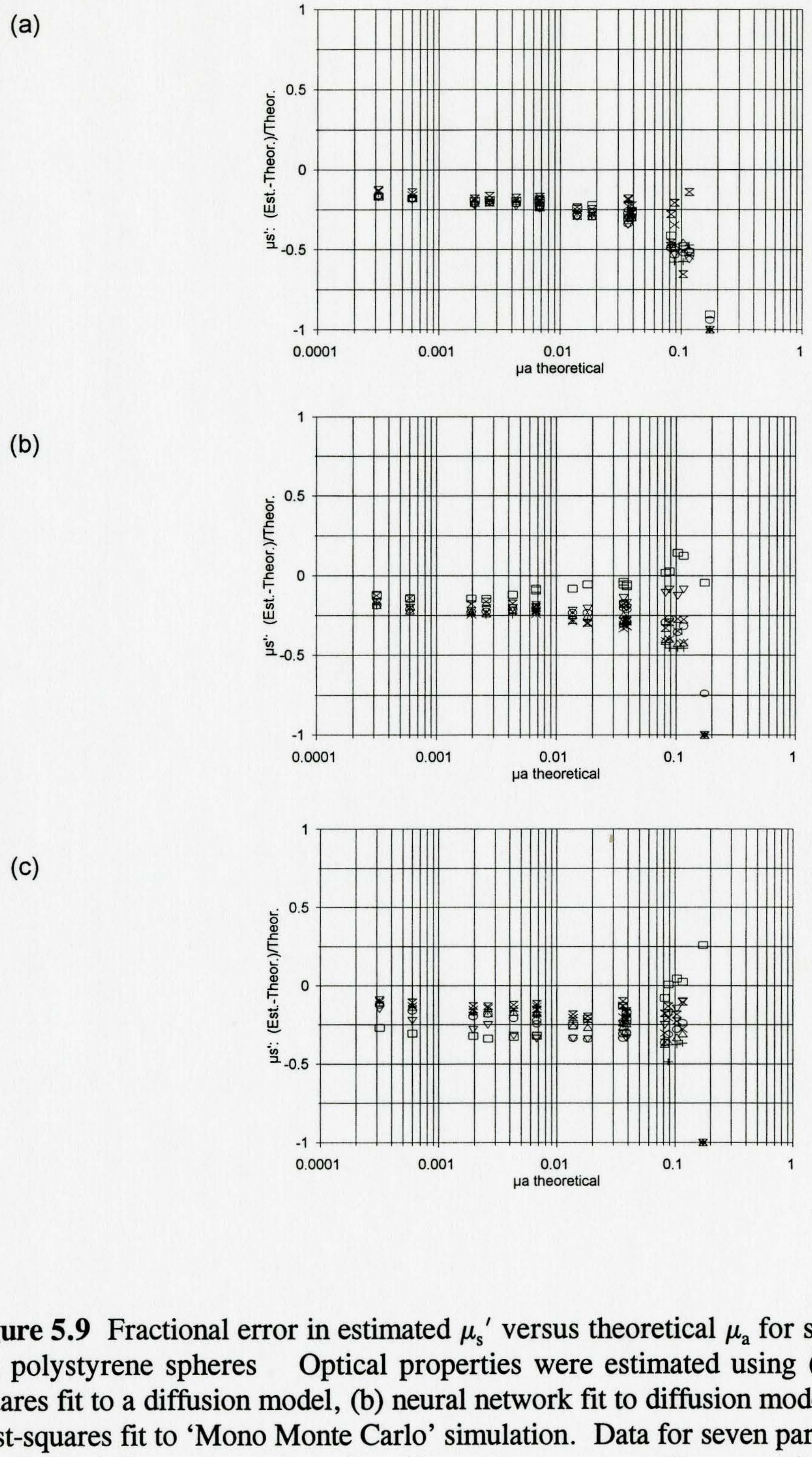

Figure 5.9 Fractional error in estimated μ_s' versus theoretical μ_a for suspensions of 1.53 μm polystyrene spheres Optical properties were estimated using (a) nonlinear least-squares fit to a diffusion model, (b) neural network fit to diffusion model and (c) nonlinear least-squares fit to 'Mono Monte Carlo' simulation. Data for seven particle concentrations (see Table 5.2) are shown in order of increasing concentration as markers. □, ▽ ,○, △, +, X, ⋈.

values of μ_a. For theoretical μ_a less than 0.01 mm^{-1}, the discrepancy is lower than 25% for all fitting techniques used for most phantoms, while for larger μ_a the discrepancy exceeded 50% in some cases. The large particle phantoms resulted in slightly lower discrepancies than the small particle phantoms for larger μ_a. In Figure 5.10 and 5.11 the fractional error in estimated μ_a is plotted versus the true value of μ_a for both particle sizes. For low absorption coefficients the discrepancies were quite large, and in many cases μ_a was overestimated by factors of 2 or more. This is in part because it is difficult to determine the absorption coefficient accurately when absorption is a negligible process compared to scattering. The absolute error in these estimated coefficients is still very small. Even for higher theoretical absorption, however, the discrepancy still approaches 100% in some cases.

Figure 5.12 and 5.13 show the fractional error in estimated μ_s' versus the predicted μ_s'. Data were selected from the same range of wavelengths as used in the analysis above. All three fitting methods show a clear dependence of the discrepancy on the predicted μ_s'. For low μ_s', μ_s' is overestimated, in some cases by more than 50%. For μ_s' greater than about 0.6 mm^{-1}, μ_s' is underestimated by 10-40%. These trends are similar to but more extreme than the trends observed when measuring the performance of the different fitting algorithms, as shown in Figures 3.1 and 3.4. It would be reasonable to expect that larger errors in μ_s' would occur for low scattering phantoms when applying a diffusion approximation for photon transport. However, a similar distribution of discrepancies was found when the Monte Carlo fitting technique was applied. Figure 5.14 and 5.15 plot the fractional error in estimated μ_a versus the theoretical reduced scattering coefficient. For

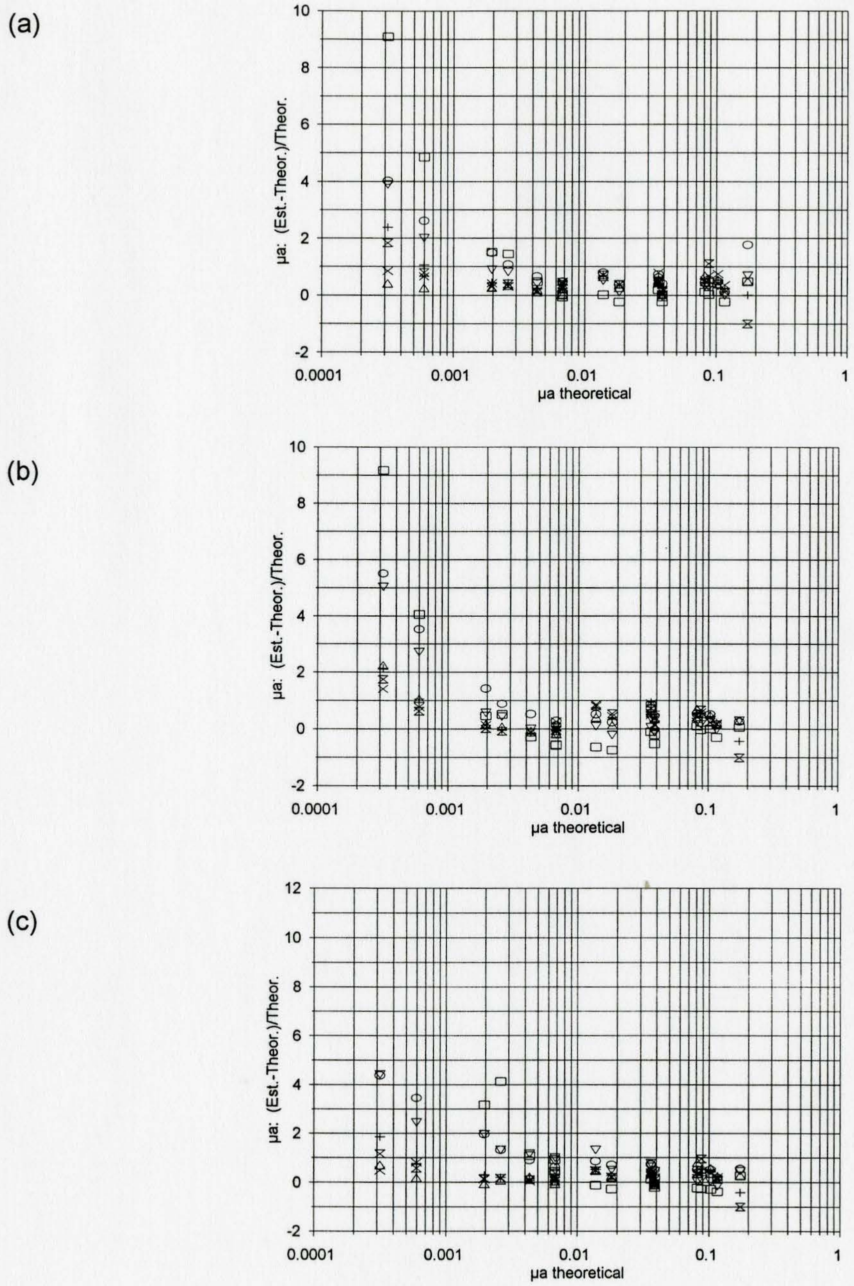

Figure 5.10 Fractional error in estimated μ_a versus theoretical μ_a for suspensions of 0.653 μm polystyrene spheres Optical properties were estimated using (a) nonlinear least-squares fit to a diffusion model, (b) neural network fit to diffusion model and (c) nonlinear least-squares fit to 'Mono Monte Carlo' simulation. Data for seven particle concentrations (see Table 5.2) are shown in order of increasing concentration as markers: □, ▿ ,○, ▵, +, X, ⋈

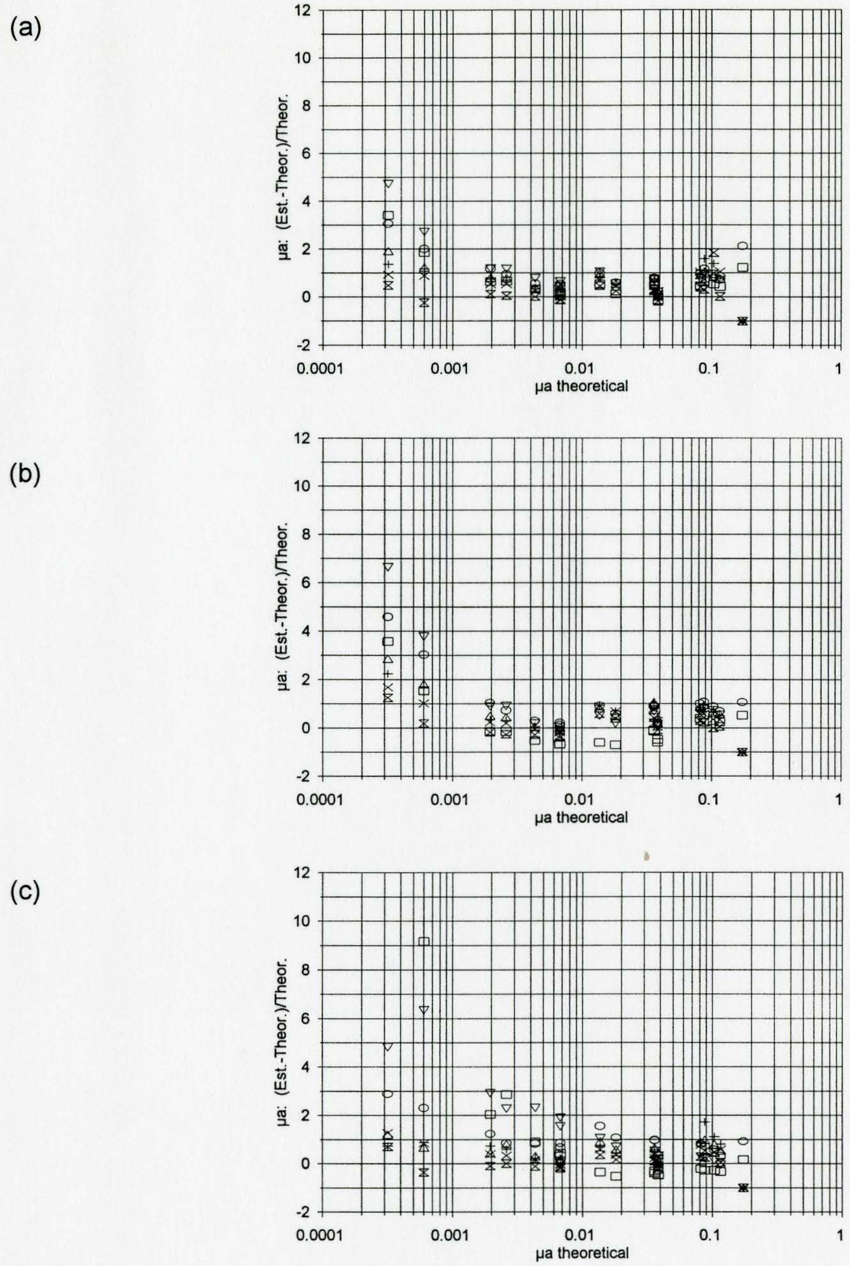

Figure 5.11 Fractional error in estimated μ_a versus theoretical μ_a for suspensions of 1.53 μm polystyrene spheres Optical properties were estimated using (a) nonlinear least-squares fit to a diffusion model, (b) neural network fit to diffusion model and (c) nonlinear least-squares fit to 'Mono Monte Carlo' simulation. Data for seven particle concentrations (see Table 5.2) are shown in order of increasing concentration as markers: □, ▿ ,○, ▵, +, X, ⋈

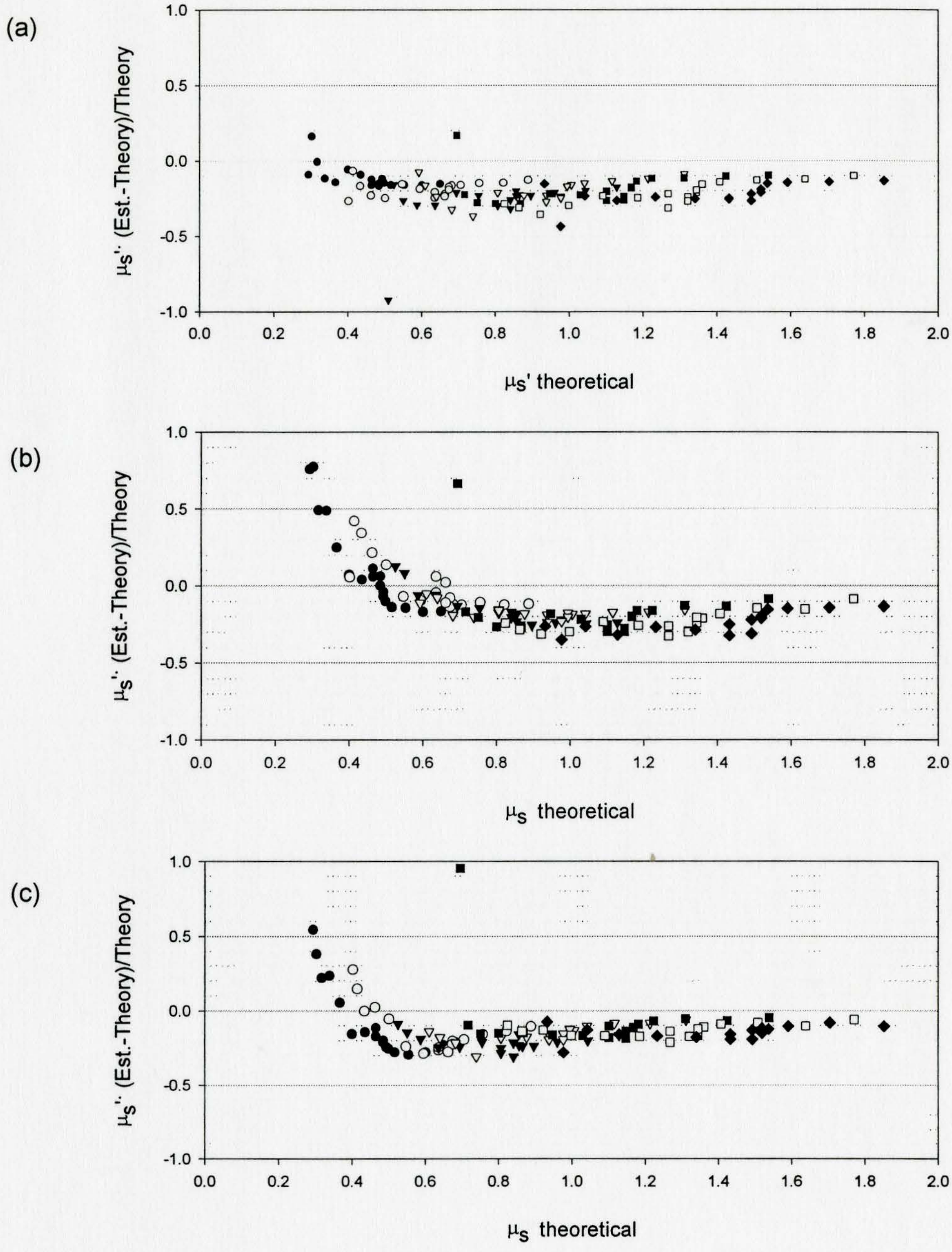

Figure 5.12 Fractional error in estimated μ_s' versus theoretical μ_s' for suspensions of 0.653 μm polystyrene spheres Optical properties were estimated using (a) nonlinear least-squares fit to a diffusion model, (b) neural network fit to diffusion model and (c) nonlinear least-squares fit to 'Mono Monte Carlo' simulation. Data for seven particle concentrations (see Table 5.2) are shown in order of increasing concentration as markers. ●, ○, ▾, ▿, ■, □, ♦

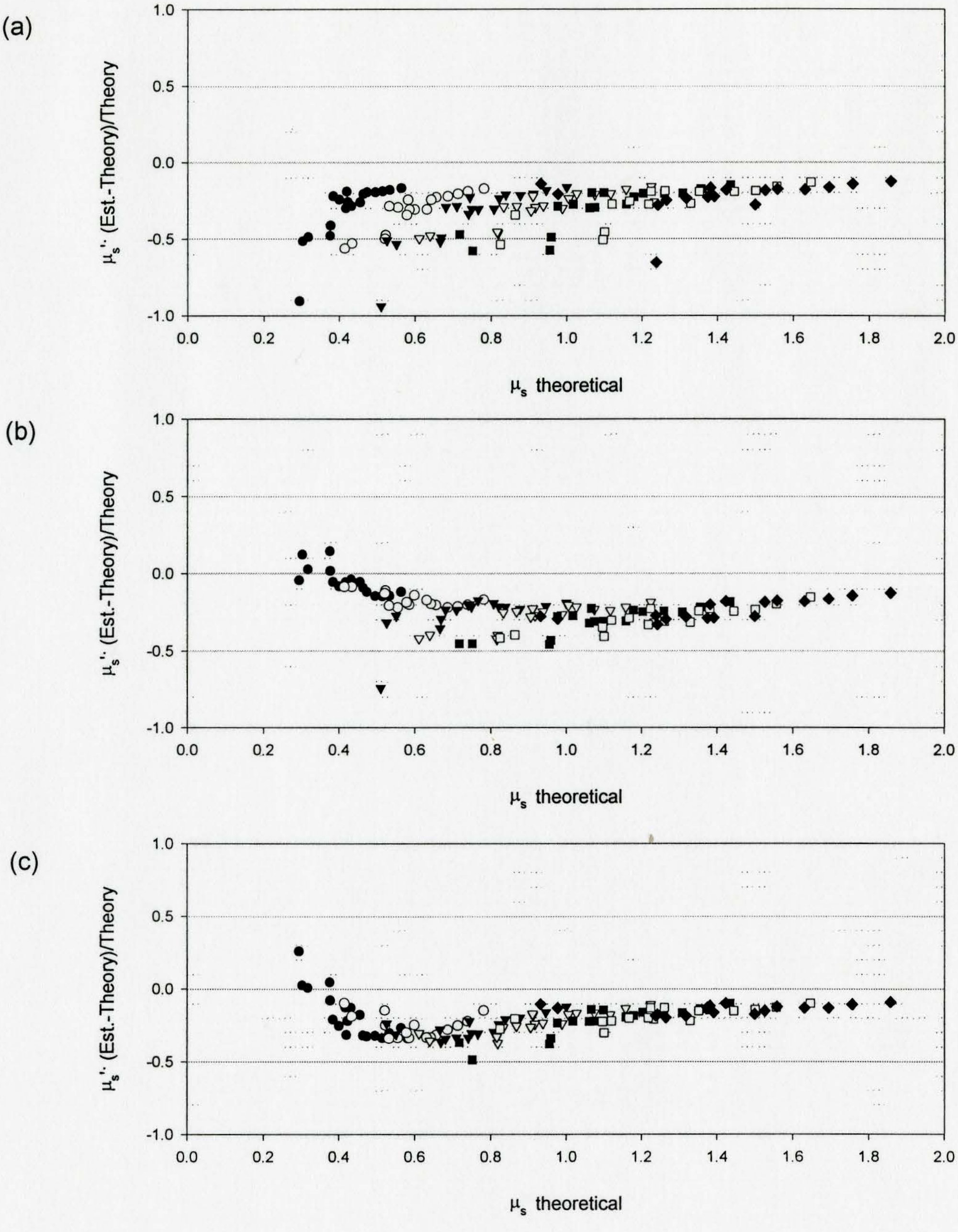

Figure 5.13 Fractional error in estimated μ_s' versus theoretical μ_s' for suspensions of 1.53 μm polystyrene spheres Optical properties were estimated using (a) nonlinear least-squares fit to a diffusion model, (b) neural network fit to diffusion model and (c) nonlinear least-squares fit to 'Mono Monte Carlo' simulation. Data for seven particle concentrations (see Table 5.2) are shown in order of increasing concentration as markers. ●, ○, ▾, ▿, ■, □, ◆

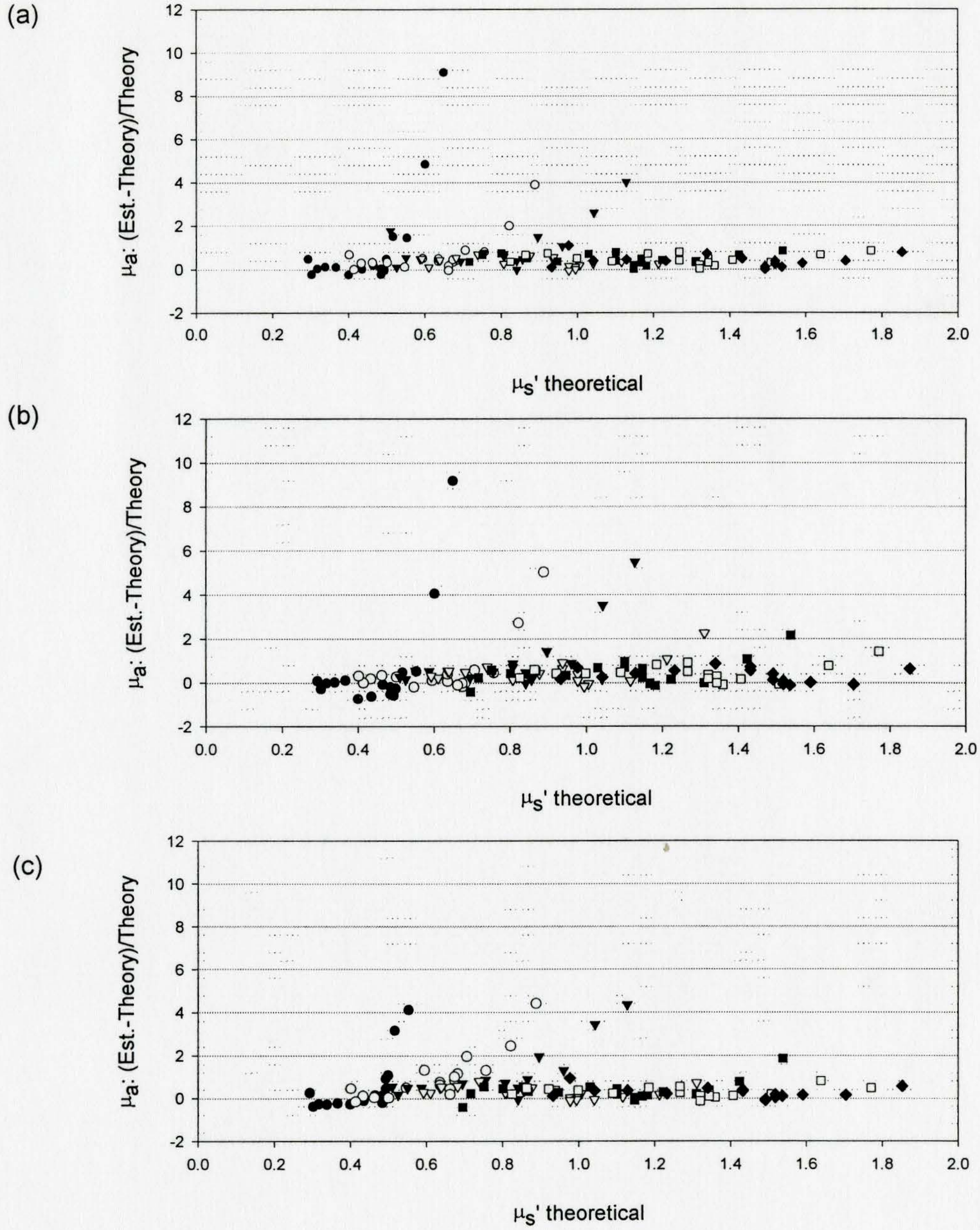

Figure 5.14 Fractional error in estimated μ_a versus theoretical μ_s' for suspensions of 0.653 μm polystyrene spheres Optical properties were estimated using (a) nonlinear least-squares fit to a diffusion model, (b) neural network fit to diffusion model and (c) nonlinear least-squares fit to 'Mono Monte Carlo' simulation. Data for seven particle concentrations (see Table 5.2) are shown in order of increasing concentration as markers ●, ○, ▾, ▿, ■, □, ♦

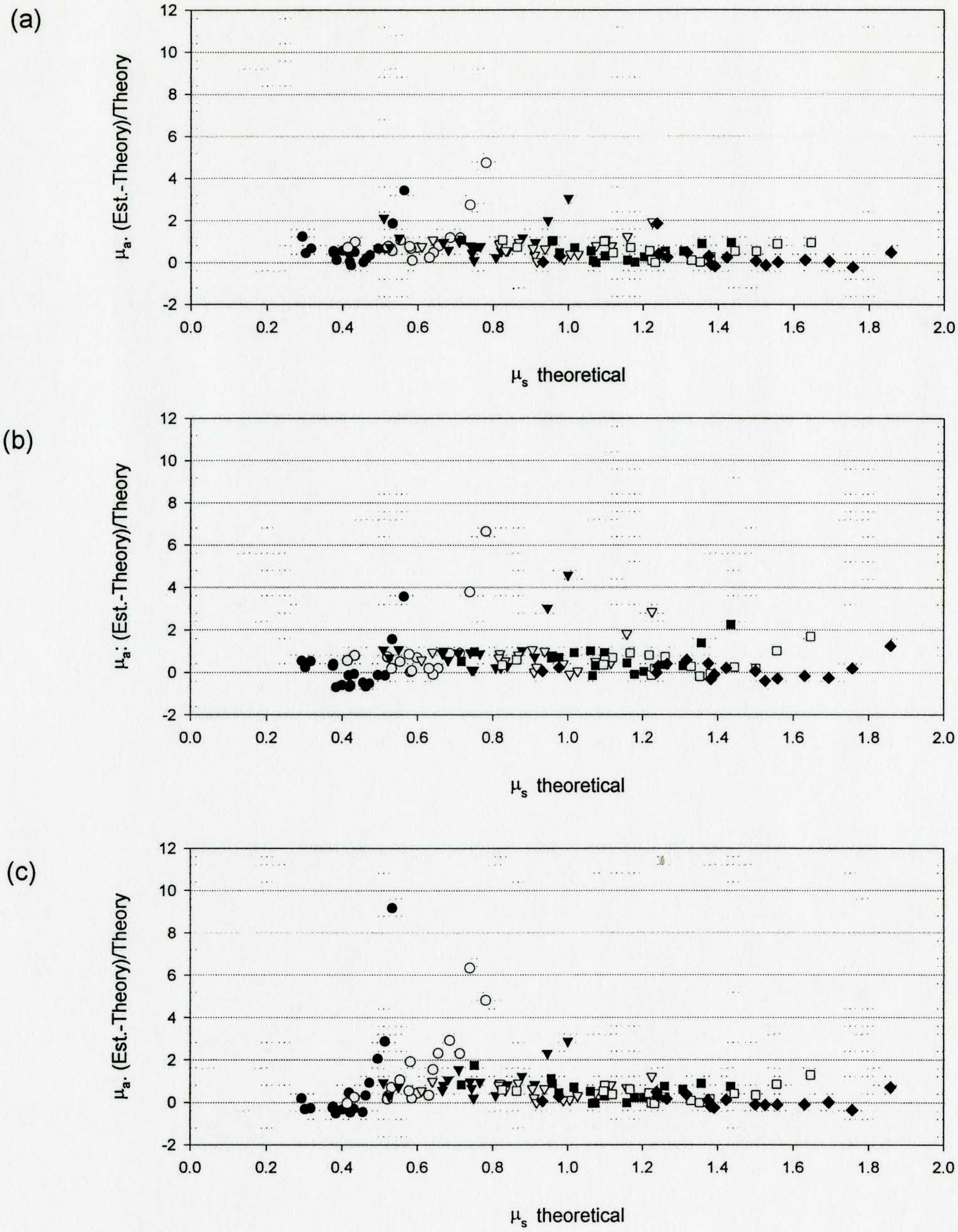

Figure 5.15 Fractional error in estimated μ_a versus theoretical μ_s' for suspensions of 1.53 μm polystyrene spheres Optical properties were estimated using (a) nonlinear least-squares fit to a diffusion model, (b) neural network fit to diffusion model and (c) nonlinear least-squares fit to 'Mono Monte Carlo' simulation. Data for seven particle concentrations (see Table 5.2) are shown in order of increasing concentration as markers. ●, ○, ▾, ▿, ■, □, ♦

all three fitting techniques and for both particle sizes there did not seem to be a correlation between the two parameters.

5.3 Discussion of Polystyrene Sphere Suspension Results

The discrepancies found between the estimated and predicted coefficients of the polystyrene phantoms were much greater than could be explained by uncertainties in the estimated or predicted coefficients. The quality of the reflectance data, and of the fits to the data was investigated as a possible source of error. At wavelengths of 950 nm and 1300 nm, the reflectance data for different suspensions were extracted and plotted as $\ln(\rho^2 R(\rho))$, normalized to 1 mm. 'Theoretical' reflectance was obtained using the optical properties estimated for each sample using each fitting method. For example, reflectance was generated from a diffusion model when the optical properties were estimated using a diffusion model. Similarly, reflectance was obtained from the 'Mono Monte Carlo' simulation for comparison with data fit using the Monte Carlo method. These data were plotted on the same graphs as the measured reflectance, also as $\ln(\rho^2 R(\rho))$, normalized to 1 mm.

Figure 5.16 and 5.17 show the fitting results for 0.653 μm diameter sphere suspensions measured at 950 nm and 1300 nm respectively. Data for all seven particle concentrations are included in each graph. Results are shown for the three fitting techniques. The data at both wavelengths are well-behaved for all particle concentrations, even where the relative intensities vary by several orders of magnitude. It is clear from these graphs that the nonlinear least-squares fit to the diffusion model fits the experimental data at both wavelengths much better than the other two techniques. The neural network demonstrates the worst performance, especially at 1300 nm where the fits bear little

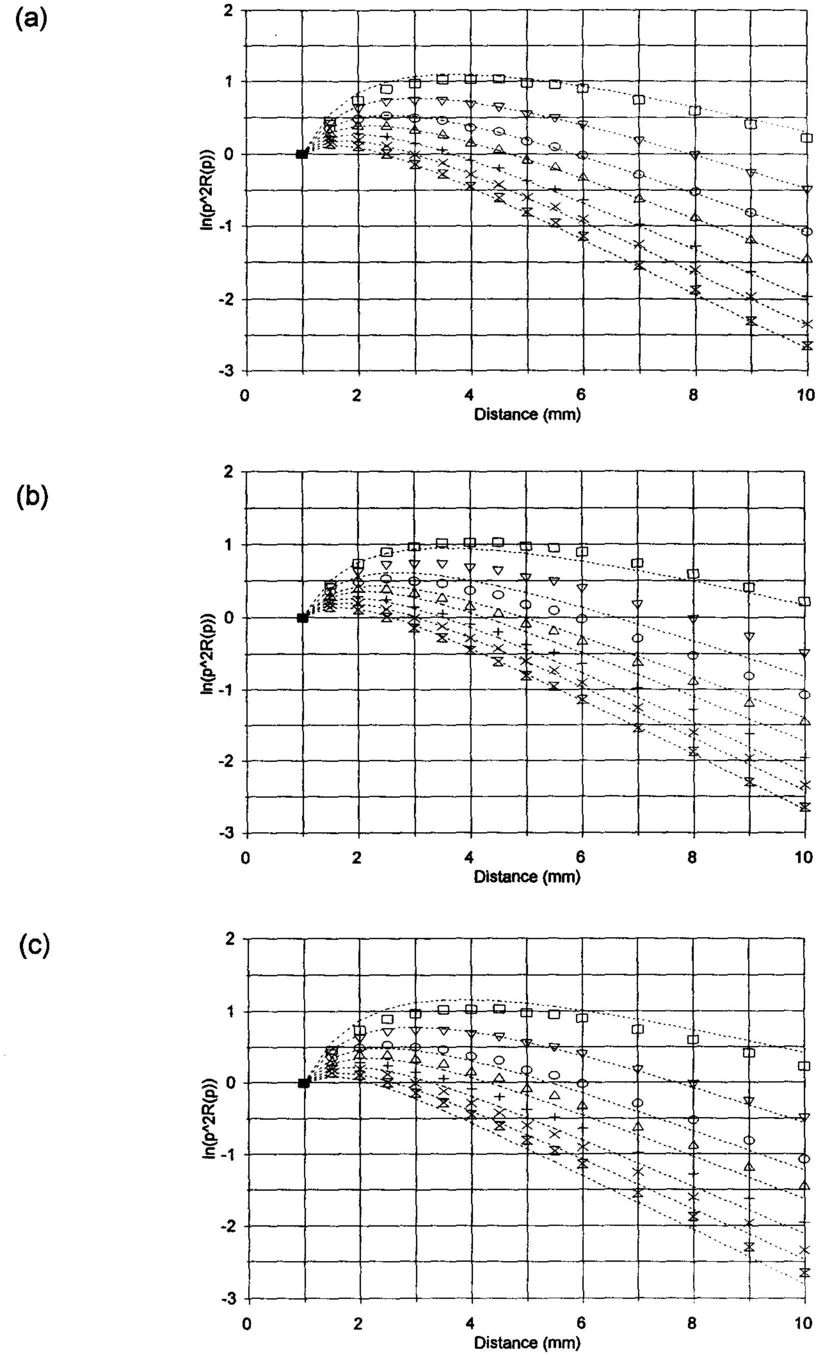

Figure 5.16 Selected fit results for aqueous suspensions of 0.653 μm diameter polystyrene spheres measured at 950 nm. Fits were performed using: (a) nonlinear least-squares fit to the analytical solution to the diffusion model (Equation 14), (b) neural network fit to the diffusion model and (c) nonlinear least-squares fit to the 'Mono Monte Carlo' simulation. Data for seven particle concentrations (see Table 5.2) are shown in order of increasing concentration as markers: □, ▽ ,○, △, +, X, ⋈.

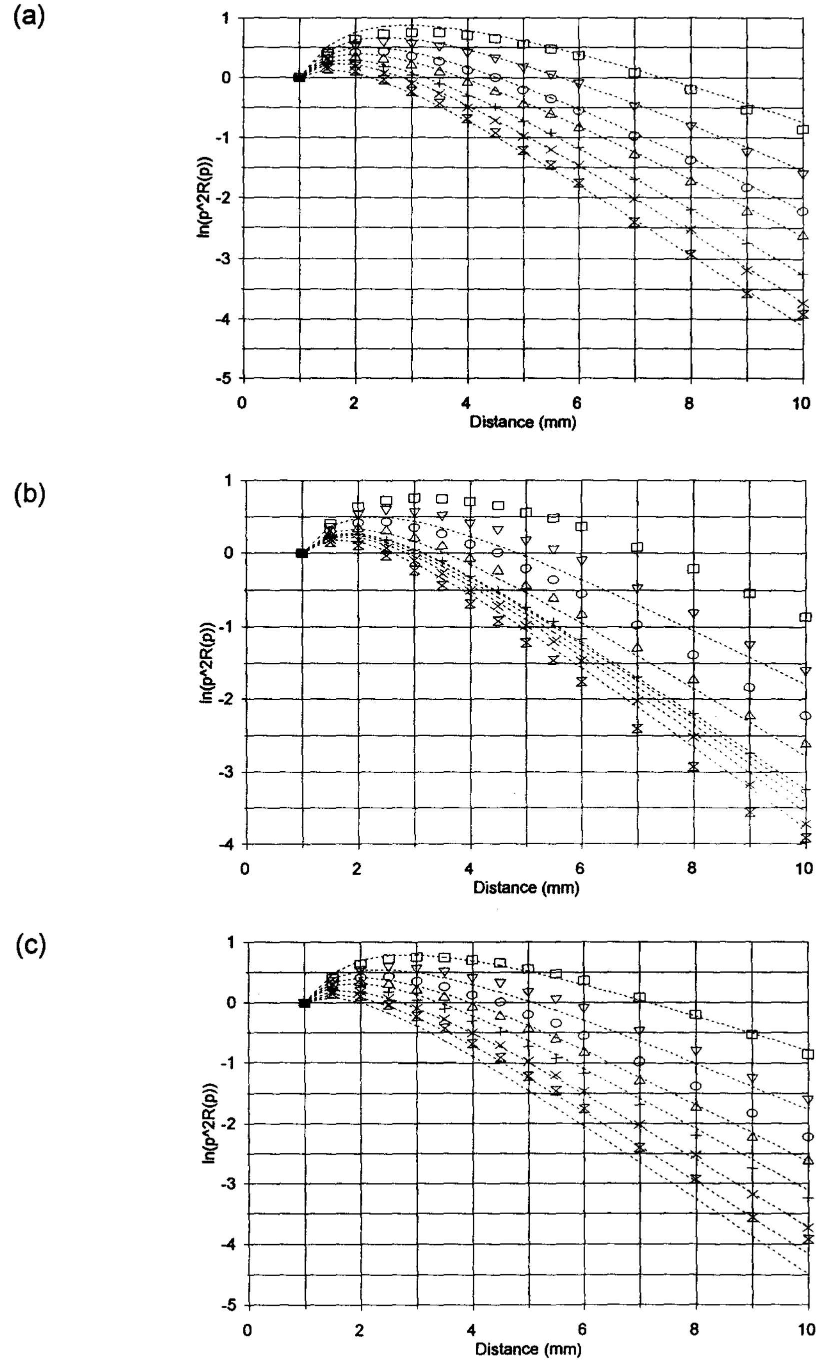

Figure 5.17 Selected fit results for aqueous suspensions of 0.653 μm diameter polystyrene spheres measured at 1300 nm. Fits were performed using: (a) nonlinear least-squares fit to the analytical solution to the diffusion model (Equation 14), (b) neural network fit to the diffusion model and (c) nonlinear least-squares fit to the 'Mono Monte Carlo' simulation. Data for seven particle concentrations (see Table 5.2) are shown in order of increasing concentration as markers: □, ▽ ,○, △, +, X, ⋈.

relationship to the measured data. It should be noted that all three methods yielded incorrect optical properties. The two nonlinear least-squares fitting methods resulted in incorrect coefficients which still fit the data reasonably well, while the neural network method resulted in incorrect coefficients which, in some cases, fit the data extremely poorly.

The nonlinear least-squares fitting techniques produced consistently reasonable fits which resulted in consistently wrong coefficients. The errors in estimated coefficients could not be attributed to expected problems with using a diffusion model, since similar errors occurred when the data were fit using a Monte Carlo simulation. A more basic comparison between measured and predicted results can be done by comparing the measured and predicted relative reflectance. Reflectance data were extracted from the 'Mono Monte Carlo' grid using the predicted optical properties of selected phantoms and wavelengths, and compared to the measured reflectance. These data were plotted as $\ln(\rho^2 R(\rho))$, normalized to 1 mm.

Figure 5.18 plots the theoretical and measured reflectance at 900, 1100 and 1300 nm for four different small sphere phantom concentrations. A similar comparison for the large spheres is shown in Figure 5.19. At both 900 and 1100 nm, the measured reflectance is higher than the expected reflectance. This difference bears some resemblance to the difference in reflectance shown in Figure 2.4 for a matched and mismatched boundary. All of the data analysis performed assumed a perfectly matched boundary between the probe and the surface of the phantom. However, it is possible that the probe used for measurements is not perfectly absorbing, and may introduce a small effective boundary

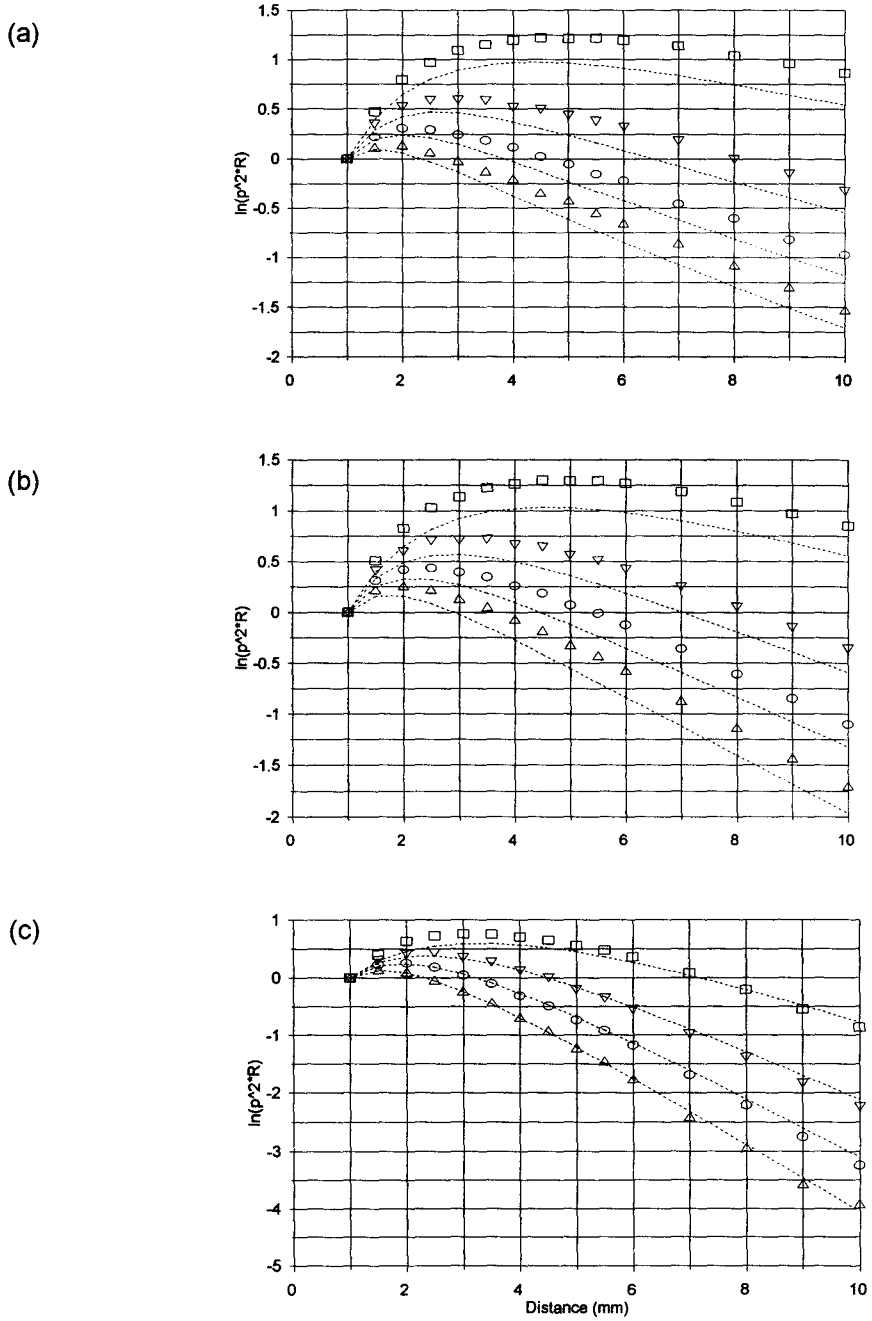

Figure 5.18 Measured and theoretical reflectance at selected wavelengths for 0.653 μm diameter polystyrene sphere suspensions. Data are shown for (a) 900 nm, (b) 1100 nm and (c) 1300 nm. Markers represent measured reflectance for particle concentrations of □ - $1.20\text{x}10^{10}$ mL^{-1}, ▽ - $2.09\text{x}10^{10}$ mL^{-1}, ○ - $2.84\text{x}10^{10}$ mL^{-1}, and △ - $3.70\text{x}10^{10}$ mL^{-1}.

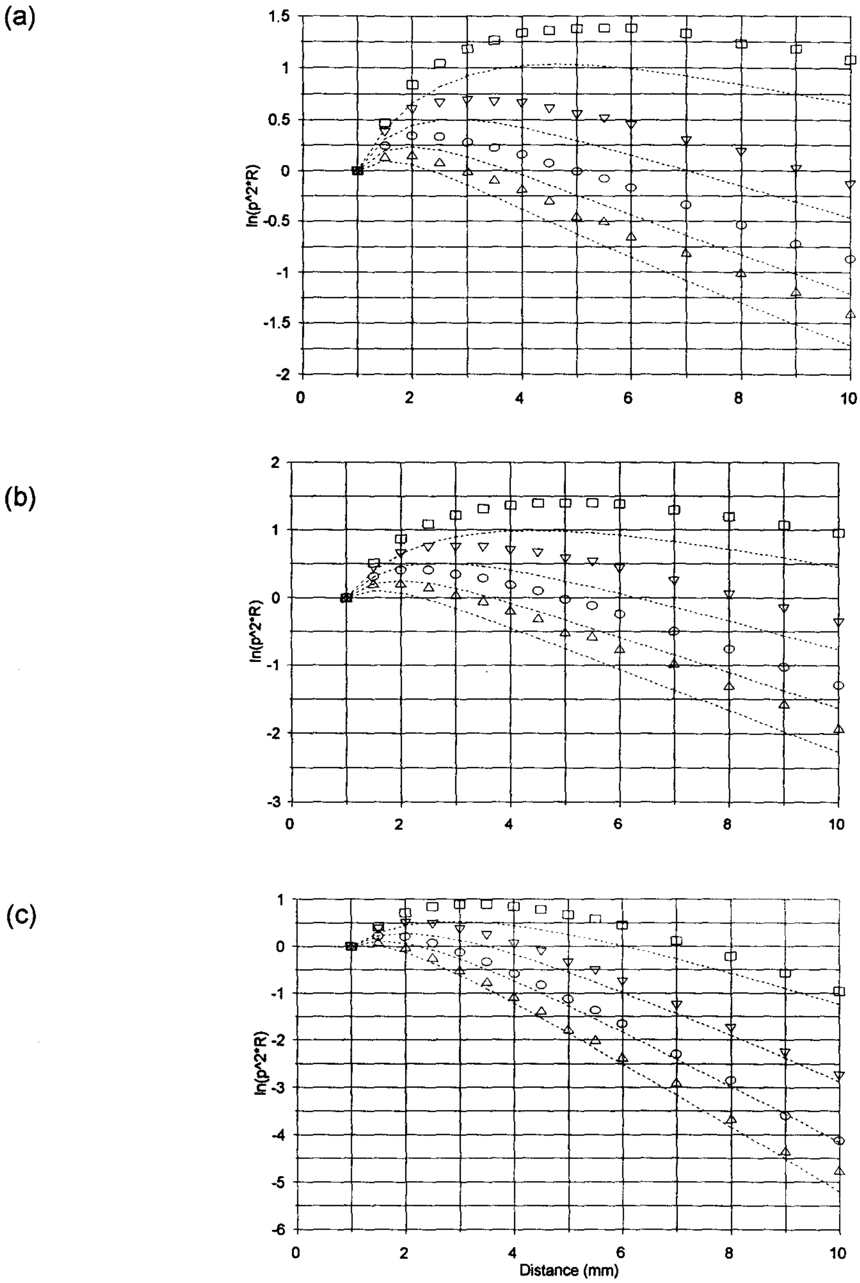

Figure 5.19 Measured and theoretical reflectance at selected wavelengths for 1.53 μm diameter polystyrene sphere suspensions. Data are shown for (a) 900 nm, (b) 1100 nm and (c) 1300 nm. Markers represent measured reflectance for particle concentrations of □ - 1.24x10^9 mL^{-1}, ▽ - 2.21x10^9 mL^{-1}, ○ - 3.17x10^9 mL^{-1}, and △ - 4.10x10^9 mL^{-1}.

mismatch.

The predicted reflectance with and without a small boundary mismatch was compared to the measured reflectance to examine this effect. Figure 5.20 shows the effect of introducing a refractive index mismatch of 1.08 to the predicted reflectance for selected wavelengths and particle concentrations. At 950 and 1100 nm, this change offers a slight improvement to agreement between the predicted and measured reflectance. In some cases, a much larger mismatch would be required to bring the curves into complete agreement. However, introducing a large mismatch would 'over-correct' the discrepancy in other cases. At 1250 nm, the predicted reflectance is already larger than the measured reflectance, and the introduction of a boundary mismatch increases the discrepancy. While it is plausible that a boundary mismatch contributes to the discrepancy between measured and predicted reflectance, there must be other factors which also contribute.

In studying Figures 5.18 and 5.19, one can imagine that by normalizing the $\ln(\rho^2 R(\rho))$ reflectance to a detector distance further from the source, the theoretical and predicted curves would agree much better, especially at the further distances. This suggests that, at least at the lower wavelengths, another source of the discrepancy between the measured and predicted reflectance may be a near detector effect. One such effect which is not accounted for in either the diffusion or Monte Carlo models is the limited collection cone of the detector. Both models assume that any photon leaving the sample at a detector site is collected. In reality, however, the fibre optic detectors have a rather narrow collection angle which is determined by the numerical aperture of the fibre. At distances far from the source, the angular distribution of photons exiting the sample

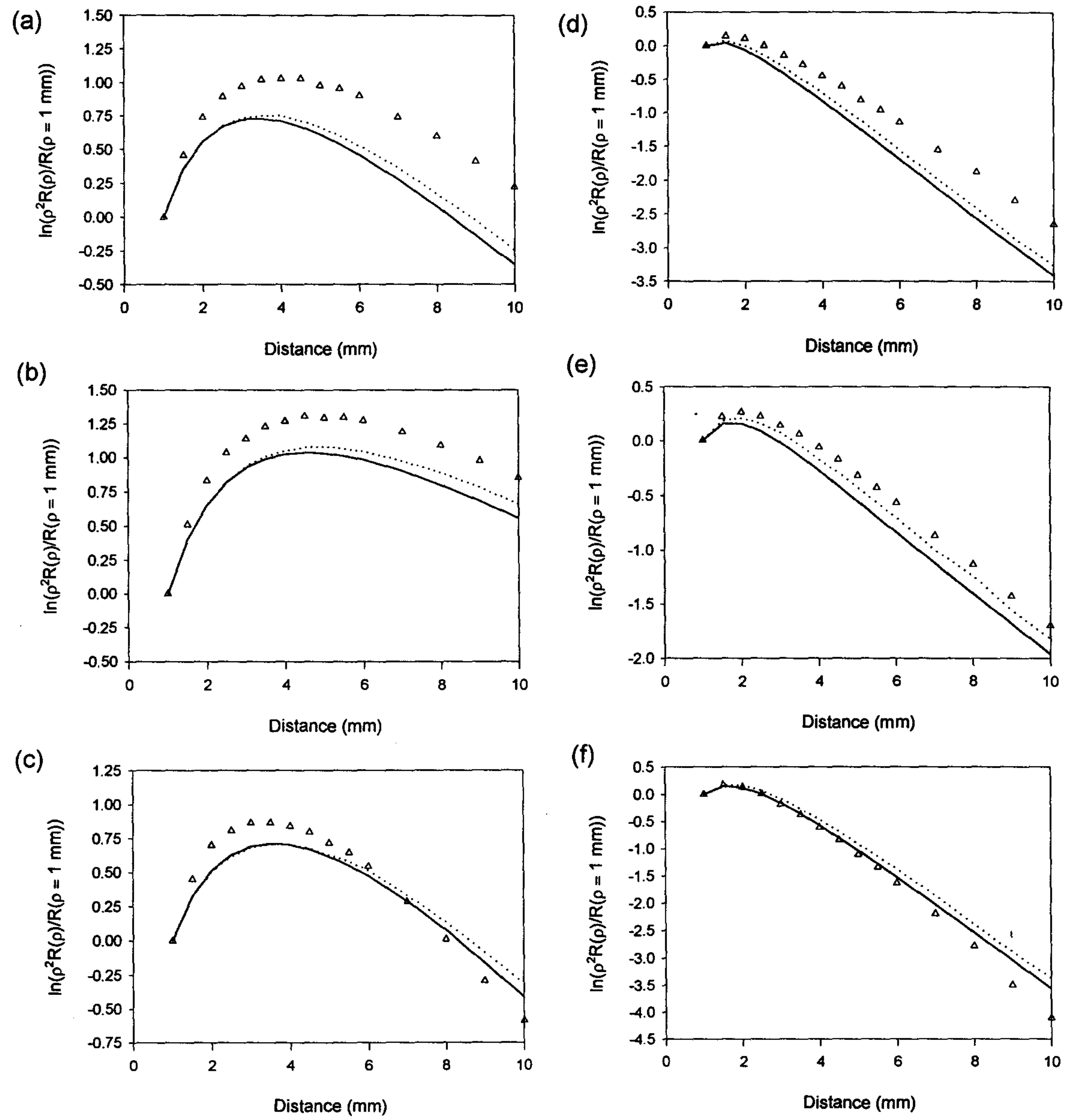

Figure 5.20 Effect of introducing a slight refractive index mismatch at the probe-sample boundary. Predicted and measured reflectance are shown for measurements on aqueous suspensions of 0.653 μm diameter polystyrene spheres. (a), (b), and (c) show the comparison for a particle concentration of 1.20x10^{10} mL^{-1} measured at 950 nm, 1100 nm and 1250 nm respectively. (d), (e), and (f) show the comparison for a particle concentration of 3.70x10^{10} mL^{-1} measured at 950 nm, 1100 nm and 1250 nm respectively. Measured reflectance is plotted as markers. Predicted reflectance is shown for a relative mismatch of 1 (solid line) and 1.08 (dotted line).

becomes uniform; however, at closer distances, before the photon field can be accurately described as being diffuse, the intensity sampled by the acceptance cone of the fibre may not be equivalent to that assumed in the model.

Monte Carlo simulations were performed in which the numerical aperture of the detectors was considered. Only photons leaving the sample at an angle within the cone defined by the fibre numerical aperture (incident on water) were scored. The reflectance obtained from these simulations was compared to the reflectance obtained using the standard method. Results for these simulations are shown for two sets of optical properties in Figure 5.21. The data are plotted as $\ln(\rho^2 R(\rho))$ normalized to 1 mm. These graphs show that inclusion of the numerical aperture factor introduces a positive shift in the reflectance curve when normalization is performed with respect to 1mm. The introduction of such a shift would reduce the discrepancy between measured and predicted reflectance curves shown in Figures 5.18 and 5.19, at least at the lower wavelengths.

Two possible factors which may contribute to the discrepancies found between the measured and predicted reflectance have been discussed: incorrectly assuming a perfectly matched boundary between the probe and sample, and not accounting for the collection geometry introduced by fibre optic detectors. Neither of these factors could reasonably be assumed to account fully for the observed discrepancies, although including a combination of both of these factors in the model would result in still better agreement between the measured and predicted reflectance in many cases. A problem associated with applying both of these factors is that they do not result in improvements at all the wavelengths sampled. At wavelengths with high absorption coefficients, application of these factors increases the discrepancy between measured and predicted reflectance. There must be an additional factor or factors contributing to these discrepancies which is not accounted for in the models. It is possible that these factors exhibit spectral dependence.

Aqueous suspensions of monodisperse polystyrene spheres are commonly used as optical standards because their optical properties are easily determined using Mie theory. Mourant *et al* [1997] performed measurements on polystyrene sphere suspensions using a method similar to the technique applied in our studies. In their case, a model of an infinite medium was used, and a diffusion approximation was applied to the measured reflectance to estimate the optical properties. They found good agreement between spectral dependence of the measured and predicted reduced scattering coefficients. However, they noted that the magnitude of the estimated reduced scattering coefficients differed from the theoretical values by about a factor of two. They provided no explanation for this observed discrepancy. Nichols *et al* [1997] used a method nearly identical to our technique to measure the optical properties of polystyrene sphere suspensions. They applied the diffusion model solution given by Equation 14 to their measured reflectance to estimate the optical properties. The reduced scattering coefficients that they measured were within less than 10% of their predicted coefficients for suspensions with μ_s' greater than 0.55 mm^{-1}, and were systematically over-estimated. It is difficult to see how we can apply the identical technique, model, instrument and sampling probe and yet obtain significantly worse results.

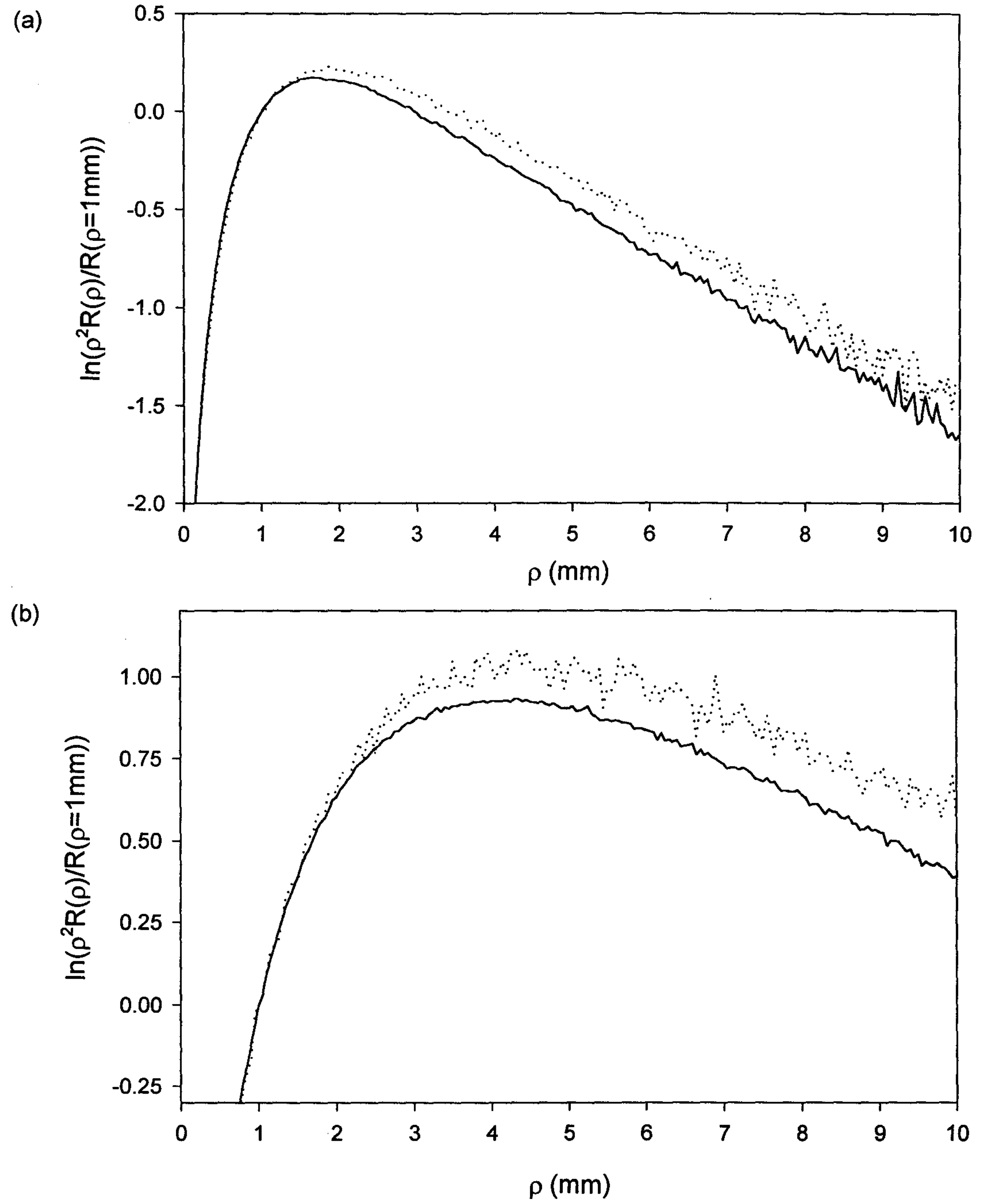

Figure 5.21 Effect of including a numerical aperture acceptance angle criterion in Monte Carlo simulations. Reflectance obtained using the standard method (solid line) is compared to the reflectance obtained when the numerical aperture criterion is applied (dotted line). Reflectance is shown for (a) $\mu_s' = 1.3$ mm^{-1}, $\mu_a = 0.01$ mm^{-1} and (b) $\mu_s' = 0.5$ mm^{-1}, $\mu_a = 0.01$ mm^{-1}.

Chapter 6 Demonstration of Instrument Application *in Vivo*

A series of experiments was performed to demonstrate the *in vivo* capabilities of the instrument and to introduce some potential applications. Although the technique was found to be lacking in accuracy for absolute determination of optical properties, it is useful for applications in which the primary requirement is the detection of relative changes of optical properties over time or with wavelength. The experimental results have been divided into three sections. The first section will present *in vivo* measurements of human skin on several volunteers. Section 6.2 will present results of a study comparing optical properties of tissue containing oxygenated or deoxygenated haemoglobin as measured on a human hand. The last section will explore the temperature dependence of optical properties of human skin.

6.1 Optical Properties of Human Skin

As described in Chapter 1, the optical properties of skin in the region under study (900 - 1400 nm) are expected to be characterized by an absorption spectrum similar to that of water, and a scattering coefficient which decreases with increasing wavelength. The magnitudes of the absorption and scattering coefficients are more difficult to predict because of variability of skin thickness, subdermal tissue, and water content between individuals and different body sites. Spatially resolved diffuse reflectance spectra were obtained on several human volunteers to investigate these predictions. For each measurement, the probe was placed on either the abdomen or lower back of the volunteer. The probe was fixed to the skin using a thin, transparent double-sided medical adhesive (Adhesives Research). The volunteer lay on his or her back or abdomen for the duration of the scan, and kept as still as possible to prevent motion artifacts. Lights in the room were dimmed during the measurement.

A wavelength scan was obtained with measurements taken at 10 nm increments. The measured signal is strongly dependent on the wavelength due to both the instrument response and the optical property spectral dependence. For this reason, the exposure time for each wavelength was optimized for maximum signal without detector saturation. The exposure times ranged from about 0.5 seconds to 5 seconds. For extremely high attenuations of tissue beyond 1360 nm, exposure times were not fully optimized to prevent the scan from becoming too long. Each scan took approximately 20-30 minutes which included a background scan.

8 scans were obtained on a total of 6 volunteers, with 2 scans performed on the lower back and the remainder on the abdomen. All volunteers were Caucasian between the age of 20 and 40. Both male and female volunteers were measured. The probe was calibrated using the integrating sphere method described in Chapter 4. Optical properties were estimated using the three methods described in Chapter 3. Optical property spectra obtained using the nonlinear least squares fit to the diffusion model are plotted in Figures 6.1a (reduced scattering coefficient) and 6.1b (absorption coefficient). In Figure 6.1b the

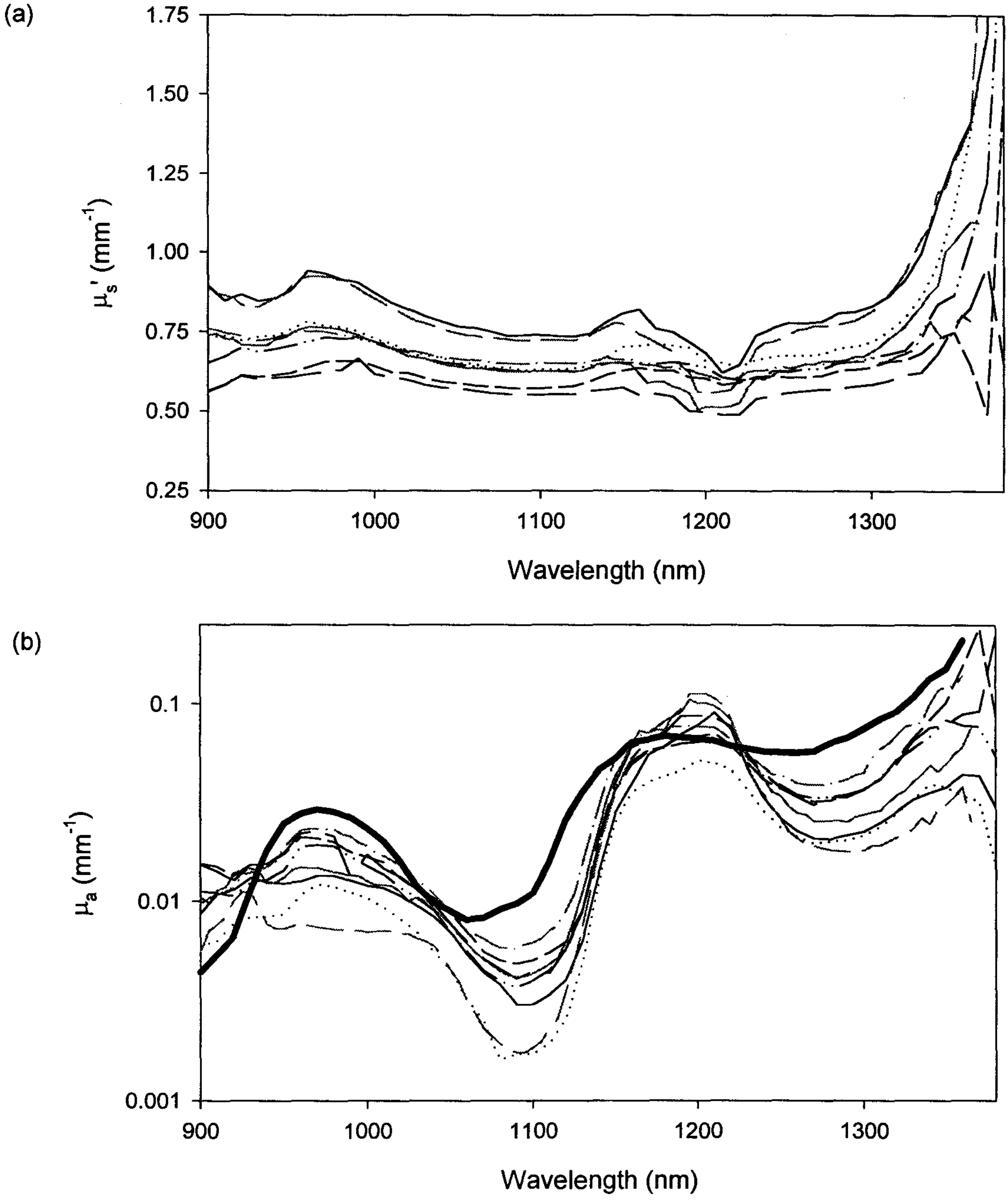

Figure 6.1 *In vivo* optical property spectra of skin obtained from 6 Caucasian volunteers. Two volunteers were measured on both the abdomen and lower back. Optical properties were estimated using a nonlinear least-squares fit to an analytical solution to the diffusion approximation (Equation 14). The absorption spectrum of water at a concentration of 65% is shown in (b) as a thick solid line.

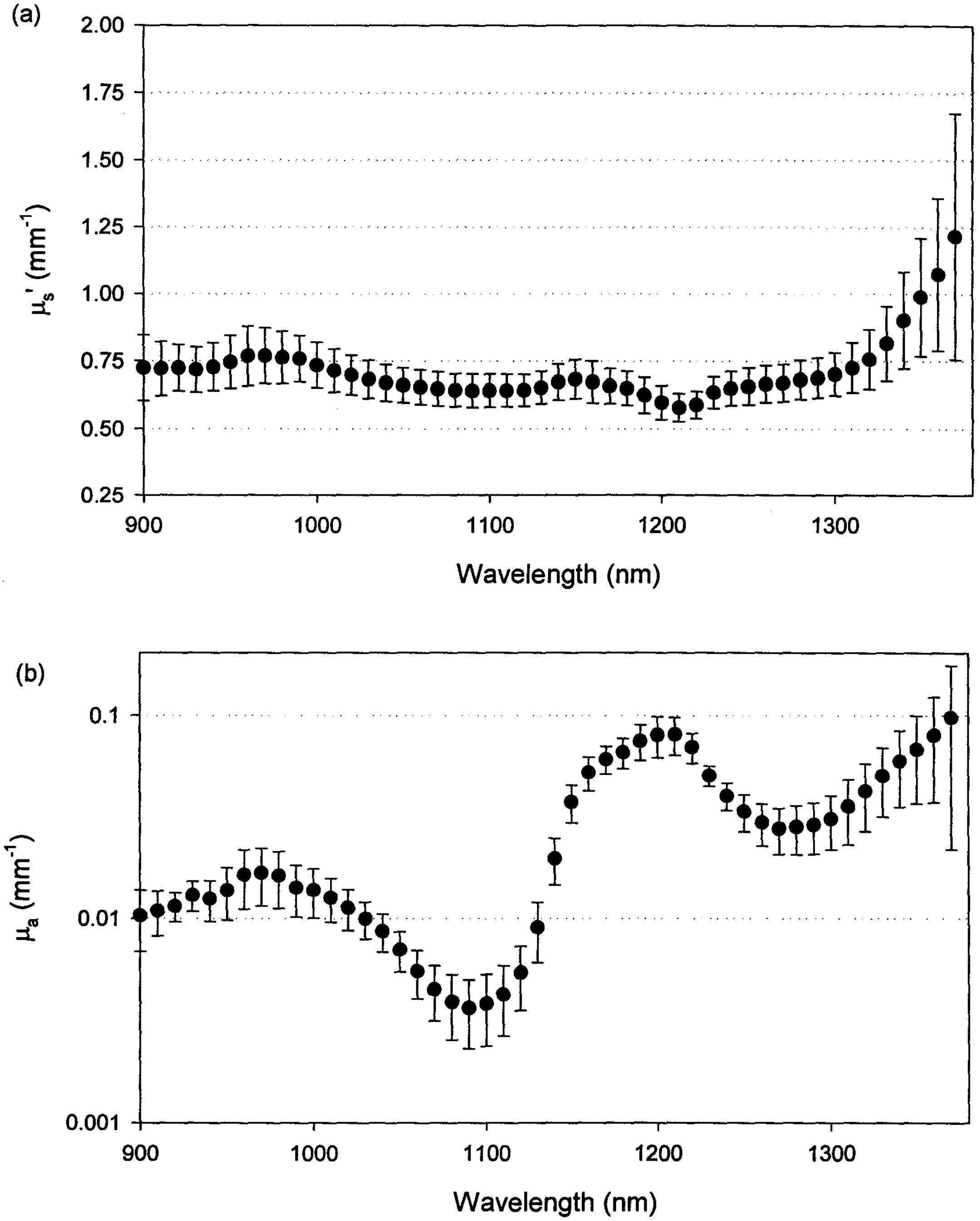

Figure 6.2 *In vivo* optical properties of skin. The mean of 8 samples is shown. Error bars represent the standard deviation of the optical properties.

spectrum of water, assuming a concentration of 65%, is plotted for reference. The two measurements obtained on the lower back resulted in spectra which fell within the range of both absorption and scattering spectra obtained on the abdomen, and are not distinguished in the plots. The mean of the coefficients at each wavelength was obtained and is plotted in Figures 6.2a (reduced scattering coefficient) and 6.2b (absorption coefficient). The error bars represent the standard deviation of the 8 samples.

These results indicate a large inter-volunteer variation in optical properties. The largest range in values occurs at the longest wavelengths, where there is less confidence in the method of optical property extraction, particularly when the diffusion approximation is invoked. The features of the absorption spectra are fairly consistent and agree with the features of the water spectrum, although there is a wide range in relative magnitude of the spectral peaks and valleys. The spectra for the reduced scattering coefficient exhibit fairly consistent features for all volunteers. However, the spectral features observed are unexpected. In the wavelength region extending from about 950 nm to 1150 nm, μ_s' decreases with wavelength, as predicted. From 900 nm to 950 nm, some spectra display an increasing μ_s'. From 1150 nm to 1230 nm all spectra have a rise in μ_s', followed by a dip. Beyond 1230 nm, all spectra show an increasing μ_s', with a dramatic increase occurring beyond 1300 nm.

The differences in optical properties estimated using different methods also fell within the range of the inter-volunteer variation. The optical property spectra obtained on one of the volunteers are displayed in Figure 6.3a (μ_s') and 6.3b (μ_a). In this case the optical properties were estimated using all three fitting techniques. For both estimated coefficients, the three techniques resulted in spectra of differing magnitudes, but basically

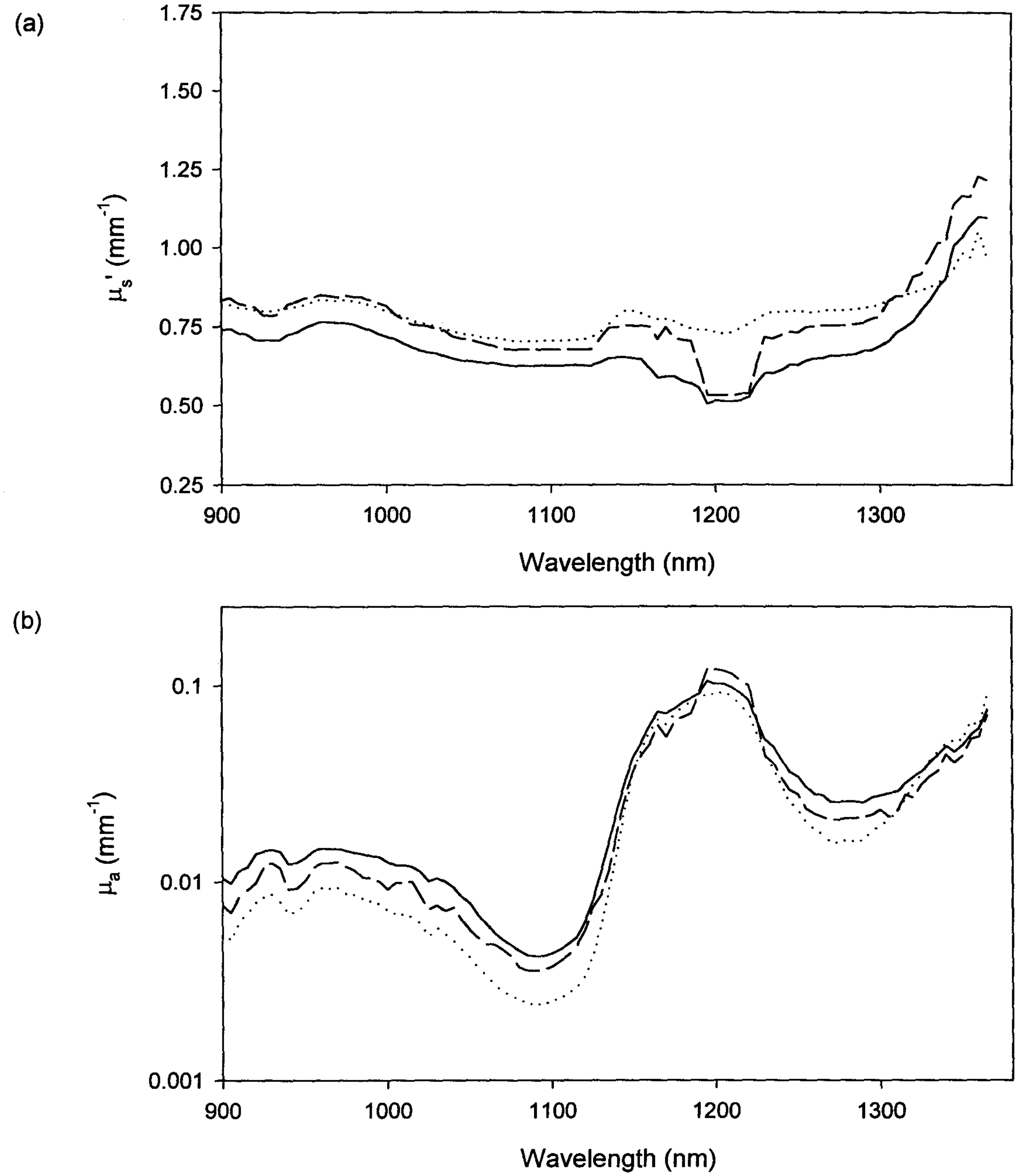

Figure 6.3 *In vivo* optical properties of skin estimated using three different fitting techniques. Solid line - nonlinear least-squares fit to diffusion model (Equation 14); dotted line - neural network fit to diffusion model (Equation 14); dashed line - nonlinear least-squares fit to 'Mono Monte Carlo' simulation.

the same spectral features.

It is interesting to compare how well these different methods of fitting are able to fit the reflectance data. Figure 6.4 plots the reflectance as $\ln(\rho^2 R(\rho))$, normalized to $\rho = 1$ mm at selected wavelengths using data from the same scan as shown in Figure 6.3. The markers represent measured data, while the lines are the corresponding fits. The fits for the nonlinear least-squares fit to diffusion, neural network fit to diffusion, and nonlinear least-squares fit to a Monte Carlo simulation are given in Figure 6.4a, b, and c respectively. Figure 6.4d shows all three fits plotted together at two selected wavelengths. With the exception of the neural network at certain wavelengths, the estimated coefficients result in curves which fit the data points reasonably well. Figure 6.4d demonstrates that three different sets of optical properties (as shown in Figure 6.3) can result in very similar fitting results.

Some of these results can be compared to *ex vivo* optical properties determined by other researchers at selected wavelengths. Chan *et al* [1997] performed transmission and reflectance measurements at 1065 nm on thin samples of skin consisting of epidermis and dermis. On Caucasian volunteers they measured μ_a ranging from 0.02-0.45 mm^{-1}, with a mean of 0.14 mm^{-1} from 9 samples. They found that μ_s' ranged from 0.69-1.96 mm^{-1} with a mean value of 1.24 mm^{-1}. Simpson *et al* [1997] also performed transmission and reflectance measurements on separate thin samples of Caucasian dermis and subdermis at 1000 nm. The subdermis was composed mainly of fat. They found μ_a to be about $0.036 \pm 0.01 mm^{-1}$ in the dermis, and $0.012 \pm 0.005 mm^{-1}$ in the subdermis. They measured a μ_s' of $1.5 \pm 0.2 mm^{-1}$ in the dermis and 1.1 ± 0.3 mm^{-1} in the subdermis. Both of these *ex*

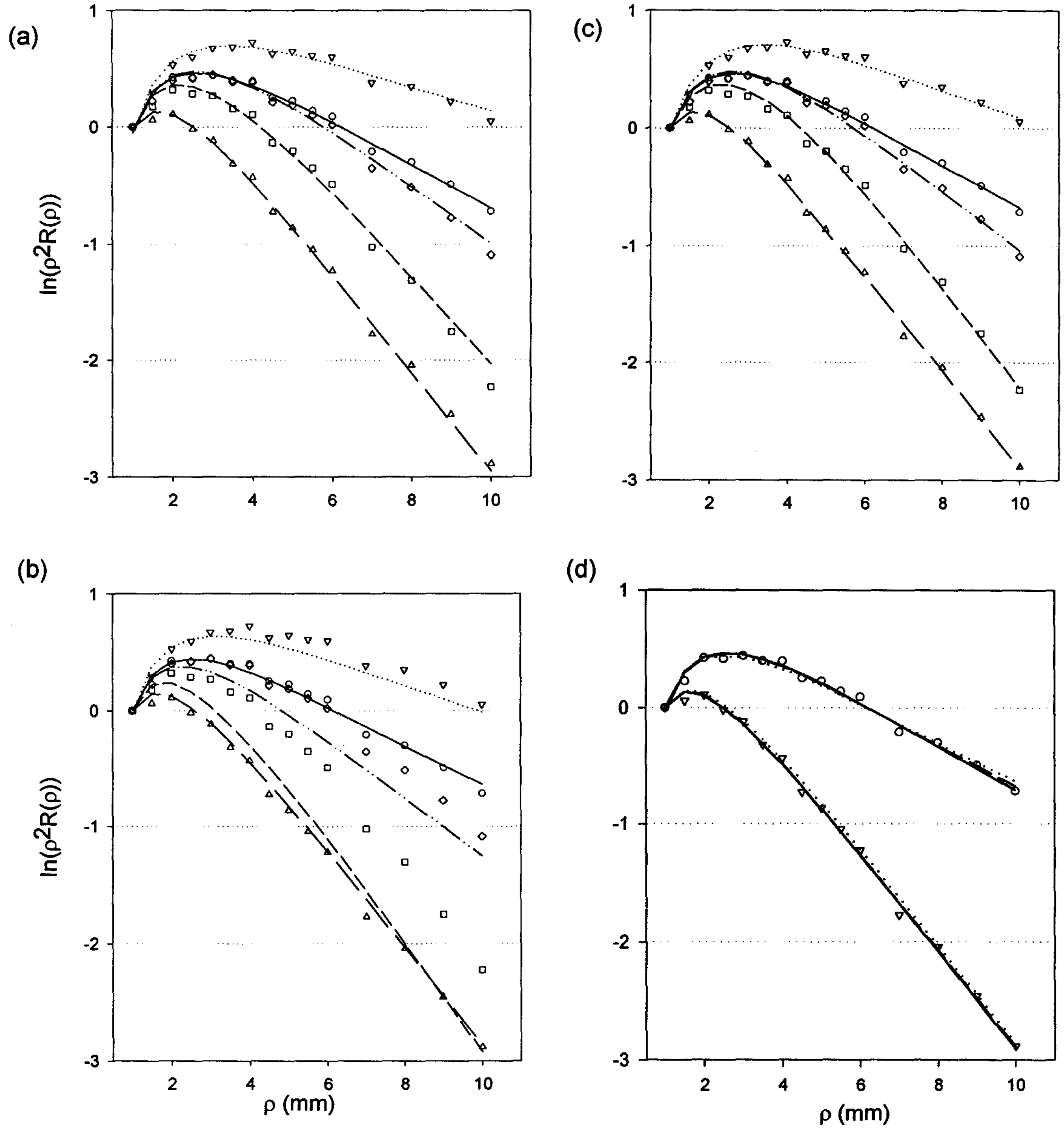

Figure 6.4 Selected fitting results to reflectance sampled on skin, *in vivo*. (a) nonlinear least-squares fit to diffusion model (Equation 14), (b) neural network fit to diffusion model (Equation 14), (c) nonlinear least-squares fit to 'Mono Monte Carlo' simulation, (d) comparison of three fits. Measured reflectance data are shown as symbols and fits as lines for selected wavelengths in (a), (b), and (c) as: 950 nm - ○, solid line, 1100 nm - ▿, dotted line, 1200 nm - □, dashed line, 1250 nm - ◇, dash-dot line, and 1350 nm - ▵, long dashed line. In (d), measured reflectance is plotted as symbols for 950 nm (○) and 1350 nm (▿). Fits in (d) are plotted as: solid line - nonlinear fit to diffusion model; dotted line - neural network fit to diffusion model; dashed line - nonlinear fit to 'Mono Monte Carlo' simulation.

vivo measurements resulted in higher optical coefficients than those estimated *in vivo* in this study. At 1000 nm, μ_a and μ_s' were found to be $0.014 \pm 004\text{mm}^{-1}$ and $0.73 \pm 0.9\text{mm}^{-1}$ respectively, and at 1060 nm μ_a and μ_s' were found to be $0.0055 \pm 0.001\text{mm}^{-1}$ and $0.65 \pm 0.07\text{mm}^{-1}$. The trend towards lower optical coefficients in the *in vivo* measurement is consistent with the findings of Graaff *et al* [1993].

It is also of interest for this study to understand how the optical properties of skin, measured *in vivo*, may change on the same individual over an extended period of time. For any sort of monitoring application, the normal variations of tissue optical properties must be separated from the changes induced by the physiological factor of interest. In order to estimate what these baseline changes might be, several optical property stability measurements were performed on volunteers. The protocol for these measurements was similar to that described above for the wavelength scans. All measurements were performed on the abdomen. Volunteers lay as still as possible during the measurement, and were not permitted to consume food or drink 1 hour before or during the measurement. Reflectance measurements were obtained at 3 wavelengths for a duration of 2 hours or more at intervals of about 20 seconds.

Results from a sample stability measurement are shown in Figure 6.5. Figure 6.5a shows the relative transport scattering coefficient over the measurement period for the three wavelengths, and 6.5b shows the relative absorption coefficient. Optical properties were estimated using a nonlinear least squares fit to the diffusion model. The relative coefficient was obtained by taking the coefficient at each time and dividing by the mean of that coefficient over the entire measurement period for each respective wavelength. A

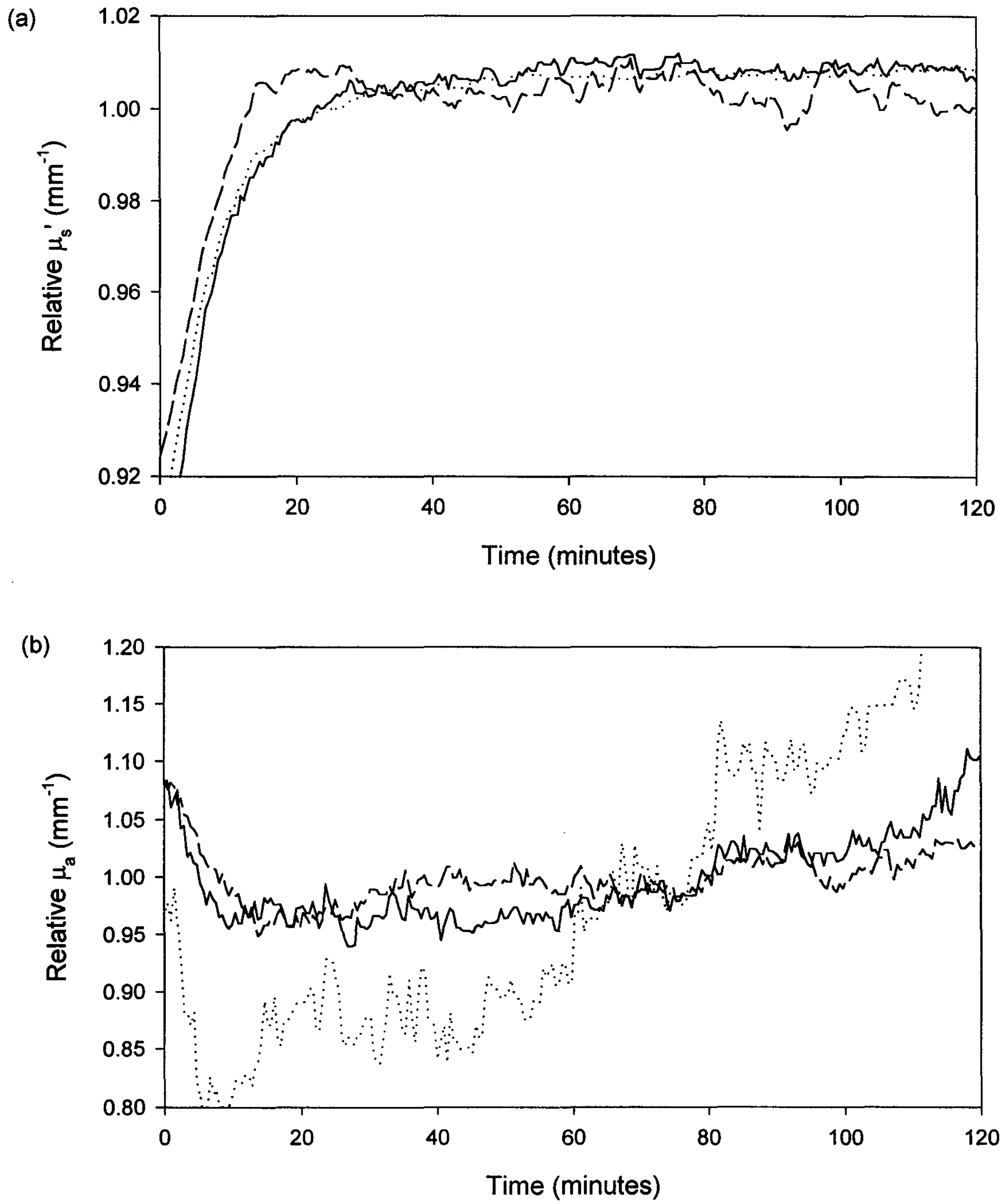

Figure 6.5 Typical optical property stability measurement. Optical properties are plotted relative to the mean of the measurement period. Data were sampled at 3 wavelengths and are plotted as: solid line - 960 nm; dotted line - 1060 nm; dashed line - 1250 nm.

common trend observed in most stability measurements was an increase or decrease in μ_s' during the initial 30 minutes of measurement. In some cases μ_s' changed by more than 10% during this initial period, although usually the change was on the order of 5%. It is believed that this change is a result of the skin-adhesive-probe interface coming into an equilibrium state. During this initial period, local swelling of the skin beneath the probe may occur, as well as sweating. In addition, the adhesive may develop air bubbles, resulting in perturbations from what is assumed to be a perfectly matched boundary. Another common characteristic of these scans was a steady increase of in μ_a throughout the scan. The relative change in μ_a was often very large, changing by as much as 20% over a 2-hour period in some cases. The largest rate of increase was usually observed during the initial 30 minutes of measurement, which may be related to the contact issues previously discussed. The reasons for the apparent continuous increase are not known

Five stability measurements were performed on volunteers according to the protocol described above. For each scan, the relative standard deviation of the optical properties over the measurement was determined, excluding the first 30 minutes of sampling. The results are summarized in Table 6.2. The stability of the reduced scattering coefficient was, in general, better than that of the absorption coefficient by a factor on the order of 10. The absorption coefficient was usually more stable at 1250 nm than the other two wavelengths, by about a factor of 2. No consistent spectral dependence was observed in the reduced scattering coefficient.

Table 6.1 Summary of stability measurements. The relative standard deviation was evaluated using all but the first 30 minutes of the sample period. Remainder of sampling time is about 90 minutes.

	Relative σ, μ_s'			**Relative σ, μ_a**		
	960 nm	**1060 nm**	**1250 nm**	**960 nm**	**1060 nm**	**1250 nm**
1	0.0025	0.0027	0.0040	0.0402	0.0438	0.0286
2	0.0061	0.0054	0.0034	0.0372	0.0515	0.0161
3	0.0029	0.0017	0.0043	0.0401	0.0481	0.0107
4	0.0063	0.0066	0.0123	0.0771	0.0829	0.0784
5	0.0033	0.0017	0.0045	0.0605	0.0765	0.0208
mean	0.0042	0.0036	0.0057	0.0510	0.0605	0.0309
min	0.0025	0.0017	0.0034	0.0372	0.0438	0.0107
max	0.0063	0.0066	0.0123	0.0771	0.0829	0.0784

Optical techniques which are used to detect concentration changes of tissue constituents must be able to attain specificity to the analyte of interest. Optical spectroscopy has been applied to blood oxygenation monitoring [Cope *et al* 1988] in the NIR because good specificity is possible due to the significant contribution of haemoglobin to tissue absorption, and to the fact that oxygenated and reduced haemoglobin have different absorption spectra at wavelengths lower than about 1250 nm. Figure 6.6 plots

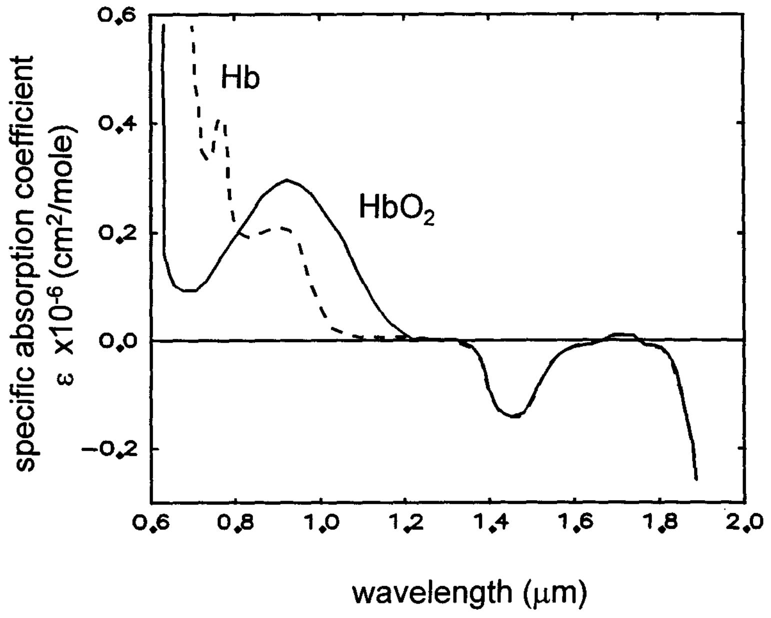

Figure 6.6 Absorption spectra for oxygenated and reduced haemoglobin. From Barlow and Polanyi [1962].

the absorption spectra for oxygenated and reduced haemoglobin. Beyond about 1250 nm, the oxygenated and reduced haemoglobin spectra become isosbestic. Noninvasive optical monitoring of other analytes in tissue may be confounded by blood oxygenation changes in the lower wavelength region, but not in the isosbestic region. In addition to this, the optical properties of tissue at wavelengths at which absorption becomes dominated by water rather than haemoglobin should be less sensitive to changes in blood volume.

To investigate these hypotheses, reflectance measurements were performed on the palm of the hand of volunteers. Blood volume increases via venous occlusion were induced by applying a pressure of 85 - 100 mmHg to a blood pressure cuff worn on the arm. Blood oxygenation decreases via arterial occlusion were induced by applying a pressure of ~250 mmHg. The measurement series consisted of about 10-15 min of baseline acquisition with no applied pressure, ~5 min of arterial occlusion, 10-15 min with no applied pressure, ~5 min venous occlusion, and finished with about 10-15 min with no externally applied pressure. In some cases a second venous occlusion step was performed in place of the arterial occlusion step. Data were acquired at 1060 nm or 1040 nm, and 1250 nm. Optical properties were estimated using the nonlinear least-squares fit to the diffusion model.

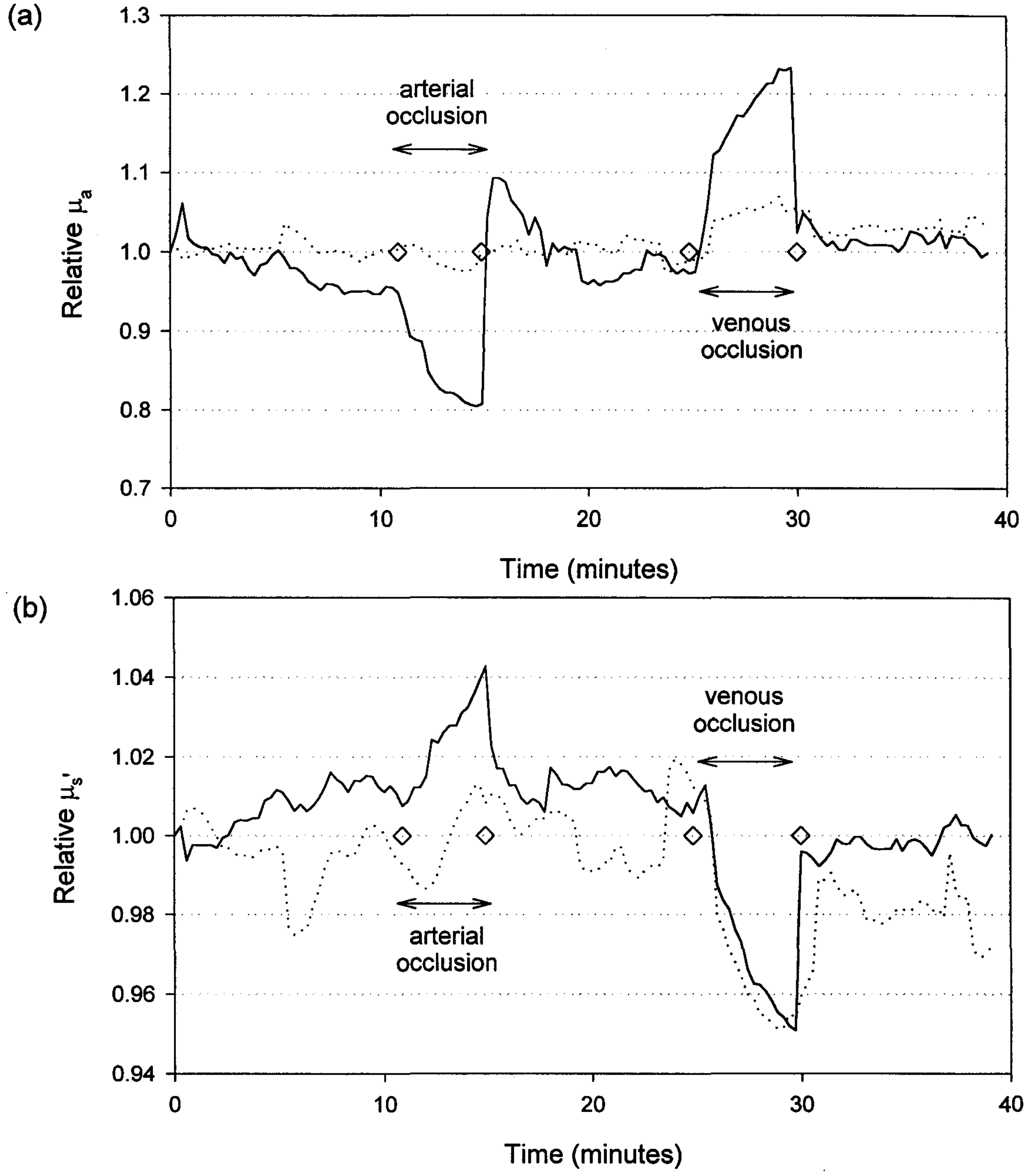

Figure 6.7 Optical properties measured during a typical arterial and venous occlusion experiment. Solid line - 1040 nm. Dotted line - 1250 nm. Markers denote the start and end of periods during which cuff pressure was applied.

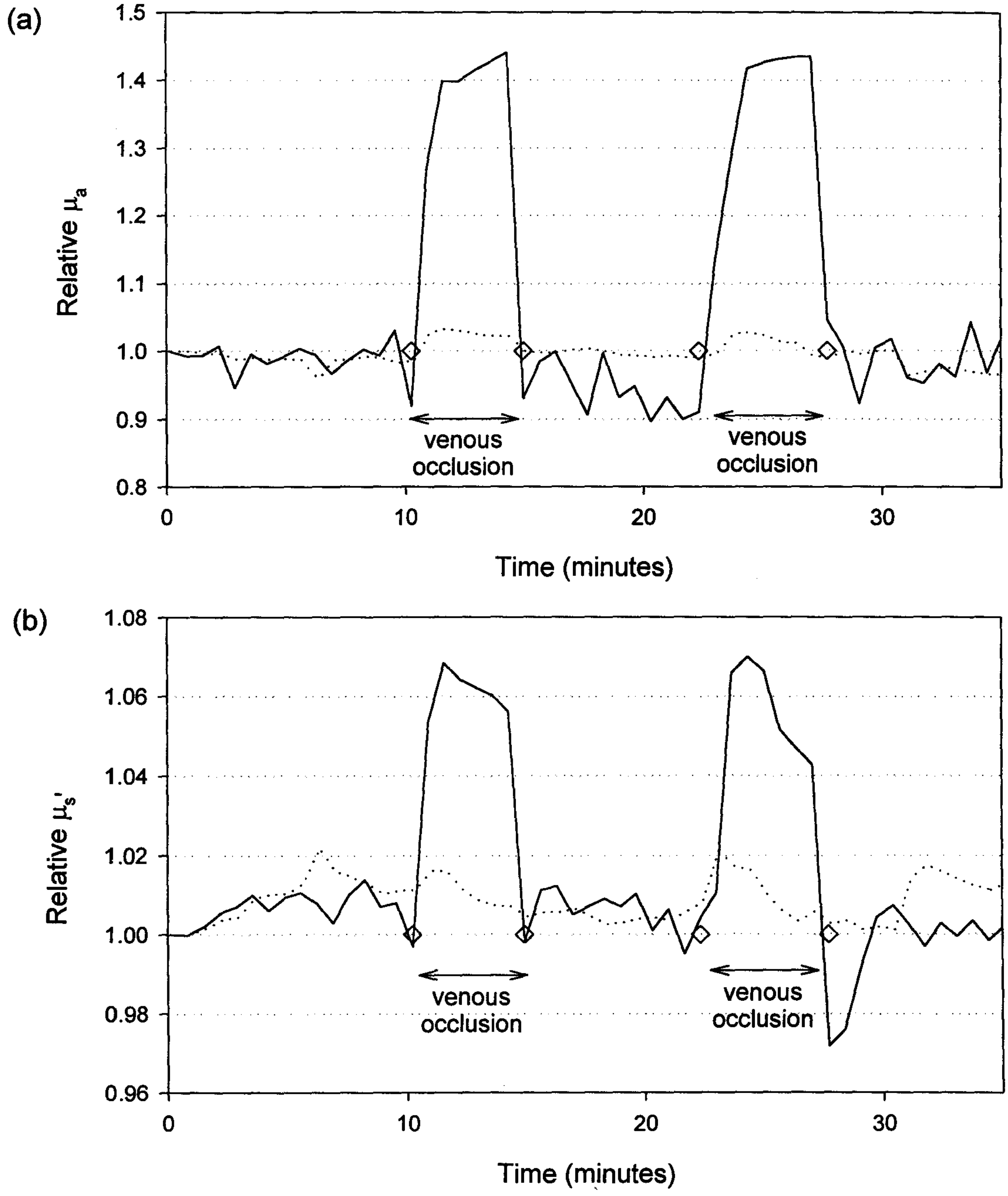

Figure 6.8 Optical properties measured during a typical venous occlusion experiment. Solid line - 1040 nm. Dotted line - 1250 nm. Markers denote the start and end of periods during which cuff pressure was applied.

Figure 6.7a shows the estimated absorption coefficient versus time for a typical experiment in which venous and arterial occlusion were induced, and 6.8a is an example of an experiment in which two venous occlusions were performed in sequence. During the arterial occlusion step in Figure 6.7a, the absorption coefficient at 1040 nm decreased by about 15 %, and showed little change at 1250 nm. After release of pressure μ_a at 1040 nm increases very quickly, rising initially to 10% above its original value, and then returning to close to the initial magnitude. This 'overshoot' in the absorption coefficient is consistent with the expected phenomenon of post-occlusion hyperaemia [Andersen 1994]. At 1250 nm, the absorption coefficient remains stable after release of pressure. The venous occlusion steps shown in Figure 6.7a and 6.8a demonstrate the increase of μ_a due to the blood volume increase. The magnitude of the increase is larger for the lower wavelength measured, due to the larger contribution of blood constituents to the tissue absorption coefficient. The corresponding scattering coefficients for these occlusion scans are given in Figure 6.7b and 6.8b.

Four scans were obtained in which both an arterial and venous occlusion step were performed, and four scans were obtained in which two venous occlusion steps were performed. Table 6.2 summarizes the results obtained for these scans at 1040 or 1060 nm and 1250 nm. For each volunteer, the optical properties prior to clamping were estimated from the scan result. The change in both μ_a and μ_s' was also estimated for each step, and is tabulated in Table 6.2 as the change relative to the magnitude just prior to the application of pressure. In some cases it was difficult to estimate the change accurately, because the optical properties before and during the clamp were somewhat unstable.

Table 6.2 Optical property changes during arterial and venous clamping steps.
** *Indicates change was not well defined and could not be estimated.*
-- *Indicates measurement was not made.*

Sample	1040 or 1060 nm							
	Optical property prior to change (mm^{-1})		Arterial Occlusion (relative change)		Venous Occlusion (1) (relative change)		Venous Occlusion (2) (relative change)	
	$\sim\mu_a$	$\sim\mu_s'$	$\Delta\mu_a$	$\Delta\mu_s'$	$\Delta\mu_a$	$\Delta\mu_s'$	$\Delta\mu_a$	$\Delta\mu_s'$
1	0.049	0.55	-0.07	-0.02	0.09	-0.05	--	--
2	0.050	0.48	-0.15	0.03	0.24	-0.06	--	--
3	0.043	0.50	-0.20	-0.04	0.15	0.04	--	--
4	0.029	0.64	-0.17	**	0.33	**	--	--
5	0.024	0.66	--	--	0.59	0.06	0.57	0.05
6	0.036	0.48	--	--	0.11	-0.01	0.08	-0.02
7	0.043	0.53	--	--	0.08	0.06	0.09	0.07
8	0.050	0.48	--	--	0.25	-0.05	0.26	-0.07

Sample	1250 nm							
	Optical Property prior to change (mm^{-1})		Arterial Occlusion (relative change)		Venous Occlusion (1) (relative change)		Venous Occlusion (2) (relative change)	
	$\sim\mu_a$	$\sim\mu_s'$	$\Delta\mu_a$	$\Delta\mu_s'$	$\Delta\mu_a$	$\Delta\mu_s'$	$\Delta\mu_a$	$\Delta\mu_s'$
1	0.126	0.38	0.02	-0.01	0.025	-0.04	--	--
2	0.124	0.38	-0.02	0.01	0.050	-0.06	--	--
3	0.100	0.43	-0.03	0.01	0.040	-0.04	--	--
4	0.084	0.58	-0.01	**	0.035	**	--	--
5	0.084	0.60	--	--	0.040	-0.01	0.036	-0.003
6	0.093	0.45	--	--	0.027	**	0.022	**
7	0.117	0.43	--	--	0.030	-0.01	0.020	-0.030
8	0.120	0.38	--	--	0.094	-0.08	0.024	0.031

The magnitude of the pre-occlusion absorption coefficients measured on the palm of the hand, shown in Table 6.2, were higher than those found on the abdomen measurements, shown in Figure 6.2, by a factor of about 4. The skin on the palm of the hand is somewhat different from other body sites - in particular, the epidermis is 5-6 times thicker. This difference in tissue structure may affect the outcome of fitting algorithms which estimate the optical properties assuming a single layer, homogeneous structure. The implications of applying the model to heterogeneous tissues will be discussed in greater detail at the end of this chapter. The blood and water content of the skin on the hands may also be greater than that on the abdomen, which would result in a higher absorption coefficient.

During arterial occlusion, on average the absorption coefficient at 1040 nm decreased by about 15%, but changed by an average of only 2% at 1250 nm (in one case an increase was observed). This demonstrates that μ_a is less sensitive to blood oxygenation changes in the isosbestic wavelength region, as expected. The corresponding changes in the reduced scattering coefficient were on average 2% at 1040 nm and less than 1% at 1250 nm. The physiological explanation for the absorption decrease during arterial occlusion is well understood, while the change in scattering probably requires a more complicated explanation. A change in the scattering coefficient may be a result of a redistribution of tissue fluids in response to the lack of circulation in the tissue.

Although accurate determination of haemoglobin saturation changes requires more rigorous spectral analysis, a rough calculation can be performed to determine if the magnitude of the absorption changes observed in these experiments are reasonable. If water, Hb, and HbO_2 are assumed to be the only important chromophores in skin at 1040 nm, the absorption coefficient is given by:

$$\mu_a = \epsilon_{HbO2,1040nm}[HbO2] + \epsilon_{Hb,1040nm}[Hb] + \mu_{a,H2O,1040nm} \tag{21}$$

where ϵ is the specific extinction coefficient for the chromophore. The oxygen saturation, S, is defined as:

$$S = \frac{[HbO2]}{[Hb_t]}, \quad [Hb_t] = [HbO2] + [Hb] \tag{22}$$

The expected change in the absorption coefficient for a total oxygen desaturation is given by:

$$\Delta\mu_a = S(\epsilon_{HbO2} - \epsilon_{Hb})[Hb_t] \tag{23}$$

Assuming an initial oxygen saturation of 70% (typical for tissue) and a total Hb concentration of 100 μM, the expected change in absorption would be 0.0042 mm^{-1} from an initial μ_a of 0.031 mm^{-1}, corresponding to a change of 14%. This falls in the range of the observed absorption changes.

During the venous occlusion steps, average increases in μ_a of about 20%, 25%, and 4% were observed at 1040 nm,1060 nm, and 1250 nm respectively. This confirms that μ_a is less sensitive to changes in blood volume at wavelengths where it contributes less to the total absorption coefficient. Blood volume changes could also result in an increase in the tissue water concentration, which may explain the increases in μ_a at 1250 nm. The corresponding average changes in magnitude of μ_s' during venous occlusion were about 5%, 5%, and 2% at 1040 nm, 1060 nm, and 1250 nm respectively. In most cases μ_s' decreased or remained constant during occlusion. When the sign of the change is included in the average, the corresponding average changes in μ_s' during venous occlusion were about -2%, +1%, and -3% at 1040 nm, 1060 nm, and 1250 nm respectively. As discussed in the previous paragraph, a physiological explanation for the changes in μ_s' during occlusion is not known. The apparent change in μ_s' may be an artifact resulting from applying a model of a homogeneous, semi-infinite medium to a multi-layered structure, and will be discussed in section 6.4.

6.3 Temperature Dependence of Human Skin Optical Properties

The sensitivity of the optical properties of skin to changes in temperature is a major concern for monitoring applications. For example, Qu and Wilson [1997] used Monte Carlo simulations to predict that a 0.1 °C decrease in skin temperature would result in observed reflectance or transmittance change comparable to that induced by a 1 mM increase in glucose concentration, due to the change in the absorption coefficient of water with temperature. The absorption coefficient of water, one of the primary components of tissue, is known to be temperature dependent with a coefficient of about 0.5%/°C [Collins 1925]. The effect of temperature on optical properties of human skin *ex vivo* have been studied by Laufer *et al* [1998]. They performed measurements on thin samples of dermis and subdermis (primarily fat) in the 25-40 °C temperature range and found coefficients for relative changes in μ_s' of 0.47±0.05%/°C and -0.14±0.028%/°C for dermis and subdermis respectively They did not detect any changes in μ_a as a result of the temperature changes. It is also important to study the effect that skin temperature changes have *in vivo* Perfusion is known to depend strongly on local skin temperature [Kraning 1991], which may have a significant effect on the absorption coefficient at wavelengths where haemoglobin absorbs strongly Unfortunately, *in vivo* techniques are limited to sampling multiple layers of skin, which may lead to false conclusions when different tissues exhibit different temperature responses, as found by Laufer *et al* [1998]

Experiments were performed on human volunteers to investigate the temperature dependence of optical properties. The measurement protocol was similar to the baseline stability measurements described above. In order to produce controlled changes in temperature, a 1 cm thick aluminum collar was placed on the skin and fit loosely around the probe. Water from a heating and refrigerating water bath was circulated through the collar The collar is depicted in Figure 6.9 The collar temperature was held constant for 45-60 minutes at 37° C, then 20° C, then 45° C, and finally 37° C. The reflectance was

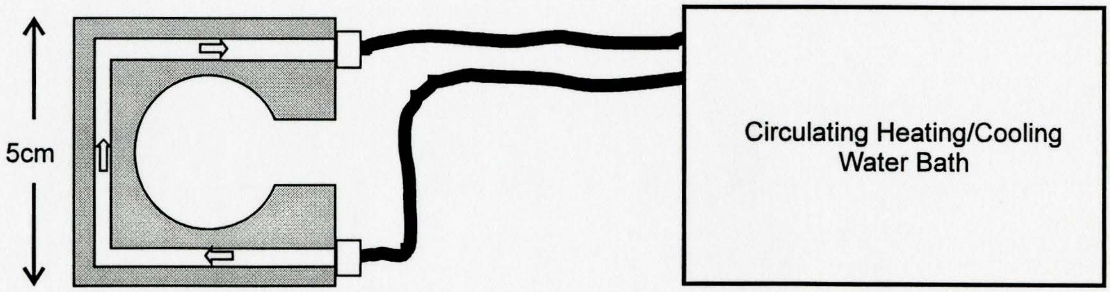

Figure 6.9 Probe collar used for skin temperature manipulation experiments.

sampled at 960 nm, 1060 nm, and 1250 nm. Measurements were performed on 7 Caucasian volunteers. Skin temperature was measured with a thermistor incorporated into the face of the probe.

The estimated optical properties based on reflectance measured during a typical temperature series are shown in Figure 6.10. The behaviour observed in the 7 measurements showed several qualitative trends. Both μ_s' and μ_a increased and decreased with increases and decreases in temperature, but with different relative magnitudes and temporal response. The relative changes in μ_s' were somewhat comparable at the three wavelengths studied, while the changes in μ_a generally had a strong wavelength dependence. The absorption coefficient at 1250 nm demonstrated the smallest response to changes in temperature.

The results of all of the temperature scans are summarized in Table 6.3, showing the estimated average relative changes for each temperature step. The changes are given in units of per cent per degree Celsius. This is not meant to imply that the optical properties change linearly with temperature, but is used as a convenient way to combine results for all the samples. It should be noted that the relative changes may be slightly underestimated because the time allowed for temperature stabilization may not have been sufficiently long. It was necessary to keep these plateau periods as short as possible to minimize the total length of the measurements. Although the temperature appeared to be stable during these periods, a time lag may be expected for some of the biological effects.

The relative transport scattering changes measured *in vivo* in this study are comparable to the coefficient for relative change measured by Laufer *et al* [1998] for the

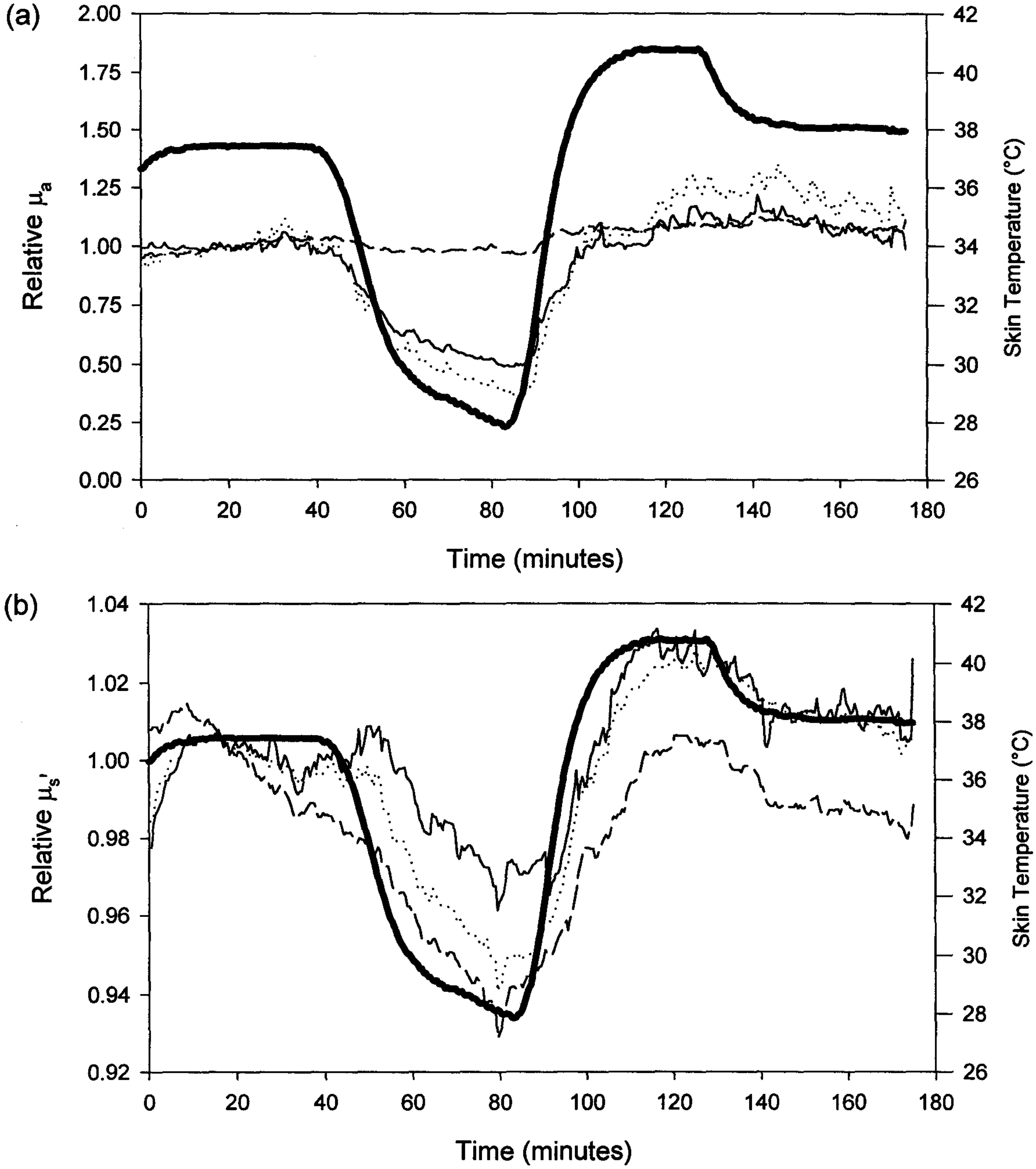

Figure 6.10 Optical properties measured during a typical temperature manipulation experiment. Skin temperature is plotted as a thick solid line. Reflectance was sampled at 3 wavelengths, plotted as: solid line - 960 nm, dotted line - 1060 nm, and dashed line - 1250 nm.

Table 6.3 Summary of optical property changes during skin temperature manipulations. In some experiments some elements of the scan were omitted to shorten the measurement or because of problems with equipment or data collection. In some cases the data were too noisy to estimate a change in optical property correlated to the temperature change. For these reasons the number of samples is less than the total (7) in some instances.

Wavelength (nm)		Temperature Decrease		Temperature Increase	
		$\Delta\mu_s'$ (%/°C)	$\Delta\mu_a$ (%/°C)	$\Delta\mu_s'$ (%/°C)	$\Delta\mu_a$ (%/°C)
960	# of samples	6	6	7	6
	min	0.00	-2.90	0.10	2.50
	max	-0.80	-6.70	0.80	22.50
	mean	-0.30	-4.40	0.40	13.20
1050	# of samples	6	6	7	6
	min	0.00	-2.50	0.20	2.50
	max	-0.80	-5.60	0.70	17.50
	mean	-0.30	-3.60	0.50	10.10
1250	# of samples	6	6	4	7
	min	0.00	0.00	0.00	1.00
	max	-0.80	-2.50	0.70	12.50
	mean	-0.20	-1.00	0.40	4.60

dermis. The responses to temperature increases seemed to be slightly higher than the response to temperature decreases. In all cases the relative change in absorption coefficient was much higher than the relative change in transport scattering coefficient. The response to increases in skin temperature was significantly higher than the response to decreases in skin temperature. The change in absorption coefficient can be attributed to changes in perfusion and hence tissue blood volume. Blood flow decreases when the skin is cooled, leading to a reduction of blood volume and a reduction of μ_a at wavelengths where haemoglobin absorbs. Even at wavelengths where μ_a is mostly due to water, a significant relative change in μ_a was observed. These changes are too large to be attributed solely to the change in water absorption itself, and may be a result of a change of water concentration in the region because of the changes in blood flow.

6.4 Discussion of *in Vivo* Results

The results of three different experiments in which the optical properties of skin and their response to externally induced physiological changes have been presented. In all of these experiments, the optical coefficients were estimated by applying a model of a homogeneous, semi-infinite medium to the tissue under study. As briefly mentioned previously, artifacts in the measured coefficients may result when applying this simple model to a multi-layered structure such as skin. Recognizing this, it is tempting to assume that applying this model will result in estimated optical properties which at least represent an average of properties of the different layers. When the relative changes in the optical properties are of most interest, one might expect that the measured relative changes will be reasonably correct even though the absolute coefficients are not.

In all of the presented results, there were features which could not be readily explained by the physiological changes in the experiment. The scattering coefficient spectra of human skin (Figure 6.1) showed consistent, unexpected features. Occlusion experiments showed that both the absorption and reduced scattering coefficients changed during arterial and venous occlusion, although only the changes in the absorption coefficient could be readily explained. Similarly, very large changes in the absorption coefficient were observed during skin temperature changes at wavelengths where the primary chromophore is water. It is possible that some or all of these features may in fact be a result of artifacts of applying an over-simplified model of tissue to estimate the optical properties.

Farrell *et al* [1998] studied this problem in detail using two-layer Monte Carlo simulations and the single-layer diffusion model for steady-state, spatially resolved diffuse reflectance. Their skin model consisted of a top dermal layer and a semi-infinite bottom layer of fat. They noted that reflectance data obtained using a two-layer Monte Carlo simulation could be fit very well to the semi-infinite, homogeneous model given by Equation 14, but that the regressions resulted in optical coefficients which did not match either layer. The estimated scattering coefficients were higher than the scattering coefficient of either layer, while the estimated absorption coefficients were lower than the absorption coefficient of either layer. This is consistent with what was observed in the *in vivo* spectral measurements described in Section 6.1 and shown in Figure 6.4, in which reasonable fits to *in vivo* reflectance data were obtained. They also noted that different fitting algorithms resulted in different results when applied to two-layer data.

In the Farrell study, the sensitivity and crosstalk of changes in optical properties in the top and bottom layers of skin to the estimated optical properties were studied for different dermal (top) layer thicknesses. A neural network was used to estimate the optical properties from Monte Carlo data. They found that crosstalk of absorption changes in the dermis into the measured scattering coefficient increased with increasing interface depth, up to a depth of 2.5 mm where the crosstalk approached 0.2 (ie., a 1% increase of top layer absorption resulted in an apparent 0.2 % increase in measured μ_s'). Changes in μ_s' in the upper layer were found to be inversely correlated with changes in fitted absorption coefficients at depths below 2 mm, with maximum crosstalk at smaller interface depths approaching a factor of 2.5. Sensitivities of the measured optical coefficients to actual changes in coefficients in the top layers were found to be less than unity.

The sensitivities and crosstalks observed by Farrell *et al* [1998] were determined using baseline optical properties of dermis and subdermis (fat) for the wavelength range of 700-900nm. The absolute sensitivities observed will depend on these coefficients, as well as the source-detector distances used and the fitting algorithm. However, it is interesting to compare the observations of the Farrell study to some of the features observed in Sections 6.1, 6.2 and 6.3. Consider the results from the temperature manipulation experiments summarized in Table 6.3. At 1250 nm, where blood volume effects should be minimal, changes in μ_a were still observed while scattering changes did not exhibit a wavelength dependence. A real change in μ_s' in the dermis could result in a significant apparent change in μ_a when the bulk tissue is analysed. In the occlusion experiments, summarized in Table 6.2, changes in μ_s' were often observed during the occlusion steps, although only the changes in μ_a could be explained physiologically. Real changes in μ_a due to blood volume or oxygenation changes in the dermis may result in apparent changes in μ_s' when the bulk tissue is analysed. The features observed in the μ_s' spectra (Figure 6. 1) may also be in part or in whole artifacts arising from the layered structure of the skin.

Chapter 7 Summary and Conclusions

This thesis describes a system which was developed for the *in vivo* measurement of optical properties of tissue in the 900-1400 nm wavelength region. The instrument employs the technique of steady-state spatially resolved diffuse reflectance. This is a relatively straightforward method which consists of measuring the intensity of light exiting tissue at several distances from an input source. *In vivo* applications of this method have been described by several authors, but never in this wavelength region which may have advantages for some types of measurement. The technique was modeled using a diffusion approximation to radiation transport, as well as Monte Carlo simulations. In both cases, a homogeneous semi-infinite medium was assumed. In these models, a perfectly matched refractive index was assumed at the interface between the sample and the measurement probe.

Three different methods of optical property extraction were investigated: (1) a nonlinear least-squares fit to a diffusion model, (2) a neural network fit to a diffusion model and (3) a nonlinear least-squares fit to a 'Mono Monte Carlo' simulation. The performance of these methods was compared by applying them to theoretical reflectance data generated from a Monte Carlo simulation. The fitting methods which used a diffusion approximation suffered from systematic errors in estimated coefficients, with the nonlinear least squares method demonstrating better performance than the neural network.

The Monte Carlo fitting technique was found to have the best performance, and did not suffer as much from systematic errors, particularly in the estimation of μ_s'. In general, all methods were able to estimate μ_s' with greater accuracy than μ_a.

A fibre-optic probe is used to obtain spatially resolved diffuse reflectance at 15 distances ranging from 1 to 10 mm from the light input. A broadband light source is used so that continuous spectral information can be gathered. At one wavelength, intensities at all distances are measured simultaneously by imaging all detection fibres onto a photodiode array. The grating in the monochromator can be rotated to allow reflectance measurements at different wavelengths. To reduce the dynamic range of the intensities, the light detected at some of the smaller source-detector separations is attenuated. The relative response of the different detectors is determined using a calibration measurement.

A series of tests were performed on the instrument to verify the operation of some of the individual elements, as well as the system as a whole. Detector drift was found to be a problem which could be corrected by leaving the detector cooled for a long period of time prior to performing measurements. The calibration method, which uses an integrating sphere to produce uniform illumination of the detector fibres of the probe, was found to be suitable for determining the relative response of the different detectors. Corrections for crosstalk between fibres imaged adjacently on the photodiode array were found to be necessary, and a first-order correction procedure was implemented for this purpose. Measurements on phantoms over long acquisition periods demonstrated that the device was very stable and suitable for *in vivo* monitoring.

A series of measurements was performed on aqueous suspensions of monodisperse polystyrene spheres to evaluate the ability of the technique to measure absolute optical properties. The three methods of optical property extraction were compared in this task.

The discrepancies between the predicted and estimated coefficients were larger than expected for all three methods, and could not be attributed to the expected systematic discrepancies presented in Chapter 3. Systematic discrepancies were found when the measured and predicted reflectance data were compared, which indicated that the errors in the extracted coefficients were a result of a systematic measurement problem or modelling problem. Two possible sources of these errors were described: (1) assuming a perfectly matched refractive index between the sample surface and measurement probe and (2) not accounting for the limited collection solid angle determined by the numerical aperture of the detector fibres. Application of these factors to the model would result in better agreement between the measured and predicted reflectance in many cases. However, further investigations are required to fully explain the discrepancy.

Characterization of the numerical aperture and refractive index parameters may be difficult to do. A slightly different application of the neural network analysis method may provide a solution to the problem of absolute determination of optical properties. Measurements of optical properties on suspensions of polystyrene spheres in water would provide a large set of reflectance data for a large range of combinations of absorption and scattering. Data obtained in this way could be used as a training set for a neural network, which could then be applied to reflectance measurements made *in vivo* with the same probe geometry.

Several experiments were performed using the instrument to demonstrate its capabilities and the advantages of working in this wavelength range. Optical property spectra were obtained on the skin of several volunteers. These spectra showed a large inter-volunteer variation of optical properties. The absorption spectra showed reasonable qualitative agreement with the absorption spectrum of water which is the primary chromophore in tissue in this wavelength range. The spectra of the estimated reduced scattering coefficient contained unexpected features. Although the magnitude of the estimated μ_s' varied between samples, the features in the spectra were fairly consistent. It is believed that these features are an artifact of applying a model of a semi-infinite homogeneous medium to a layered tissue.

Measurements were performed in which blood oxygenation and blood volume were manipulated to investigate the wavelength dependence. Reflectance was sampled on the palm of the hand while arterial or venous occlusion was induced via pressure applied to a cuff worn on the upper arm. As expected, the absorption coefficient measured at a wavelength where HbO_2 and Hb are isosbestic(1250 nm) showed a much lower sensitivity to the blood oxygenation changes than at 1040 nm. The absorption coefficient at 1250 nm was also less sensitive to blood volume changes, due to the negligible contribution of Hb absorption to the tissue absorption coefficient. Changes that were observed at 1250 nm could be due to changes in water distribution. Changes in the reduced scattering coefficient were observed during the occlusion steps, which may also be due to water distribution effects. It is also probable that some of the apparent changes in optical properties are artifacts of applying the simple, homogeneous model of tissue to reflectance data sampled from a layered tissue. Temperature manipulation experiments on human skin showed similar trends, and it is likely that these results are also infected with artifacts associated with the two-layer structure of skin.

For future *in vivo* measurements, this measurement technique would benefit from improvements in two main areas. First, there is a need to improve the ability of the method in the estimation of absolute optical properties. While some suggestions have been presented as to the source of the errors, further studies are warranted to determine how best to improve the analysis models and fitting methods. Further accuracy could also be attained by modifying the instrument to measure absolute, rather than relative reflectance. This is, in practice, much more difficult to do. A second improvement, particularly for skin measurements, is to apply a two-layer model of skin for the extraction of optical properties. Several groups have addressed this problem using diffusion approximations [Keijzer *et al* 1988, Schmitt *et al* 1990] and Monte Carlo techniques [Wang *et al* 1995]. The inverse problem of fitting models to experimental data to estimate optical properties is much more complicated since there are at least five parameters (top layer thickness, μ_s' of top and bottom layers and μ_a of top and bottom layers). Kienle *et al* [1998] have had some success with estimating optical properties in a two-layer system using absolute spatially resolved diffuse reflectance.

Until such improvements can be made, optical property measurements made using this technique should be used with caution, recognizing the somewhat qualitative nature of the estimated coefficients. The instrument itself was found to accurate and reliable for reflectance measurements, and thus provides a useful vehicle for investigations into issues such as layered structures. A reduced sensitivity to blood volume and oxygenation effects in the longer wavelength was clearly demonstrated, showing the potential advantage of using this wavelength range for *in vivo* monitoring of analytes such as glucose.

BIBLIOGRAPHY

Abramowitz, M. and Stegun, I., ed., 1972 Handbook of Mathematical Functions, Dover Publications, Inc., New York.

Anderson, R. R., 1993 "Optics of the Skin" in Clinical Photomedicine, H. W. Lim and N. A. Soter ed., Marcel Dekker, Inc., New York.

Andersen, P. H., 1994 "In vivo cutaneous assays to evaluate topical corticosteroids and nonsteroidal anti-inflammatory drugs using reflectance spectroscopy" in Bioengineering of the Skin: Cutaneous Blood Flow and Erythema, E. Berardesca, P. Elsner, and H. I. Maibach ed., CRC Press, Boca Raton.

Barlow, R. B. and Polanyi, M. L., 1962 "Absorption Measurements for Oxygenated and Reduced Hemoglobin in the range 0.6-1.88 microns" , Clin. Chem. 8 pp. 67-71.

Bays, R., Wagnieres, G., Robert, D., Braichotte, D., Savary, J., Monnier, P. and van den Bergh, H., 1996 "Clinical determination of tissue optical properties by endoscopic spatially resolved reflectometry" Appl .Opt., 35 pp. 1756-1766.

Bevington, P. R., 1969 Data Reduction and Error Analysis for Scientists and Engineers, McGraw Hill, New York.

Bruulsema, J. T., Hayward, J. E., Farrell, T. J., Patterson, M. S., Heinemann, L., Berger, M., Koschinsky, T., Sandahl-Christiansen, J., Orskov, H., Essenpreis, M., Schmelzeisen-Redeker, G. and Bocker, D., 1997 "Correlation between blood glucose concentration in diabetics and noninvasively measured tissue optical scattering coefficient" Opt. Let. 22 pp. 190-192.

Chan, E., Sorg, B. Protsenko, D., O'Neil, M., Motamedi, M. and Welch, A. J., 1997 "Effects of compression on human skin optical properties" Proc. SPIE 2979, p. 314-324.

Chan, K. P., Yamada, M., Devaraj, B. and Inaba, H., 1995 "Optical imaging through highly scattering media by use of heterodyne detection in the 1.3-μm wavelength region," Opt. Let. 20 pp. 492-494.

Cheong, W., Prahl, S. A. and Welch, A. J., 1990 "A review of the optical properties of biological tissues" IEEE J. Qantum Electron. 26 pp. 2166-2185.

Collins, J., 1925 "Change in the infrared absorption spectrum of water with temperature" Phys. Rev. 26 pp. 771-779.

Cope, M. and Delpy, D., 1988 "System for long-term measurement of cerebral blood and tissue oxygenation on newborn infants by near infra-red transillumination" Med. and Biol. Eng. and Comput. 26 pp. 289-294.

Duck, F. 1990 Physical Properties of Tissue, Academic Press, London.

Duderstadt, J. and Hamilton, L., 1976, Nuclear Reactor Analysis, John Wiley & Sons, Inc., New York.

Duke Scientific Corporation, 1996, Index of Refraction Notes, Technical Note TN-007 02.

Farrell, T. J., Patterson, M. S. and Essenpreis, M., 1998 "Influence of layered tissue architecture on estimates of tissue optical properties obtained from spatially resolved diffuse reflectometry" Accepted for publication in Appl. Opt. 37.

Farrell, T. J., Patterson, M. S., Essenpreis, M. and Bocker, D. 1996 "A comparison of the sensitivity of continuous wave and frequency domain systems to changes in the absorption and scattering coefficients of tissue"

Farrell, T. J., Patterson M. S., Hayward, J. E., Wilson, B. C. and Beck, E. R., 1994 "A CCD and neural network based instrument for the non-invasive determination of tissue optical properties *in vivo*" Proc. SPIE 2135 pp. 117-128.

Farrell, T. J., Wilson, B. C. and Patterson, M. S., 1992 "The use of a neural network to determine tissue optical properties from spatially resolved diffuse reflectance measurements" Phys. Med. Biol., 37 pp. 2281-2286.

Farrell, T. J. and Patterson, M. S., 1992 "A diffusion theory model of spatially resolved, steady-state diffuse reflectance for the noninvasive determination of tissue optical properties in vivo" Med. Phys. 19 pp. 879-888.

Flock, S. T., Patterson, M. S., Wilson, B. C. and Wyman, D. R., 1989 "Monte Carlo modelling of light propagation in highly scattering tissues-I: Model predictions and comparison with diffusion theory", IEEE Trans. Biomed. Eng. 36 pp. 1162-1168.

Flock, S. T., Wilson, B. C. and Patterson, M. S., 1989 "Monte Carlo modelling of light propagation in highly scattering tissues-II: Comparison with measurements in phantoms", IEEE Trans. Biomed. Eng. 36 pp. 1169-1173.

Graaff, R., Dassel, A. C. M., Koelink, M. H., de Mul, F.F.M., Aarnoudse, J. G. and Zijlstra, W. G., 1993 "Optical properties of human dermis in vitro and in vivo", Appl. Opt. 32 pp. 435-447.

Groenhuis, R. A. J., Ferwerda, H. A. and Ten Bosch, J. J., 1983 "Scattering and absorption of turbid materials determined from reflection measurements. 1: Theory", Appl. Opt. 22 pp. 2456-2462.

Hale, G. M. and Querry, M. Q., 1973 "Optical constants of water in the 200-nm to 200 um wavelength region" Appl. Opt. 12 pp. 555-563.

Haskell, R. C., Svaasand, L. O., Tsay, T., Feng, T., McAdams, M. S. and Tromberg, B. J., 1994 "Boundary conditions for the diffusion equation in radiative transfer", J. Opt. Soc. Amer. (A) 11 pp. 2727-2741.

Henyey, L. G. and Greenstein, J. L., 1941 "Diffuse radiation in the galaxy", Astrophys. J. 93 pp. 70-83.

Huang, D., Swanson, E. A., Lin, C. P., Schuman, J. S., Stinson, W. G., Chang, W., Hee, M. R., Flotte, T., Gregory, K., Puliafito, C. A. and Fujimoto, J. G., 1991 "Optical coherence tomography", Science 254 pp. 1178-1181.

Jacques, S. L., Gutsche, A., Schwartz, J., Wang, L. and Tittel, F., 1993 "Video reflectometry to specify optical properties of tissue *in vivo*" in Medical Optical Tomography: Functional Imaging and Monitoring, G. Mueller, B. Chance, R. R. Alfano, S. R. Arridge, J. Beuthan, E. Gratton, M. Kaschke, B. R. Masters, S. Svanberg, and P. Van der Zee eds. Vol. ISII of SPIE Institute Series (Society of Photo-Optical Instrumentation Engineers, Bellingham, Wash.,), pp. 211-226.

Jacques, S. L. and Wang, L., 1995 "Monte Carlo modelling of light transport in tissues" in Optical -Thermal Response of Laser-Irradiated Tissue, A. J. Welch and M. J. C. van Gemert, eds., Plenum Press, New York.

Keijzer, M., Star, W. M. and Storchi, P. R. M., 1988 "Optical diffusion in layered media," Appl. Opt. 27 pp. 1820-1824.

Kienle, A., Patterson, M. S., Utke, N., Bays, R., Wagnieres, G. and van den Bergh, H., 1998 "Determination of the optical properties of two-layered turbid media" Accepted for publication in Appl. Opt. 37.

Kienle, A. and Patterson, M. S., 1997 "Improved solutions of the steady-state and the time-resolved diffusion equations for reflectance from a semi-infinite turbid medium", J. Opt. Soc. Amer. (A) 14 pp. 246-254.

Kienle, A. and Patterson, M. S., 1996 "Determination of the optical properties of turbid media from a single Monte Carlo simulation", Phys. Med. Biol. 41 pp. 2221-2227.

Kienle, A., Lilge, L., Patterson, M. S., Hibst, R., Steiner, R. and Wilson, B. C., 1996 "Spatially resolved absolute diffuse reflectance measurements for noninvasive determination of the optical scattering and absorption coefficients of biological tissue" Appl. Opt. 35 pp. 2304-2314.

Kraning, K., 1991 "Temperature Regulation and the Skin" in Physiology, Biochemistry, and Molecular Biology of the Skin, L. A. Goldsmith ed., Oxford University Press, New York.

Laufer, J., Simpson, R., Kohl, M., Essenpreis, M., and Cope, M., 1998 "Effect of temperature on the optical properties of *ex-vivo* human dermis and subdermis" Submitted to Phys. Med. Biol.

Lin, S., Wang, L., Jacques, S. L. and Tittel, F. K., 1997 "Measurement of tissue optical properties by the use of oblique-incidence optical fiber reflectometry", Appl. Opt. 36 pp. 136-143.

Liu, H., Boas, D. A., Zhang, Y., Yodh, A. G. and Chance, B., 1995 "Determination of optical properties and blood oxygenation in tissue using continuous NIR light" Phys. Med. Biol. 40 pp. 1983-1993.

Mourant, J. R., Fuselier, T., Boyer, J., Johnson, T. M. and Bigio, I. J., 1997 "Predictions and measurements of scattering and absorption over broad wavelength ranges in tissue phantoms," Appl. Opt. 36 pp. 949-957.

Nichols, M. G., Hull, E. L. and Foster, T. H., 1997 "Design and testing of a white-light steady-state diffuse reflectance spectrometer for determination of optical properties of highly scattering systems" Appl. Opt. 36 pp. 1-12.

Odland, G., 1991 "Structure of the skin" in Physiology, Biochemistry, and Molecular Biology of the Skin, L. A. Goldsmith ed., Oxford University Press, New York.

Panjehpour, M., Overholt, B. F., Frazier, D. L. and Klebanow, E. R., 1991 "Nd:YAG laser-induced hyperthermia treatment of spontaneously occurring veterinary head and neck tumors," Lasers Surg. Med. 11 pp. 351-355.

Patterson, M. S., 1995 "Noninvasive measurements of tissue optical properties: current status and future prospects" Comments Mol. Cell. Biophys. 8 pp. 387-417.

Qu, J. and Wilson, B., 1997 "Monte Carlo modeling studies of the effect of physiological factors and other analytes on the determination of glucose concentration *in vivo* by near infrared optical absorption and scattering measurements" J. Biomed. Opt. 2 pp. 319-325.

Rumelhart, D. E., McClelland, J. L. and the PDP Research Group, 1986 Parallel Distributed Processing, MIT Press, Cambridge.

Schmitt, J. M., Zhou, G. X., Walker, E. C. and Wall, R. T. 1990 "Multilayer model of photon diffusion in skin" J. Opt. Soc. Am. A 7 pp. 2141-2153.

Simpson, R., Laufer, J., Kohl, M., Essenpreis, M. and Cope, M., 1997 "Near infrared optical properties of ex-vivo human skin and sub-cutaneous tissues using reflectance and transmittance measurements" Proc. SPIE 2979 pp. 307-313.

van de Hulst, H., 1981, Light Scattering by Small Particles, Dover Publications, Inc., New York.

van Staveren, H. J., Moes, C. J. M., van Marle, J., Prahl, S. A. and Van Gemert, M. J. C., 1991 "Light scattering in Intralipid-10% in the wavelength range of 400-1100 nm" Appl. Opt. 30 pp. 4507-4514.

Wang, L., Jacques, S. L., Zheng, L., 1995 "MCML - Monte Carlo modelling of light transport in multi-layered tissues", Comput. Methods Programs Biomed. 47 pp. 131-146.

Weast, R. C., ed., 1989 CRC Handbook of Chemistry and Physics, 60th ed., CRC Press, Boca Raton.

Wilson, B. C., 1995 "Measurement of tissue optical properties: methods and theories" in Optical -Thermal Response of Laser-Irradiated Tissue, A. J. Welch and M. J. C. van Gemert, eds., Plenum Press, New York.

Wyman, D. R., Patterson, M. S. and Wilson, B. C., 1989 "Similarity relations for the interaction parameters in radiation transport," Appl. Opt. 28 pp. 5243-5249.